

**Umweltforschungsplan
des Bundesministeriums für Umwelt, Naturschutz und
Reaktorsicherheit**

Anlagenbezogener Immissionsschutz

Förderkennzeichen (UFOPLAN) 203 43 256

**Enhancement of a diagnostic wind field model for
licensing industrial facilities (TA Luft)**

**Weiterentwicklung eines diagnostischen
Windfeldmodells für den anlagenbezogenen
Immissionsschutz (TA Luft)**

von

Dr. Ulf Janicke

Dr. Lutz Janicke

Ingenieurbüro Janicke, Dunum

Im Auftrag des Umweltbundesamtes Berlin

Oktober 2004

Report Cover Sheet

1. Report No. UBA-FB	2.	3.
4. Report Title Enhancement of a diagnostic wind field model for licensing industrial facilities (TA Luft)		
5. Author(s), Family Name(s), First Name(s) Janicke, Ulf Janicke, Lutz		8. Report Date October 2004
6. Performing Organisation (Name, Address) Janicke Consulting D-26427 Dunum Alter Postweg 21		9. Publication Date November 2004
7. Funding Agency (Name, Address) Umweltbundesamt (Federal Environmental Agency) Postfach 33 00 22 D-14191 Berlin		10. UFOPLAN-Ref. No. 203 43 256
		11. No. of Pages 98
		12. No. of References 13
		13. No. of Tables, Diagrams 7
		14. No. of Figures 63
15. Supplementary Notes The wind field program TALdia is provided in the Internet at www.austal2000.de .		
16. Abstract For source heights between 1.2 and 1.7 of neighbouring building heights the regulation TA Luft envisions the use of a diagnostic wind field model which, however, so far has not been part of the program system AUSTAL2000. In this project, a diagnostic microscale wind field model (DMK) was developed for the use with AUSTAL2000 and integrated into the existing wind field model TALdienes. In view of a robust use in practice, particular attention was paid to the condition that the model results should be largely independent of the way in which the buildings are defined and oriented with respect to the calculation grid. In addition, a simple approach was developed to take into account the additional turbulence caused by the buildings in a dispersion calculation. The model fields and the concentration fields obtained in combination with AUSTAL2000 were validated by means of a variety of experimental data sets.		
17. Keywords TA Luft, air quality control, diagnostic wind field model		
18. Price	19.	20.

Berichts-Kennblatt

1. Berichtsnummer UBA-FB	2.	3.
4. Titel des Berichts Weiterentwicklung eines diagnostischen Windfeldmodells für den anlagenbezogenen Immissionsschutz (TA Luft)		
5. Autoren, Namen, Vornamen Janicke, Ulf Janicke, Lutz	8. Abschlußdatum Oktober 2004	
6. Durchführende Institution (Name, Anschrift) Ing.-Büro Janicke D-26427 Dunum Alter Postweg 21	9. Veröffentlichungsdatum November 2004	
7. Fördernde Institution (Name, Anschrift) Umweltbundesamt Postfach 33 00 22 14191 Berlin	10. UFOPLAN-Nr. 203 43 256	
	11. Seitenzahl 98	
	12. Literaturangaben 13	
	13. Tabellen und Diagramme 7	
	14. Abbildungen 63	
15. Zusätzliche Angaben Das Windfeldprogramm TALdia wird im Internet auf www.austal2000.de bereitgestellt.		
16. Zusammenfassung Für Quellhöhen zwischen dem 1.2-fachen und 1.7-fachen benachbarter Gebäudehöhen sieht die TA Luft den Einsatz eines diagnostischen Windfeldmodells vor, das bisher aber nicht Bestandteil des Programmsystems AUSTAL2000 war. In diesem Projekt wurde ein diagnostisches mikroskaliges Windfeldmodell (DMK) für den Einsatz mit AUSTAL2000 entwickelt und in das bestehende mesoskalige Modell TALdiames eingebaut. Für einen robusten Einsatz in der Praxis wurde ein besonderes Augenmerk auf die Randbedingung gelegt, daß die Modellergebnisse weitgehend unabhängig von der Art der Gebäudefestlegung und ihrer Orientierung relativ zum Rechengitter sein sollten. Zusätzlich wurde ein einfacher Ansatz entwickelt, mit dem die gebäudeinduzierte Zusatztrübung in der Ausbreitungsrechnung berücksichtigt werden kann. Die Modellfelder und die in Kombination mit AUSTAL2000 erzielten Konzentrationsverteilungen wurden anhand zahlreicher experimenteller Datensätze validiert.		
17. Schlagwörter TA Luft, Immissionsschutz, Diagnostisches Windfeldmodell		
18. Preis	19.	20.

Contents

1	Introduction	5
2	Concept	6
3	Model	7
3.1	Near wake	7
3.2	Prandtl layer and frontal vortex	9
3.3	Enhanced turbulence produced by the building	11
4	Verification and Validation	12
4.1	Verification	14
4.1.1	Partition of a building complex into simpler elements	14
4.1.2	Rastering of a building with rectangular base	16
4.1.3	Rastering of a building with circular base	20
4.1.4	Orientation of the calculation grid, influence on the wind field . . .	22
4.1.5	Orientation of the calculation grid, influence on the concentration distribution	25
4.2	Validation of the wind fields	26
4.2.1	Data sets of the guideline draft VDI 3783 part 9	26
4.2.2	U-shaped building	34
4.2.3	Street crossing	39
4.2.4	Measurements at the streets <i>Bonnerstrasse</i> and <i>Venloerstrasse</i> . . .	43
4.3	Validation of the velocity fluctuations	45
4.3.1	CEDVAL data sets A1-1, A1-4, A1-6	45
4.3.2	Cooling tower	52
4.4	Validation of the concentration distributions	54
4.4.1	U-shaped building	54
4.4.2	Cooling tower	65
4.4.3	CEDVAL data set D1-4 (Uttenweiler)	67
4.4.4	Comparison with the prognostic wind field model MISKAM	71
5	Transition to elevated sources	74
6	Summary	81
7	References	82
	Appendix	84
A	Mathematical calculation of the diagnostic wind field	84
B	Parameter variations	89

List of Figures

1	Calculation of the diagnostic wind field.	10
2	Test: Partition of a building complex into simpler elements (horizontal cut).	14
3	Test: Partition of a building complex into simpler elements (vertical cut).	15
4	Test: Rastering of a building with rectangular base (flow direction 225 deg, horizontal cut).	17
5	Test: Rastering of a building with rectangular base (flow direction 270 deg, horizontal cut).	18
6	Test: Rastering of a building with rectangular base (flow direction 290 deg, horizontal cut).	19
7	Test: Rastering of a building with circular base (horizontal cut).	20
8	Test: Rastering of a building with circular base (vertical cut).	21
9	Test: Orientation of the calculation grid. Example wind fields for two orientations.	23
10	Test: Orientation of the calculation grid. Velocity component in direction of the incoming flow in the central lee for different distances and orientations.	24
11	Test: Orientation of the calculation grid. Near ground concentration averaged over an isotropic wind rose for two orientations of source and building with respect to the calculation grid.	25
12	Guideline draft VDI 3783 part 9, data set c1, quasi 2-dimensional building in a cross flow.	29
13	Guideline draft VDI 3783 part 9, data set c3, cube in a cross flow.	30
14	Guideline draft VDI 3783 part 9, data set c4, cube in a diagonal flow.	31
15	Guideline draft VDI 3783 part 9, data set c5, cuboid in a cross flow.	32
16	Guideline draft VDI 3783 part 9, data set c6, set of 3 times 7 cuboids in a cross flow.	33
17	U-shaped building ($H = 28$ m), horizontal cuts.	35
18	U-shaped building ($H = 28$ m), vertical cuts.	36
19	U-shaped building ($H = 40$ m), Horizontal cuts.	37
20	U-shaped building ($H = 40$ m), vertical cuts.	38
21	Street crossing (incoming flow direction $r = 270$ deg, horizontal cut at $z = 4.5$ m, $\tau = 1$ s).	40
22	Street crossing (incoming flow direction $r = 270$ deg, horizontal cut at $z = 15$ m, $\tau = 1$ s).	40
23	Street crossing (incoming flow direction $r = 225$ deg, horizontal cut at $z = 4.5$ m, $\tau = 1$ s).	41
24	Street crossing (incoming flow direction $r = 225$ deg, horizontal cut at $z = 15$ m, $\tau = 1$ s).	41
25	Street crossing (incoming flow direction $r = 240$ deg, horizontal cut at $z = 4.5$ m, $\tau = 1$ s).	42
26	Street crossing (incoming flow direction $r = 240$ deg, horizontal cut at $z = 15$ m, $\tau = 1$ s).	42
27	Measurements in the streets <i>Bonnerstrasse</i> (top) and <i>Venloerstrasse</i>	44

28	Data set A1-1, difference of velocity fluctuations with respect to the undisturbed flow.	46
29	Data set A1-1, difference of velocity fluctuations with respect to the undisturbed flow.	47
30	Data set A1-4, difference of velocity fluctuations with respect to the undisturbed flow.	48
31	Data set A1-4, difference of velocity fluctuations with respect to the undisturbed flow.	49
32	Data set A1-6, difference of velocity fluctuations with respect to the undisturbed flow.	50
33	Data set A1-6, difference of velocity fluctuations with respect to the undisturbed flow.	51
34	Wind tunnel measurements for a cooling tower. Calculated increase of velocity fluctuations due to the cooling tower.	53
35	Concentration distribution near ground for an U-shaped building ($H = 28$ m) and different directions of the incoming flow.	56
36	Concentration distribution near ground for an U-shaped building ($H = 28$ m) and different directions of the incoming flow.	57
37	Concentration distribution near ground for an U-shaped building ($H = 28$ m) and different directions of the incoming flow.	58
38	Concentration distribution near ground for an U-shaped building ($H = 16$ m, $H = 40$ m) and different directions of the incoming flow.	59
39	Concentration distribution near ground for an U-shaped building ($H = 16$ m, $H = 40$ m) and different directions of the incoming flow.	60
40	Concentration distribution near ground for an U-shaped building ($H = 16$ m, $H = 40$ m) and different directions of the incoming flow.	61
41	Test runs without additional turbulence: Concentration distribution near ground for an U-shaped building ($H = 28$ m) and different directions of the incoming flow.	62
42	Test runs without additional turbulence: Concentration distribution near ground for an U-shaped building ($H = 28$ m) and different directions of the incoming flow.	63
43	Test runs without additional turbulence: Concentration distribution near ground for an U-shaped building ($H = 28$ m) and different directions of the incoming flow.	64
44	Cooling tower in Emsland, calculated concentration distribution near ground for an incoming flow direction of 120 deg.	66
45	Cooling tower in Emsland, calculated concentration distribution near ground for an incoming flow direction of 295 deg.	66
46	Location of buildings and sources applied in the dispersion calculations for the CEDVAL data set D1-4.	67
47	Maximum concentrations measured in the wind tunnel (diamonds) and calculated by the model (bars) for three distances from source SII.	69

48	Like Fig. 47, but with application of the default boundary layer model of LASAT instead of the one of guideline VDI 3783 part 8.	70
49	Concentration distribution near ground for the zero case without buildings and a constant wind direction. Left: Application of the profiles according to guideline VDI 3783 part 8. Right: Application of the MISKAM profiles. . .	72
50	Rastered building shapes used for the comparison with MISKAM.	72
51	Concentration distribution near ground for an isotropic wind rose, centre source. Left: Application of the fields of the present model. Right: Application of the MISKAM fields.	73
52	Concentration distribution near ground for an isotropic wind rose, southwest source. Left: Application of the fields of the present model. Right: Application of the MISKAM fields.	73
53	Transition to elevated sources. Isotropic wind rose, densely build-up area, source height 35 m (1.7 times the building heights).	76
54	Transition to elevated sources. Isotropic wind rose, source height 34 m (1.7 times the building height).	77
55	Transition to elevated sources. Isotropic wind rose, source height 40 m (2 times the building height).	78
56	Transition to elevated sources. Isotropic wind rose, source height 50 m (2.5 times the building height).	79
57	Transition to elevated sources. Meteorological statistics anonym. aks, source height 34 m (1.7 times the building height).	80
58	Parameter variations, parameters a_1 and a_3	91
59	Parameter variations, parameter a_2	92
60	Parameter variations, parameter a_5	93
61	Parameter variations, parameter h_s	94
62	Parameter variations, parameter f_s	95
63	Parameter variations, parameter f_k	96

1 Introduction

The program system AUSTAL2000¹ contains a diagnostic wind field model that is designed for applications in orographically structured terrain in the absence of buildings. The demands of practice call for an extension to built-up terrain. Such a wind field model, in the following referred to as DMK (*Diagnostisches Mikroskaliges Windfeldmodell* / diagnostic wind field model for the microscale), must obey several constraints:

- It must be applicable in the framework of AUSTAL2000, i.e. as a standard tool. This implies for example that wind field libraries must be generated with feasible time effort.
- It must fit the requirements of the *TA Luft* and the modelling concept of AUSTAL2000. For example, the vertical wind profile in the undisturbed case must be in accordance with guideline VDI 3783 part 3; likewise, for source heights exceeding 1.7 building heights there should be little difference in the resulting concentration distribution if an increased surface roughness length is applied instead of the wind field model, as envisioned in the *TA Luft*.
- The wind field should be largely independent of the way used to specify the building shapes (for example exact or rastered shapes) and of the orientation of the calculation grid with respect to the buildings.
- The wind and turbulence fields created by the model as well as the concentration fields calculated in combination with AUSTAL2000 should show reasonable agreement with experimental data.

So far, preferentially diagnostic wind field models have been applied in practice, in particular because of the first constraint stated above. Preliminary to the development of AUSTAL2000, the adoption of the model DMW, a diagnostic wind field according to guideline VDI 3783 part 10, was discussed, but it was discarded due to problems with the third constraint.

In this project, the wind field model of AUSTAL2000, *TALdiames*, was extended to built-up areas. Beside the modified boundary constraints, the wake field and the modified turbulence properties of the air flow had to be accounted for.

One has to bear in mind that according to the *TA Luft*, appendix 3, section 10, a diagnostic wind field model is applicable only to those situations, where the emission sources have a height of at least 1.2 times the height of the surrounding buildings. Hence in a dispersion calculation, the wake of the buildings takes effect only in course of the plume expansion and is less important for the dispersion as compared to lower sources. For the envisioned situations, alas almost no experimental validation sets were available and one had to use data sets for lower sources and results from other models instead.

¹An exemplary realization of the calculation specifications given in the *TA Luft* (Technical Instruction on Air Quality Control), see Internet page www.austal2000.de.

The wake field was therefore studied carefully and tested also for low sources. This is useful as well in view of the fact that the application range of the *TA Luft* includes diffusive emissions which do not meet the required emission heights. Last but not least, a reasonable modelling for low sources enhances confidence in a suitable treatment of elevated sources.

The extension of *TALdiames* was realized in the following steps:

1. Development of a model concept to include building influences for flat terrain based on the diagnostic wind field model implemented in the dispersion system LASAT. For a better overview, the wind field model was implemented in the programming language JAVA.
2. Calibrations and test calculations.
3. Application of the model fields in dispersion calculations with AUSTAL2000 (LASAT in AUSTAL2000 mode) and comparison with measured concentrations.
4. Translation to the programming language C and implementation into *TALdiames*.

The first three steps are described in the following.

2 Concept

A diagnostic wind field model utilizes partial information about a wind field to generate the final field by means of empirical relations and in compliance with certain boundary conditions. In the present case, partial information is supplied by the properties of the incoming flow. For flat terrain it is provided for example by a one-dimensional boundary layer model, for complex terrain by a (diagnostic) wind field model for the mesoscale.

In the near wake of an obstacle, empirical relations about the form of the wind field are applied. A divergence-free flow parallel to the boundary surfaces defines the boundary conditions. This yields the following tasks:

1. Take a wind field that describes the flow without buildings (zero field \mathbf{u}_0).
2. Add a recirculation field \mathbf{R} that reflects the recirculation zones observed in wind tunnel experiments (empirical wind field $\mathbf{u} = \mathbf{u}_0 + \mathbf{R}$).
3. Find a wind field that agrees as close as possible with the empirical one and that obeys all constraints and boundary conditions (diagnostic wind field \mathbf{v}).
4. Set up additional fields to account in a dispersion calculation for the enhanced turbulence induced by the buildings.

The third step can be formulated as mathematical variation problem. Its solution is described in appendix A.

3 Model

From the mathematical point of view, the recirculation zone in the near wake of a building represents a rotation of the wind field. The derivation of the diagnostic wind field \boldsymbol{v} from the empirical one \boldsymbol{u} does not change the rotation and the zero field does not contain a rotation.² Hence, the required rotation must be produced by the recirculation field \boldsymbol{R} solely. The following constraints apply:

- The recirculation field (and the diagnostic wind field) should not depend on the orientation of the calculation grid because in general it is not possible to align it according to the building axes.
- The recirculation field should be independent of whether and how complex buildings structures are represented by simpler elements. Therefore its derivation cannot be based on characteristic building shapes or extensions,³ especially as such a classification may be ambiguous in complex situations.
- To allow a specification of buildings in rastered form, the recirculation field further away from a building should not depend on whether the walls are defined as plain surfaces or in form of tilted elements.
- The diagnostic wind field should show reasonable agreement with standard situations as measured in the wind tunnel. The same holds for the concentration distributions obtained from the wind and turbulence fields in combination with a dispersion model.
- For complex situations (e.g. densely built-up areas) it is preferable to calculate in case of ambiguities without recirculation rather than with one that does not reflect the real situation.

The first three conditions are important for an integration into a standardized dispersion model like AUSTAL2000 as they yield results that are to a large extent independent of the kind of representation of the buildings. In addition, they allow to resolve buildings internally on the calculation grid with the advantage that inaccurate specifications of the building shapes (like overlaps or small gaps) are corrected without the need of complex algorithms.

3.1 Near wake

Following the approach in LASAT, the recirculation is defined with the help of a field that corresponds to an electrical field caused by a homogeneous charge distribution located at the lee-side wall of a building. In doing so, several of the constraints listed before are satisfied automatically.

²Despite the rotation that is produced by the vertical profile of the Prandtl layer.

³This approach is pursued by the DMW model (VDI 3783 part 10).

Only faces at the lee side of the building are considered, i.e. for which $\mathbf{n}_i \cdot \mathbf{u}_0 > 0$, where \mathbf{u}_0 is the given zero field (e.g. a homogeneous field) and \mathbf{n}_i is the normal of the wall area with index i (pointing outside the building). The homogeneous charge assigned to this area is $\rho_i = 2(\mathbf{n}_i \cdot \mathbf{u}_0)/|\mathbf{u}_0|$ and the resulting field is denoted by \mathbf{g}_i . The total field \mathbf{E} is the superposition of all partial fields \mathbf{g}_i ,

$$\mathbf{E}(\mathbf{r}) = \sum_i \mathbf{g}_i(\mathbf{r}) \quad \text{with} \quad \mathbf{g}_i(\mathbf{r}) = \frac{\rho_i}{4\pi} \int_{\mathcal{A}_i} \frac{\mathbf{r} - \mathbf{a}}{|\mathbf{r} - \mathbf{a}|^3} d^2a. \quad (1)$$

The integral runs over all points \mathbf{a} of area \mathcal{A}_i . In order to ensure vanishing normal components of \mathbf{E} at the ground, the sum covers also the fields produced by the mirror areas \mathcal{A}'_i that result from a reflection of \mathcal{A}_i at the ground.

The field \mathbf{E} has the following properties:

- It is divergence-free.
- In the centre of an isolated wall its direction is perpendicular to the wall and its absolute value approaches unity at the wall.
- Its extend scales with the total area of the wall.
- It does not depend on whether and how the area of the wall face is subdivided into smaller faces (superposition principle).
- At some distance from the wall its form does not depend on whether the base of the wall is defined in its exact shape or in rastered form.

The recirculation field \mathbf{R} is obtained by trimming \mathbf{E} :

Step 1: Reduction of the z -component,⁴

$$\mathbf{E}_1 = (\mathbf{I} - a_5 \mathbf{z}\mathbf{z}) \cdot \mathbf{E}. \quad (2)$$

Step 2: Enhancement of the component parallel to the undisturbed flow direction,

$$\mathbf{E}_2 = \left(\frac{\mathbf{E}_1 \cdot \mathbf{u}_0}{|\mathbf{E}_1| |\mathbf{u}_0|} \right)^{\frac{a_2}{|\mathbf{E}_1|}} \mathbf{E}_1. \quad (3)$$

Step 3: Limitation of the range of absolute values,

$$\mathbf{E}_3 = \min(a_3, |\mathbf{E}_2|) \frac{\mathbf{E}_2}{|\mathbf{E}_2|} \quad \text{and} \quad \mathbf{E}_3 = 0 \quad \text{for} \quad \mathbf{E}_2 < a_4. \quad (4)$$

⁴Vectors written side by side without operator symbol form a tensor. The components of \mathbf{ab} are $[\mathbf{ab}]_{ij} = a_i b_j$, the scalar product is $[\mathbf{ab} \cdot \mathbf{cd}]_{ij} = \sum_k a_i b_k c_k d_j$, and the twofold scalar product is $\mathbf{ab} \cdot \cdot \mathbf{cd} = \sum_{i,j} a_i b_j c_j d_i$. The unity tensor is denoted by \mathbf{I} , i.e. $I_{ij} = \delta_{ij}$.

Step 4: Scaling with the mean speed of the incoming flow,

$$\mathbf{R} = -a_1 \bar{u}_0 \mathbf{E}_3 . \quad (5)$$

The mean speed of the incoming flow \bar{u}_0 in the last step results from the local zero field averaged vertically over $|\mathbf{E}_3|$.

The first two steps introduce a rotation into the field so that in the diagnostic field a vortex can develop at the lee side. The enhancement in step 2 stretches the field along the undisturbed flow direction. Here, reduction of the z -component in step 1 prevents the field from being reduced too strongly near the top of the building. The factors a_1 and a_3 in the last two steps determine size and magnitude of the recirculation.⁵ The factors (mainly the product $a_1 a_3$, a_2 , and a_5) were fixed by comparisons with experimental data sets.

The following safety precautions were introduced to improve robustness of the model in practice and to avoid artefacts for complex built-up structures:

1. The buildings are represented internally only in rastered form on the calculation grid in order to correct in a reliable way imprecise building specifications like overlaps or small gaps. Hence, the partial areas \mathcal{A}_i always have the orientation and extend of the cell faces of the grid.⁶ This procedure is justified by the fact that exact and rastered building shapes yield almost the same wind fields as demonstrated in the verification tests.
2. In order to account for shadowing effects of other buildings, the field produced by area \mathcal{A}_i only acts on grid meshes that are visible from that area.⁷
3. The total field \mathbf{R} is restricted to the overall geometrical lee produced by the zero field.

The steps that yield the diagnostic wind field \mathbf{v} are depicted schematically in Fig. 1.

3.2 Prandtl layer and frontal vortex

Usually, the given zero field usually a Prandtl layer. If such a flow approaches an obstacle, a frontal vortex develops. Origin of the vortex is the pressure gradient that is produced by the vertically inhomogeneous incoming flow. In contrast, a vertically homogeneous incoming flow does not produce a frontal vortex (see HOSKER, 1984). In the vicinity of the obstacle the

⁵The cut-off parameter a_4 has only little influence on the result provided that it is small enough.

⁶In some of the verification tests, also the exact building shapes were divided in partial faces of cell face size for consistency.

⁷For every grid cell it is checked whether the connection line between its centre point and the centre point of the area cuts a grid cell that is part of a building, the latter point being shifted by half a mesh width in flow direction.

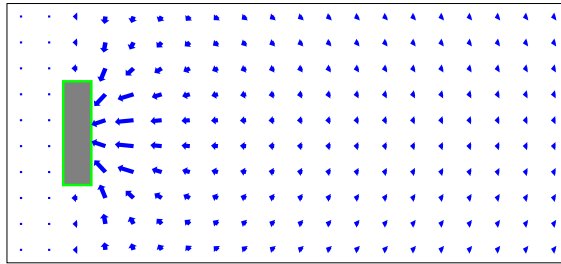
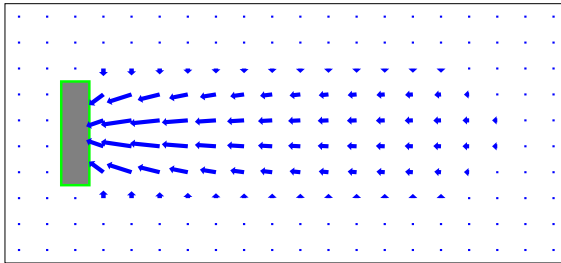
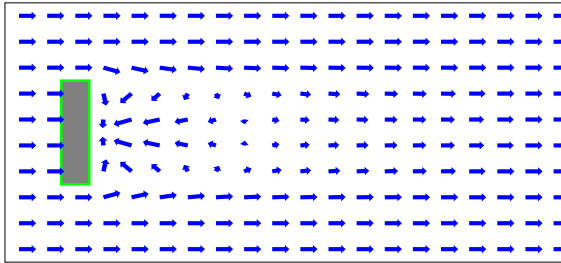
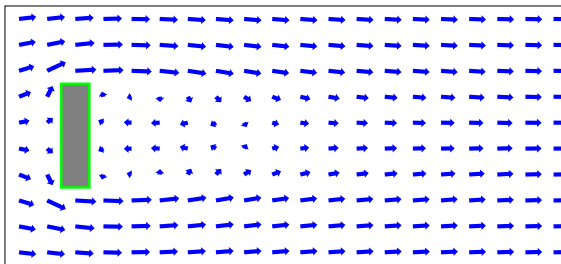
1. Construction of field E .2. Setup of the recirculation field R .3. Addition to the zero field u_0 .4. Calculation of the diagnostic wind field v .

FIGURE 1: Calculation of the diagnostic wind field for an obstacle located in a cross flow approaching from the left side.

vortex extends to about 50% to 60% of the obstacle height, further in front of the obstacle its vertical extend depends on the vertical profile of the incoming flow. The horizontal extend of the frontal vortex is determined by the obstacles height and its extension perpendicular to the flow direction.

A vertically inhomogeneous zero field contains a rotation which is conserved in the calculation of the diagnostic wind field. In the near wake, this initial rotation must be compensated for in order to avoid the appearance of an artificial flow in direction of the incoming one. In contrast, in front of the obstacle the initial rotation produces – very much like in nature – a frontal vortex in the diagnostic wind field with dimension and magnitude similar to the observed one.

Therefore, when adding the recirculation field the zero field is replaced at all locations with non-vanishing recirculation field (i.e. primarily in the wake of the obstacle) by a vertically constant field \bar{u}_0 (the zero field vertically averaged over the recirculation field) .

3.3 Enhanced turbulence produced by the building

The flow around a building causes an enhanced turbulence and diffusion in the wake zone which can be accounted for in an dispersion calculation by means of additional fields for the velocity fluctuations and diffusion coefficients. Similar to the procedure in LASAT, these additional fields are set up on the basis of the recirculation field. The additional velocity fluctuations are defined as

$$\hat{\sigma}_{u,v,w}(\mathbf{r}) = \sqrt{|E_2(\mathbf{r})|} f_s \bar{u}_0(\mathbf{r}) , \quad (6)$$

and the addition diffusion coefficients in the form

$$\hat{K}_{h,v}(\mathbf{r}) = f_k \bar{h} \hat{\sigma}_u(\mathbf{r}) . \quad (7)$$

Here, \bar{u}_0 is again the vertically averaged zero field, f_s and f_k are coefficients of order unity and \bar{h} denotes the average height of the buildings.

In analogy to the setup of the recirculation field, the square root of $|E_2|$ is restricted to values smaller a_3 and set to zero for values smaller a_4 . Hence, the maximum value of $\hat{\sigma}_{u,v,w}$ is $a_3 f_s \bar{u}_0$ and the one of $\hat{K}_{h,v}$ accordingly $a_3 f_s f_k \bar{h} \bar{u}_0$.

Like the recirculation field, the additional fields are confined to the geometrical wake produced by the zero field. However, for a better agreement with experimental observations they are extended above the top of the building with a linearly decreasing magnitude down to zero at h_s times the building height, and horizontally the geometrical wake is enlarged to an opening angle of a_s degree.

4 Verification and Validation

Task of the verification is to test whether a model has the properties it was designed for. For the present case, important properties are independence of the type of building specification (e.g. split up into smaller elements or definition in rastered form) and the orientation of the calculation grid.

The validation demonstrates the agreement between model results and measurements. Here, wind fields were tested as well as concentration fields derived from the wind and turbulence fields in combination with a dispersion calculation. Because no experimental data sets were available for a source height between 1.2 and 1.7 times the building height – the desired application range – a comparison with results from the prognostic wind field model MISKAM was carried out for this range instead.

All calculations were performed with the following set of parameter values that was derived beforehand in a series of test calculations:

a_1	6
a_2	1
a_3	0.3
a_4	0.05
a_5	0.7
f_s	0.5
f_k	0.3
h_s	1.2
a_s	15

As demonstrated in appendix B, the concentration distributions near ground are not very sensitive to the exact setting of a specific parameter value.

The following symbols are used in the description of the test calculations:

h_A	Anemometer (measurement) height (m)
H	Building height (m)
H_Q	Source height (m)
r	Direction of the incoming flow (degree)
u_A	Wind speed of the initial field at height h_A (m/s)
u_*	Friction velocity (m/s)
Δx	Horizontal mesh width (m)
Δz	Vertical mesh width near ground (m)
z_0	Roughness length (m)
d_0	Displacement height (m)

Beside the first verification tests, buildings are always resolved on the calculation grid (rastered shapes). The tests in section 4.1.2 and 4.1.3 show that rastered and exact shapes yield almost the same results, provided that the grid meshes are not too large.

The initial (zero) field was set in conformance with the *TA Luft*, appendix 3, section 8.1 according to guideline VDI 3783 part 8. For the comparisons with results from wind tunnel measurements, neutral stability (Klug/Manier class III/1) was assumed and wind shear was omitted.

In the graphical visualizations of the wind fields, blue arrows denote the calculated diagnostic wind field and red arrows the measurement results. Grid cells that are part of a building are shown with gray background, green lines denote the exact building shapes. In most cases, the pictures show only part of the calculation area, for symmetric configurations they contain only one half of the calculation area. Some captions specify the time step τ that was used to derive the length of the wind arrow (τv , where v is the horizontal respectively vertical projection of the wind vector).

The sources in the dispersion calculations were assumed to be passive so that effective source height and construction height are the same.⁸

⁸In nature, the plume emitted from a stack is subject to momentum or thermal rise, the effective source height is thus larger than the construction height.

4.1 Verification

4.1.1 Partition of a building complex into simpler elements

It is tested whether the diagnostic wind field is independent of the partition of a building complex into simpler elements.

Two adjacent buildings are defined once as 2 cuboids and once as an ensemble of 8 cuboids. The recirculation field is calculated in both cases from the exact building shapes. Figs. 2 and 3 show that the resulting diagnostic wind fields are identical.

($H = 25$ m, $\Delta z = 2$ m, $\Delta x = 5$ m, $u_A = 5$ m/s, $r = 250$ deg, vertically homogeneous incoming flow)

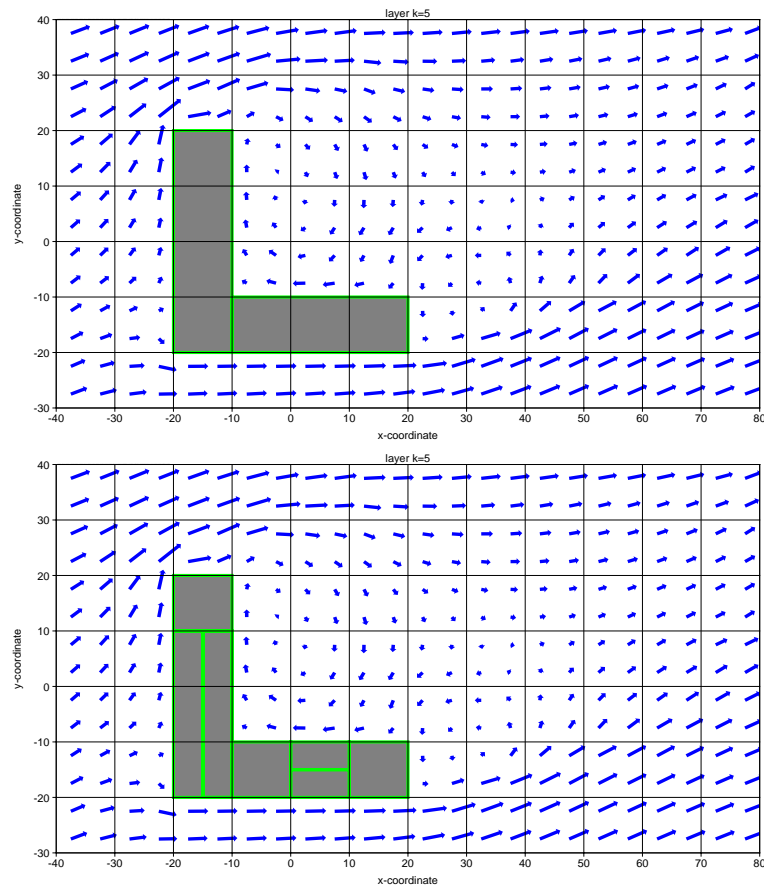


FIGURE 2: Test: Partition of a building complex into simpler elements (horizontal cut at $z = 9$ m). Top: 2 cuboids. Bottom: 8 cuboids (in this layer only 7 are visible).

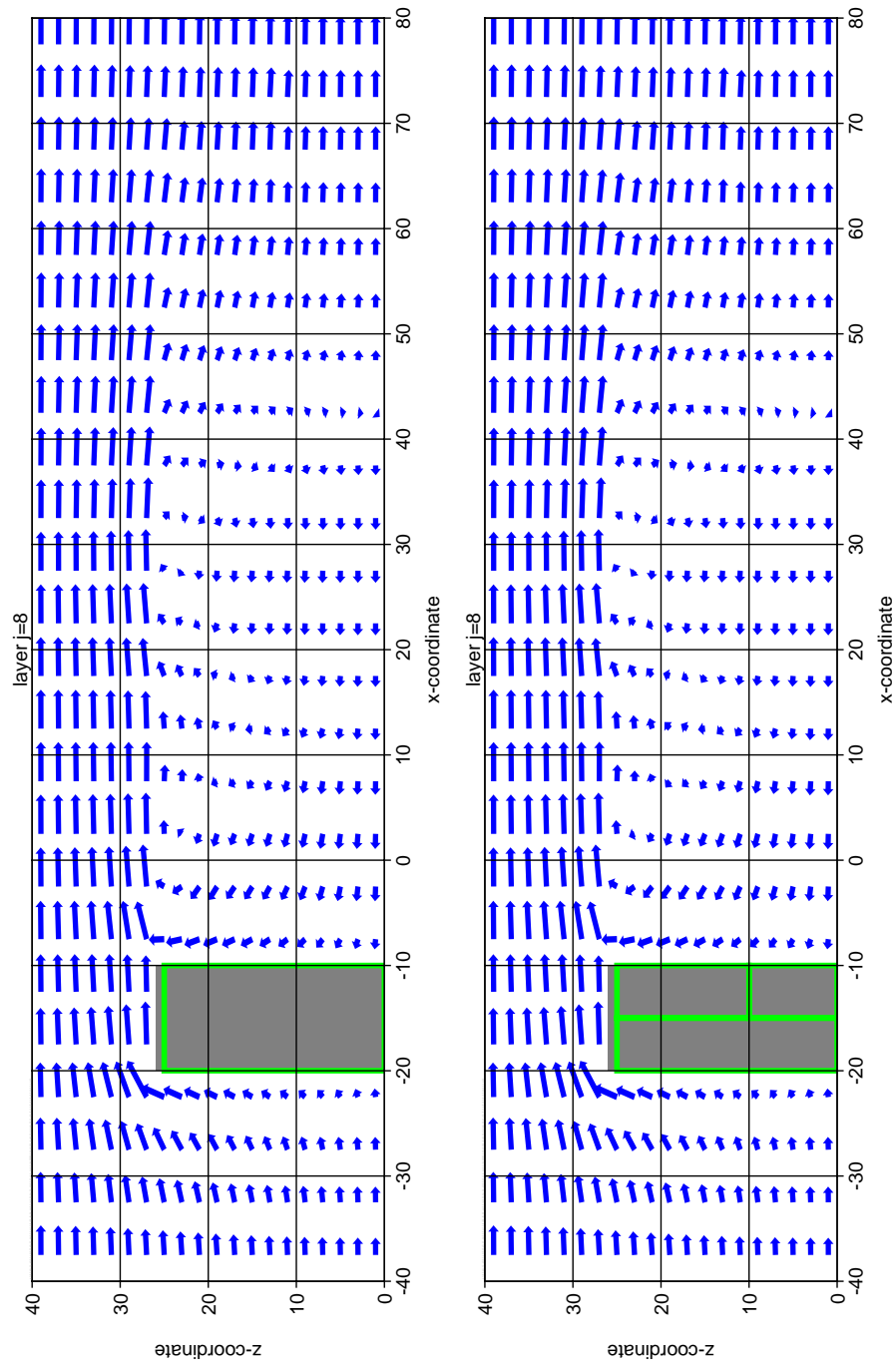


FIGURE 3: Test: Partition of a building complex into simpler elements (vertical cut at $y = 7.5$ m).
Top: 2 cuboids. Bottom: 8 cuboids (in this layer only 3 are visible).

4.1.2 Rastering of a building with rectangular base

It is tested whether the diagnostic wind field is more or less the same if a building with rectangular base is modelled in its exact and in rastered form.

A building row oriented at an angle with respect to the calculation grid is specified once in its exact and once in rastered form for the calculation of the recirculation field. The test is performed at the raster limit, where the width of the building row has an extend of only one mesh width. Three directions of the incoming flow are applied: perpendicular to the row (225 deg) and tilted (270 deg and 290 deg).

Except for the vicinity of the walls, the wind fields in the wake agree well, see Figs. 4 to 6. Only for the very tilted flow of 290 deg, more pronounced differences appear, but they should not be relevant in practice, where a smaller mesh width would be used.

($H = 25$ m, $\Delta z = 2$ m, $\Delta x = 5$ m, $u_A = 5$ m/s, vertically homogeneous incoming flow)

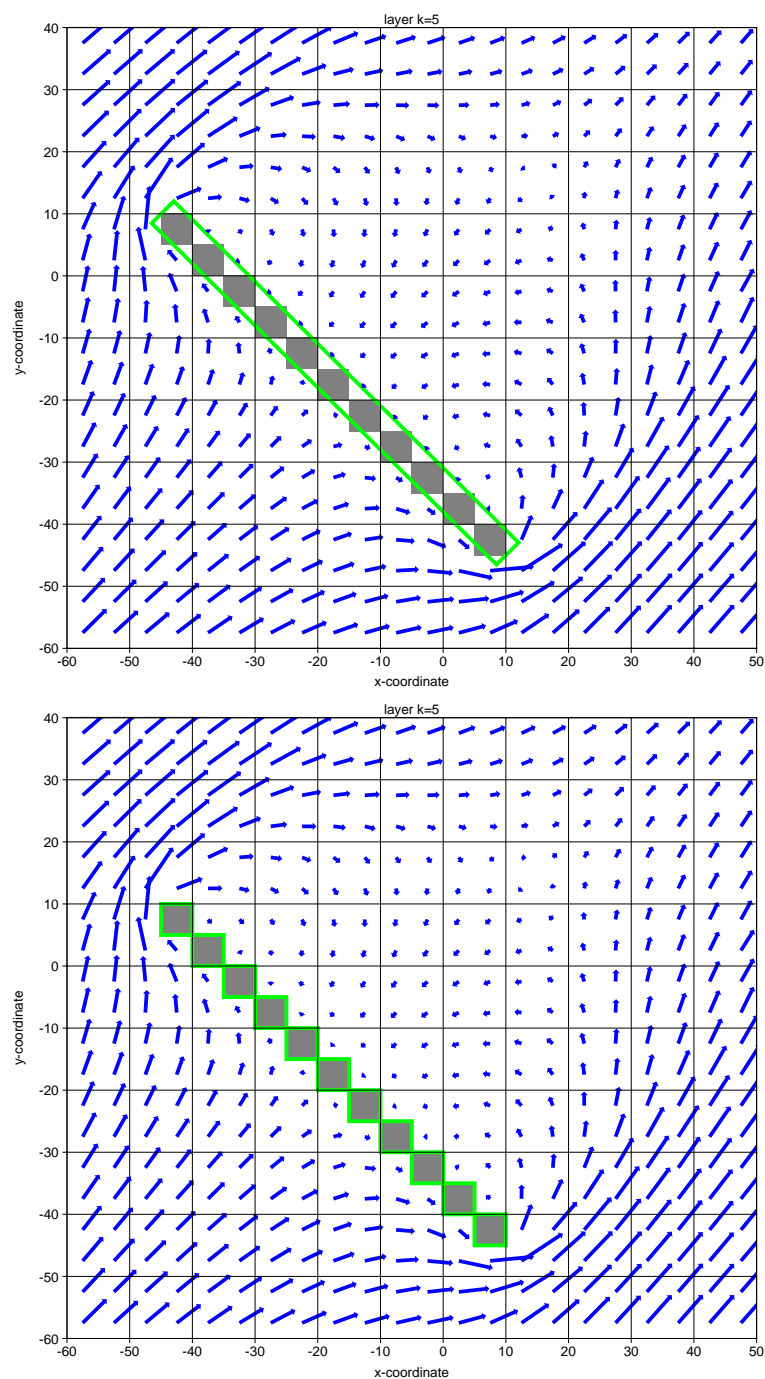


FIGURE 4: Test: Rastering of a building with rectangular base (flow direction 225 deg, horizontal cut at $z = 9$ m). Top: Wind field derived from the exact building shape. Bottom: Wind field derived from the rastered building shape.

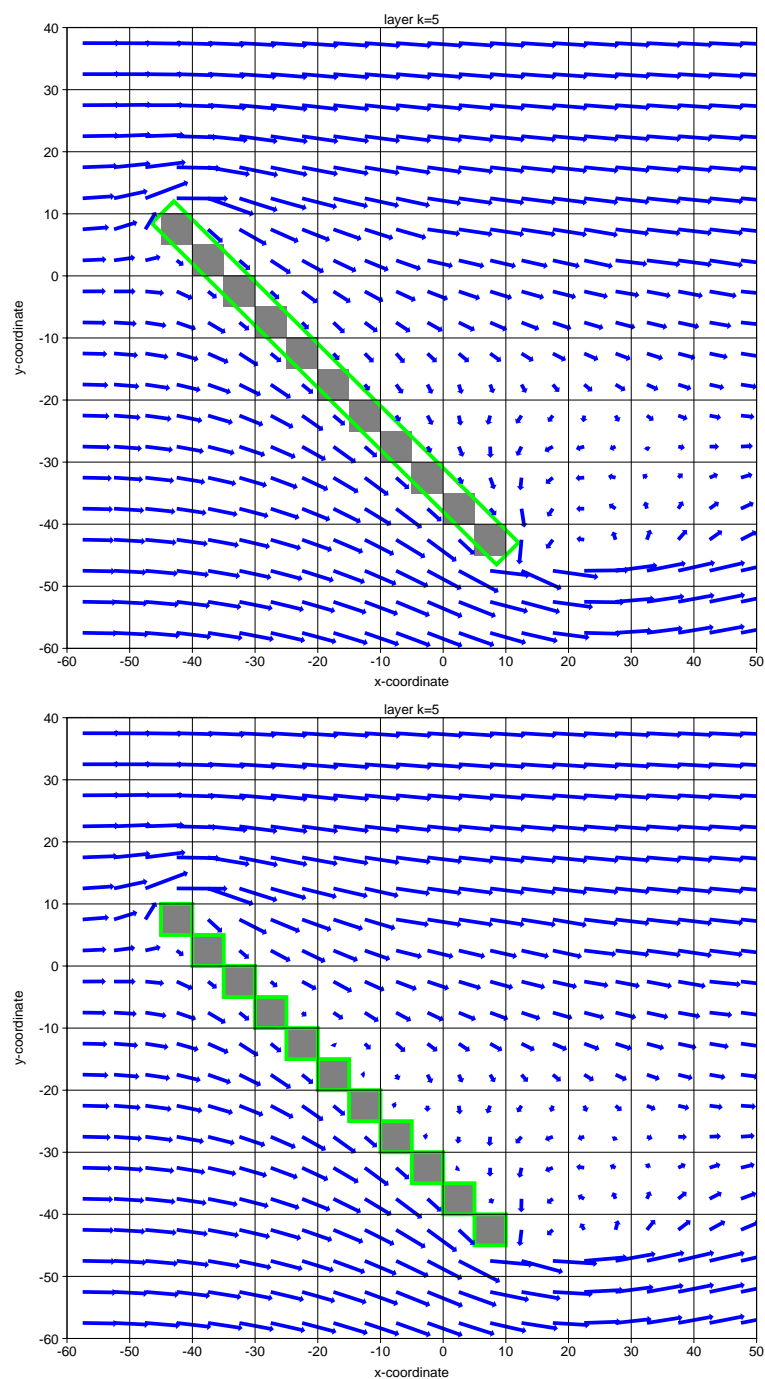


FIGURE 5: Test: Rastering of a building with rectangular base (flow direction 270 deg, horizontal cut at $z = 9$ m). Top: Wind field derived from the exact building shape. Bottom: Wind field derived from the rastered building shape.

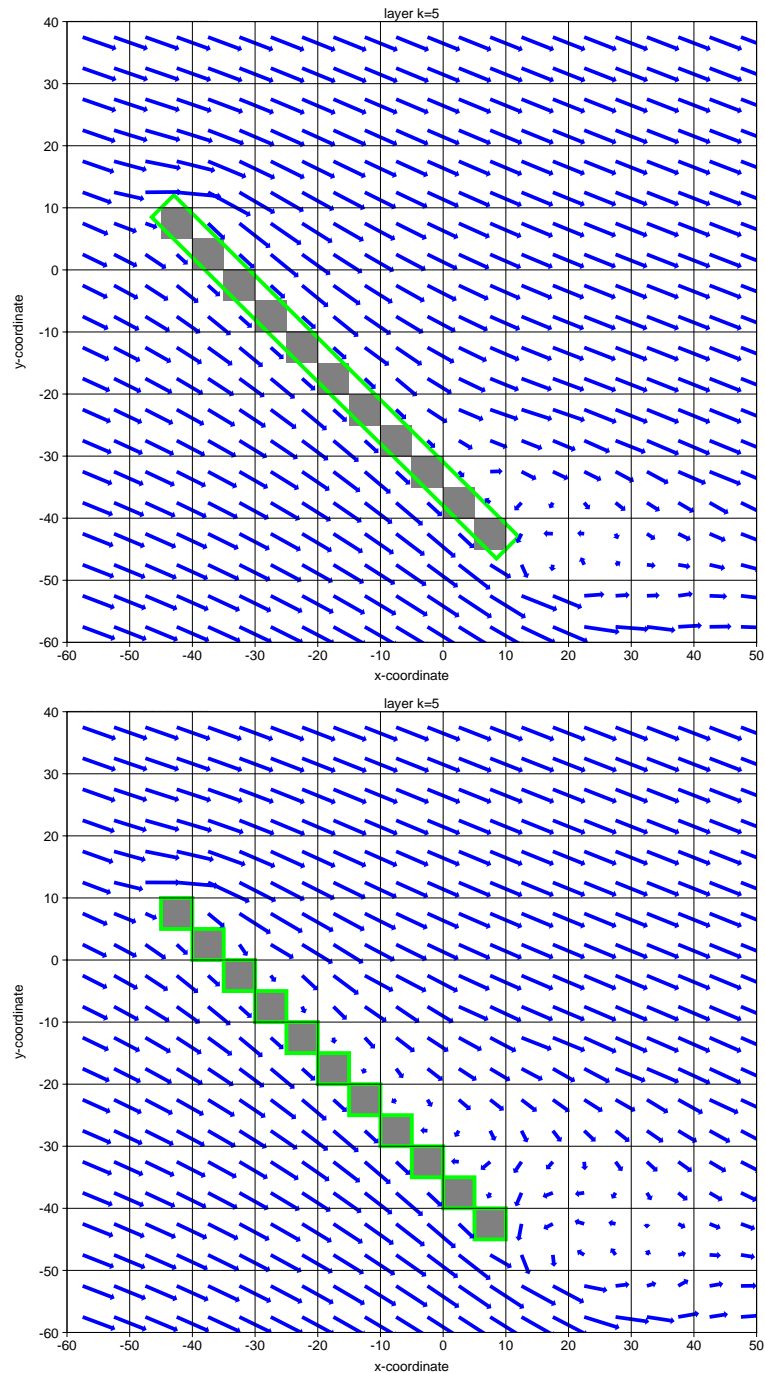


FIGURE 6: Test: Rastering of a building with rectangular base (flow direction 290 deg, horizontal cut at $z = 9$ m). Top: Wind field derived from the exact building shape. Bottom: Wind field derived from the rastered building shape.

4.1.3 Rastering of a building with circular base

It is tested whether the diagnostic wind field is more or less the same if a building with circular base is modelled in its exact and in rastered form.

A cylindrical building is applied in its exact and in rastered form for the calculation of the recirculation field. The resulting wind fields show good agreement, see Figs. 7 and 8.

(cylinder diameter 80 m, $H = 160$ m, $\Delta z = 20$ m, $\Delta x = 20$ m, $u_A = 5$ m/s, $h_A = 13$ m, $z_0 = 0.5$ m, $d_0 = 3$ m)

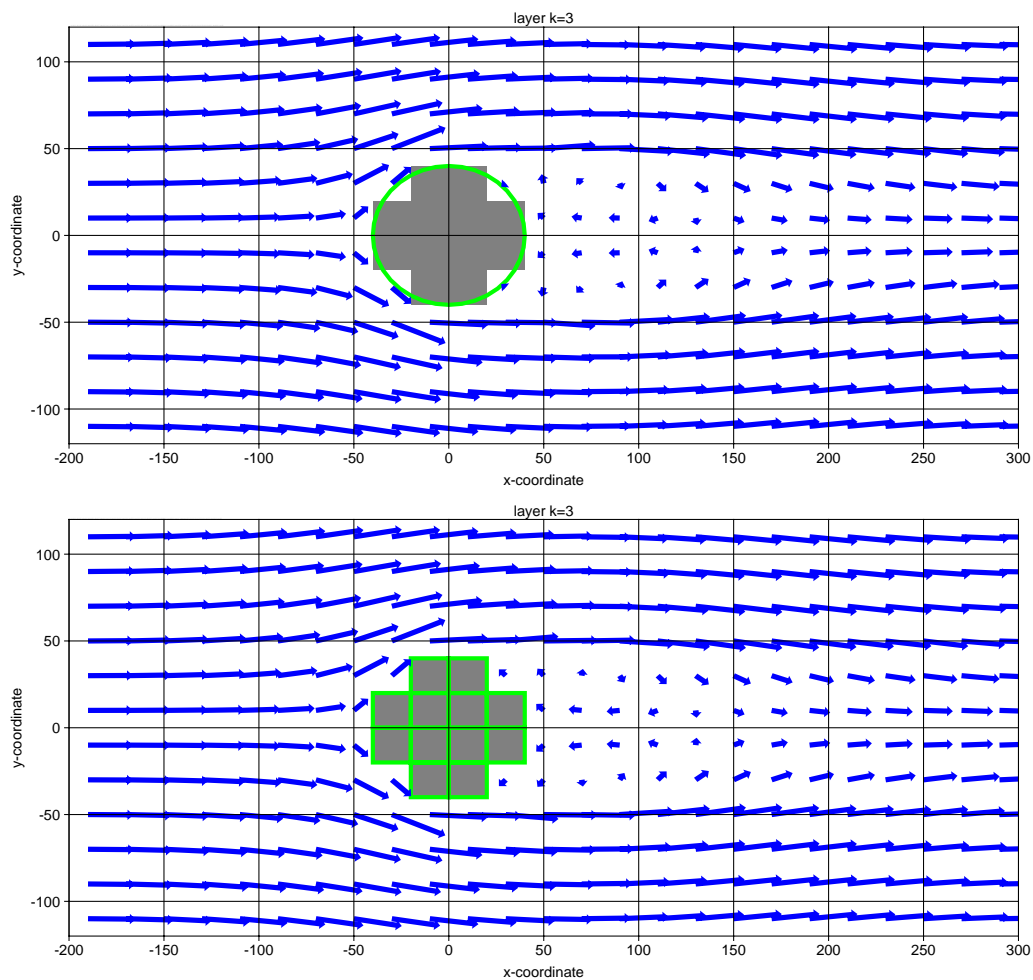


FIGURE 7: Test: Rastering of a building with circular base (horizontal cut at $z = 50$ m). Top: Wind field derived from the exact building shape. Bottom: Wind field derived from the rastered building shape.

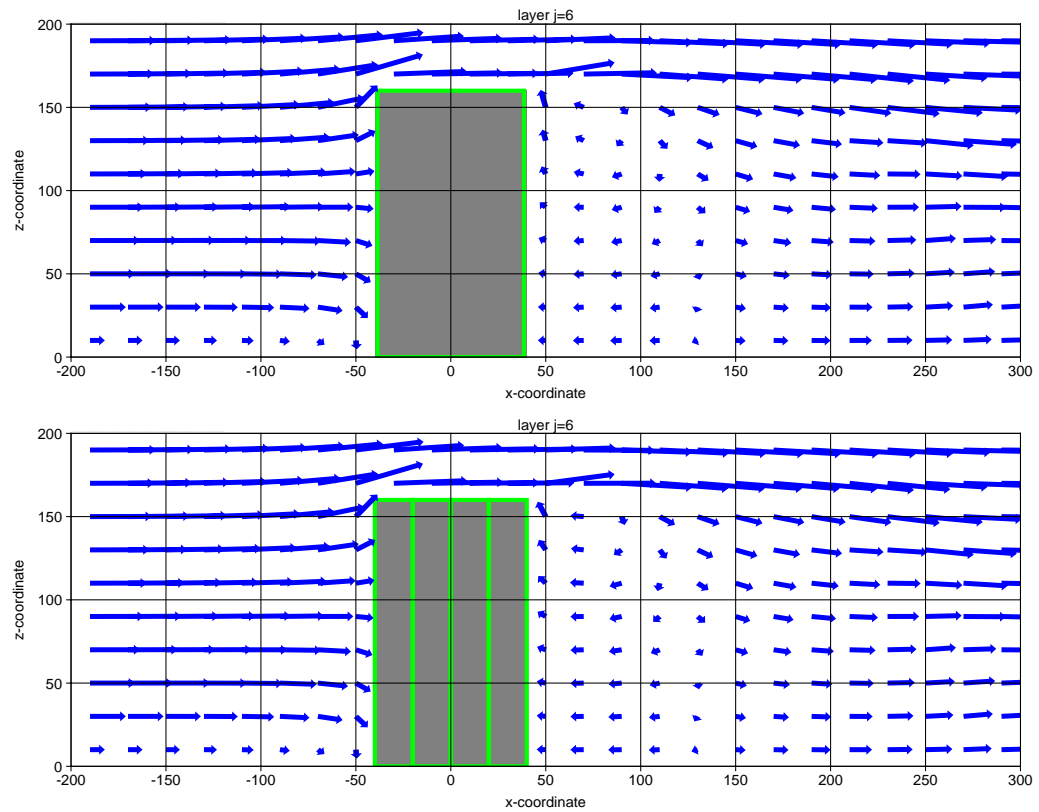


FIGURE 8: Test: Rastering of a building with circular base (vertical cut at $y = -10$ m). Top: Wind field derived from the exact building shape. Bottom: Wind field derived from the rastered building shape.

4.1.4 Orientation of the calculation grid, influence on the wind field

It is tested whether the diagnostic wind field is independent of the orientation of the calculation grid with respect to the building orientation.

The wind field in the wake of a cuboidal building is calculated for different orientations of the calculation grid. The incoming flow is always perpendicular to the building wall. Fig. 9 shows as an example the wind field for two different orientations. The velocity component in direction of the incoming flow is determined at 10 m height in the central lee at distances of 20 m, 40 m, 60 m, 80 m, 100 m, and 120 m from the lee-side face. The coordinate system of the calculation grid is rotated in steps of 5 degree from 0 degree (incoming flow along the x axis) to 90 degree (incoming flow along the y axis).

The results in Fig. 10 show that the recirculation in the wake of the building is independent of the orientation angle. There are fluctuations, but small and without systematic tendency.⁹

(Base area 63 m times 63 m, $H = 30$ m, $\Delta z = 3$ m, $\Delta x = 3$ m, $u_A = 2$ m/s, $h_A = 10$ m, $z_0 = 0.1$ m)

⁹A negative result of this verification test was one of the main reasons why the VDI model DMW was not implemented into AUSTAL2000, see the final report on AUSTAL2000.

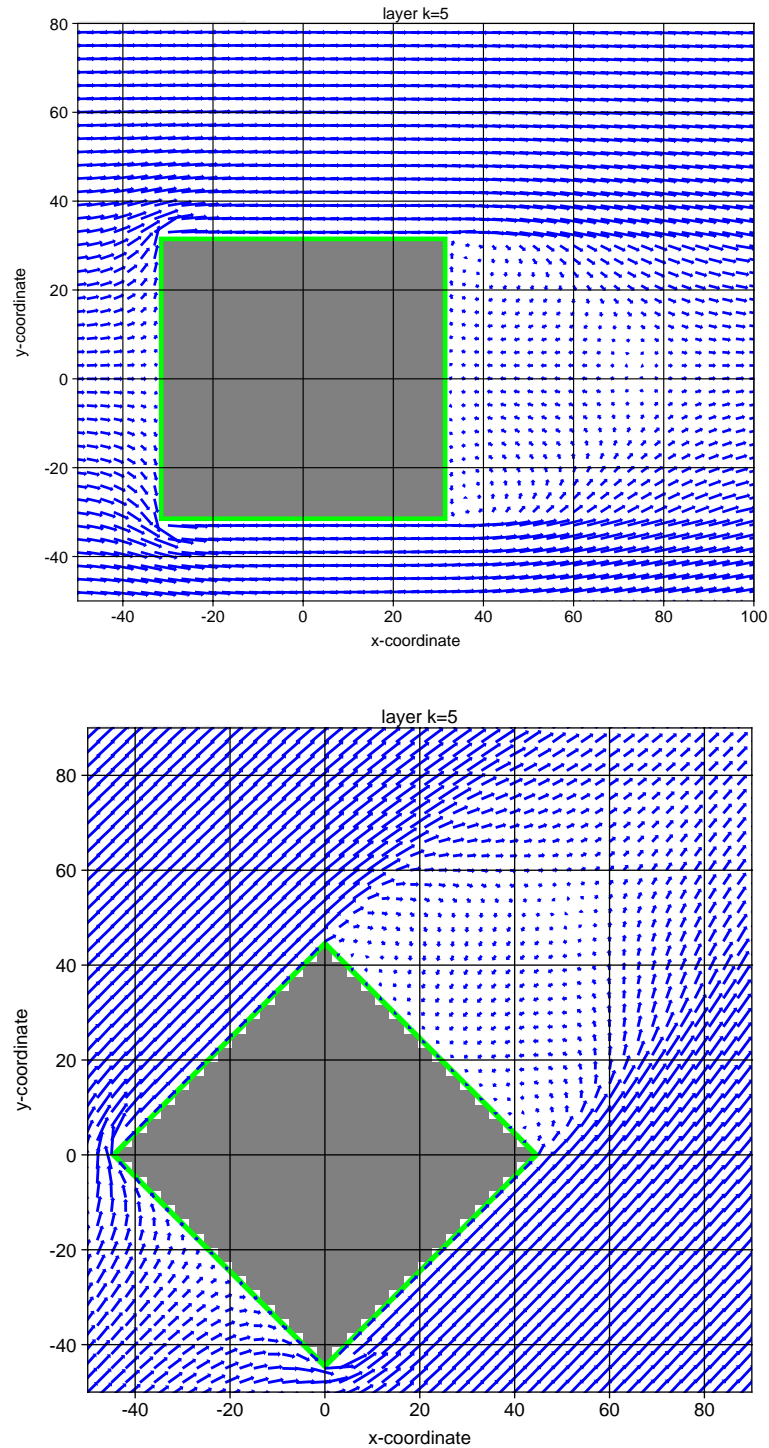


FIGURE 9: Test: Orientation of the calculation grid. Example wind fields for two orientations of the calculation grid with respect to the building (0 deg and 45 deg, horizontal cut at $z = 13.5$ m).

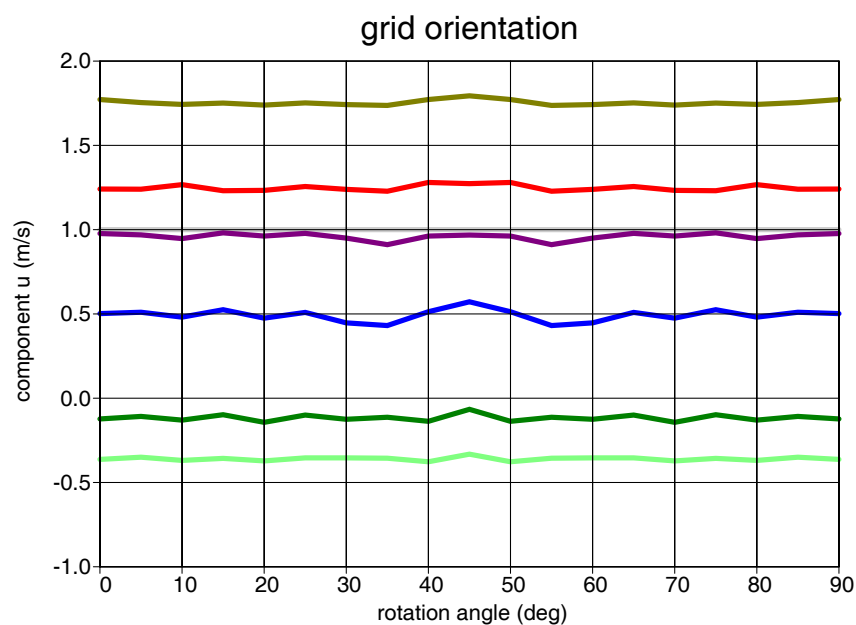


FIGURE 10: Test: Orientation of the calculation grid. Velocity component in direction of the incoming flow at 10 m height in the central lee at distances of 20 m, 40 m 60 m, 80 m 100 m, and 120 m from the lee-side wall for different rotation angles of the calculation grid with respect to the incoming flow direction.

4.1.5 Orientation of the calculation grid, influence on the concentration distribution

It is tested whether the concentration distribution resulting from the model fields is independent of the orientation of the calculation grid with respect to the building orientation.

The concentration distribution for a source next to the building is calculated as average over an isotropic wind rose. Source and building are aligned once parallel and once tilted with respect to the calculation grid.

The results in Fig. 11 show that the concentration distributions are virtually the same in both cases, differences being of the order of the statistical uncertainty (between 1 % and 4 %).

(Building extensions 12 m and 44 m, $H = 30$ m, $H_Q = 36$ m, $\Delta z = 3$ m, $\Delta x = 4$ m, $u_A = 3$ m/s, $h_A = 13$ m, $z_0 = 0.5$ m, $d_0 = 3.0$ m)

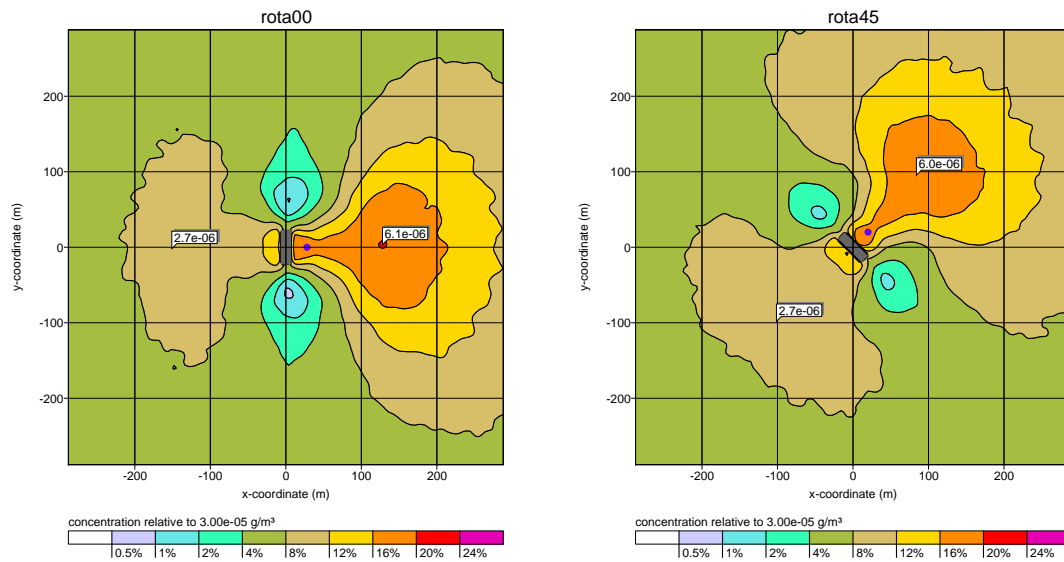


FIGURE 11: Test: Orientation of the calculation grid. Near ground concentration averaged over an isotropic wind rose for two orientations of source and building with respect to the calculation grid. The blue point denotes the source location.

4.2 Validation of the wind fields

4.2.1 Data sets of the guideline draft VDI 3783 part 9

The guideline draft VDI 3783 part 9, *Prognostic Wind Field Models for the Micro Scale, Evaluation of the Flow around Buildings and Obstacles*, contains test data sets for the validation of prognostic wind field models. They can be applied as well to a diagnostic wind field model.

For a comparison of measured and calculated wind fields the draft envisions the derivation of hit rates as a measure of agreement for the Cartesian velocity components. The hit rates are calculated for the total calculation area and for the near field as specified in the draft.

In practice this approach revealed the following shortcomings:

- Not the original fields but the fields scaled by the wind speed at a given reference point are compared, so that in certain cases systematic deviations may not be reflected in the hit rate.
- The hit rates are calculated separately for every Cartesian component of the wind vector. This can lead to good hit rates even though severe qualitative differences exist in the wind fields.
- The hit rates depend on the location of measurement points within the evaluation area whose extension is specified in form of a rectangle.
- Hit rates can be calculated only for the data sets of the draft because only for these the necessary evaluation parameters are specified.

As an additional or alternative measure of agreement one can analyze the correlation between the wind fields. The correlation coefficient k is often used to determine the agreement between two sets of scalar quantities x_i and y_i ,

$$k = \frac{\sum x_i y_i}{\sqrt{\sum x_i^2 \sum y_i^2}} . \quad (8)$$

But good correlation does not exclude systematic differences. Assuming that all values of data set x_i are scaled by a factor s , the value of s that gives least squares fitting with respect to data set y_i is

$$s = \frac{\sum x_i y_i}{\sum x_i^2} . \quad (9)$$

Values $s < 1$ imply that the absolute values of x_i systematically exceed the ones of y_i , even in case of perfect correlation.

This concept can be extended to data sets of vectorial quantities like the measured and calculated wind vectors \mathbf{o}_i and \mathbf{v}_i , respectively. In addition, a weighting factor w_i is introduced

which allows to distinguish in a formal way between disturbed and undisturbed parts (near field and far field) of the wind field. The weighting factor depends on the mean velocity of the incoming (undisturbed) flow U and the measured wind vector \mathbf{o}_i :

$$w_i = \begin{cases} 1 - \frac{\mathbf{o}_i \cdot \mathbf{U}}{|\mathbf{o}_i| |\mathbf{U}|} & \text{selects the disturbed parts} \\ 1 + \frac{\mathbf{o}_i \cdot \mathbf{U}}{|\mathbf{o}_i| |\mathbf{U}|} & \text{selects the undisturbed parts} \end{cases} \quad (10)$$

The generalized coefficients k and s read:

$$k = \frac{\sum \mathbf{v}_i \cdot \mathbf{o}_i w_i}{\sqrt{\sum |\mathbf{v}_i|^2 w_i \sum |\mathbf{o}_i|^2 w_i}} \quad (11)$$

$$s = \frac{\sum \mathbf{v}_i \cdot \mathbf{o}_i w_i}{\sum |\mathbf{v}_i|^2 w_i} \quad (12)$$

The data sets contained in guideline draft VDI 3783 part 9 are listed in the following table. They are based on the so-called CEDVAL data sets (CEDVAL, 2004) produced at the Meteorological Institute of the University of Hamburg (wind tunnel measurements).¹⁰

Data set	Description	CEDVAL source
c1	Quasi 2-dimensional building in a cross flow	A1-3
c3	Cube in a cross flow	A1-4
c4	Cube in a diagonal flow	A1-6
c5	Cuboid in a cross flow	A1-1
c6	Set of 3 times 7 cubes	B1-1

These test scenarios were re-calculated with the wind field model. The following table contains the hit rates according to the guideline draft for the near field (the draft demands at least 66%) and the correlation coefficients both for the disturbed and undisturbed areas.

Data set	q_u (%)	q_v (%)	q_w (%)	k_u	s_u	k_d	s_d
c1 (quasi 2-dimensional building)	46	-	72	-	-	-	-
c3 (cube)	81	85	74	0.99	0.95	0.88	0.83
c4 (diagonal cube)	63	69	58	0.97	0.98	0.37	0.29
c5 (cuboid)	75	82	75	0.98	1.04	0.93	1.16
c6 (3 times 7 cubes)	37	71	66	0.96	0.48	0.54	0.41

¹⁰In the data sets of the draft, some measurement points were omitted and the wind vectors were scaled with the wind speed at a given reference point.

Figs. 12 to 16 contain a graphical comparison of measured and calculated wind fields:

- For the quasi 2-dimensional building (data set c1, Fig. 12), the measured wake zone extends further above the top of the building (up to about 2 building heights) as compared to the calculated one (up to about 1.5 building heights) and the recirculation zone extends further in the direction of the incoming flow (measurement: about 4.5 building heights from the lee-side wall, calculation: about 3.5 building heights). In the near lee and in the front, shape and magnitude of the recirculation are reproduced.
- For the cube in a cross flow (data set c3, Fig. 13), the agreement between measured and calculated wind field is good. Only at the top edge the calculated flow shoots atop of the building a bit too strongly (Fig. 13, bottom).
- For the cube in a diagonal flow (data set c4, Fig. 14), the calculated flow around the side edges ($x = -12.5 \text{ m}/y = 12.5 \text{ m}$ and $x = 12.5 \text{ m}/y = -12.5 \text{ m}$) is relatively smooth before a recirculation develops. In the measurement in contrast, the recirculation sets on directly at the edges. As a consequence, the extend of the calculated recirculation zone across the incoming flow direction is about 25% smaller, which in turn leads to smaller hit rates and correlation coefficients. Along the incoming flow direction, the measured extend is reproduced in the calculation, the magnitude of the recirculating flow is a bit too small.
- The agreement for the cuboid in a cross flow (data set c5, Fig. 15) is equally good as for the cube in a cross flow. The larger amount and higher spatial density of measurement points permit a better quantitative comparison.
- For the set of cubes (data set c6, Fig. 16), the calculated wind flow propagates due to its construction (no recirculation field outside the geometrical wind shadow) more or less undisturbed inside the parallel street canyons. In contrast, the magnitude of the measured flow is reduced by about 50% (Fig. 16, top). The hit rates for the u component and the coefficient s_u are therefore small.

In the side streets, the transition to an opposite flow direction is sharper in the calculated flow than in the measured one. In the calculation, the opposite flow sets on (like in the scenarios c3 and c5) immediately at the wall edge at $y = 15 \text{ m}$, whereas in the measurement it emerges in the centre of the wall at $y = 0 \text{ m}$. This explains as well the differences in the vertical flow (Fig. 16, bottom): As in the measured flow more mass is transported into the wake of the building, more mass must be transferred to the top of the building; hence the measurement shows a larger region with upward-directed flow.

Except for the case c4 with a recirculation zone that is too narrow and the differences discussed for the more complex situation c6, the agreement between calculated and measured wind field is good with most of the hit rates exceeding the required value of 66%.

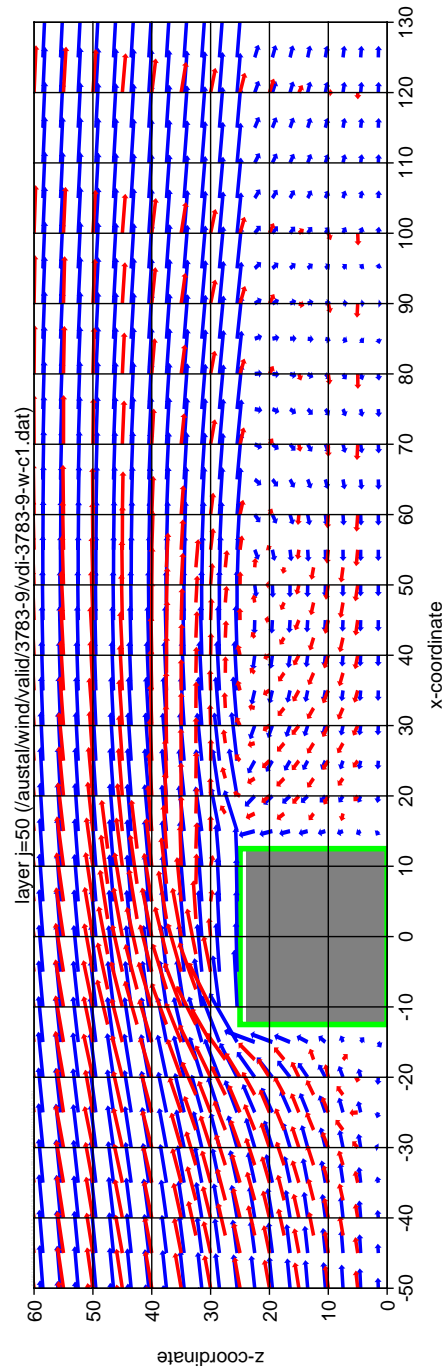


FIGURE 12: Guideline draft VDI 3783 part 9, data set c1, quasi 2-dimensional building in a cross flow (vertical cut at $y = 0$ m).

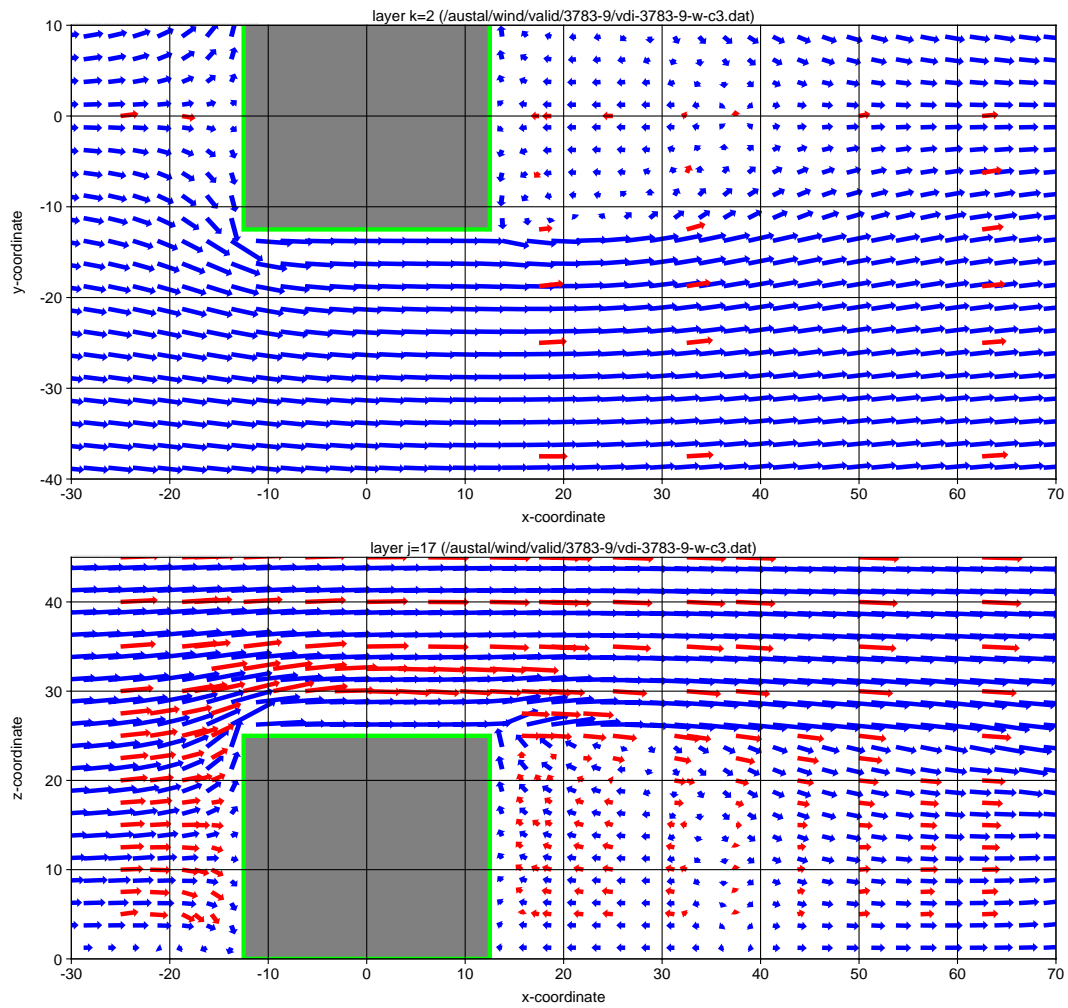


FIGURE 13: Guideline draft VDI 3783 part 9, data set c3, cube in a cross flow. Top: Horizontal cut at $z = 5$ m. Bottom: Vertical cut at $y = 0$ m.

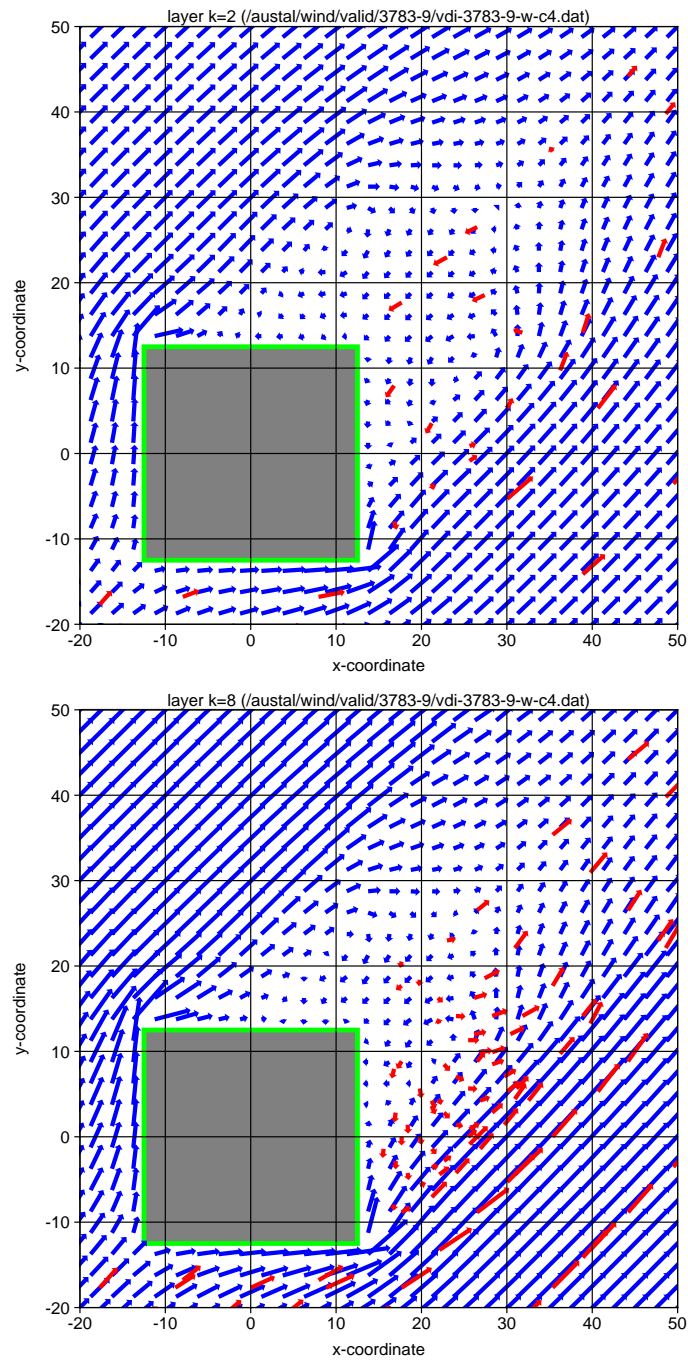


FIGURE 14: Guideline draft VDI 3783 part 9, data set c4, cube in a diagonal flow. Top: Horizontal cut at $z = 5$ m. Bottom: Horizontal cut at $z = 20$ m.

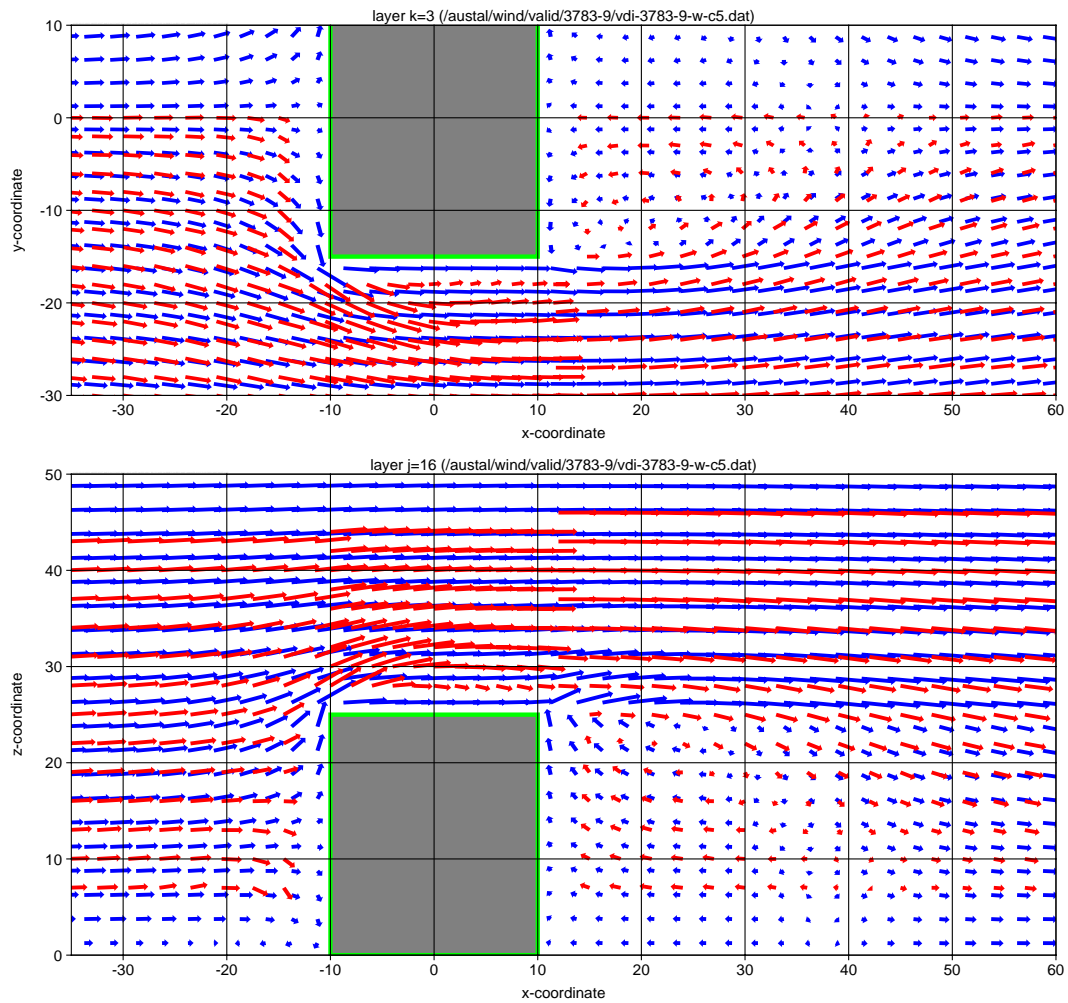


FIGURE 15: Guideline draft VDI 3783 part 9, data set c5, cuboid in a cross flow. Top: Horizontal cut at $z = 7$ m. Bottom: Vertical cut at $y = 0$ m.

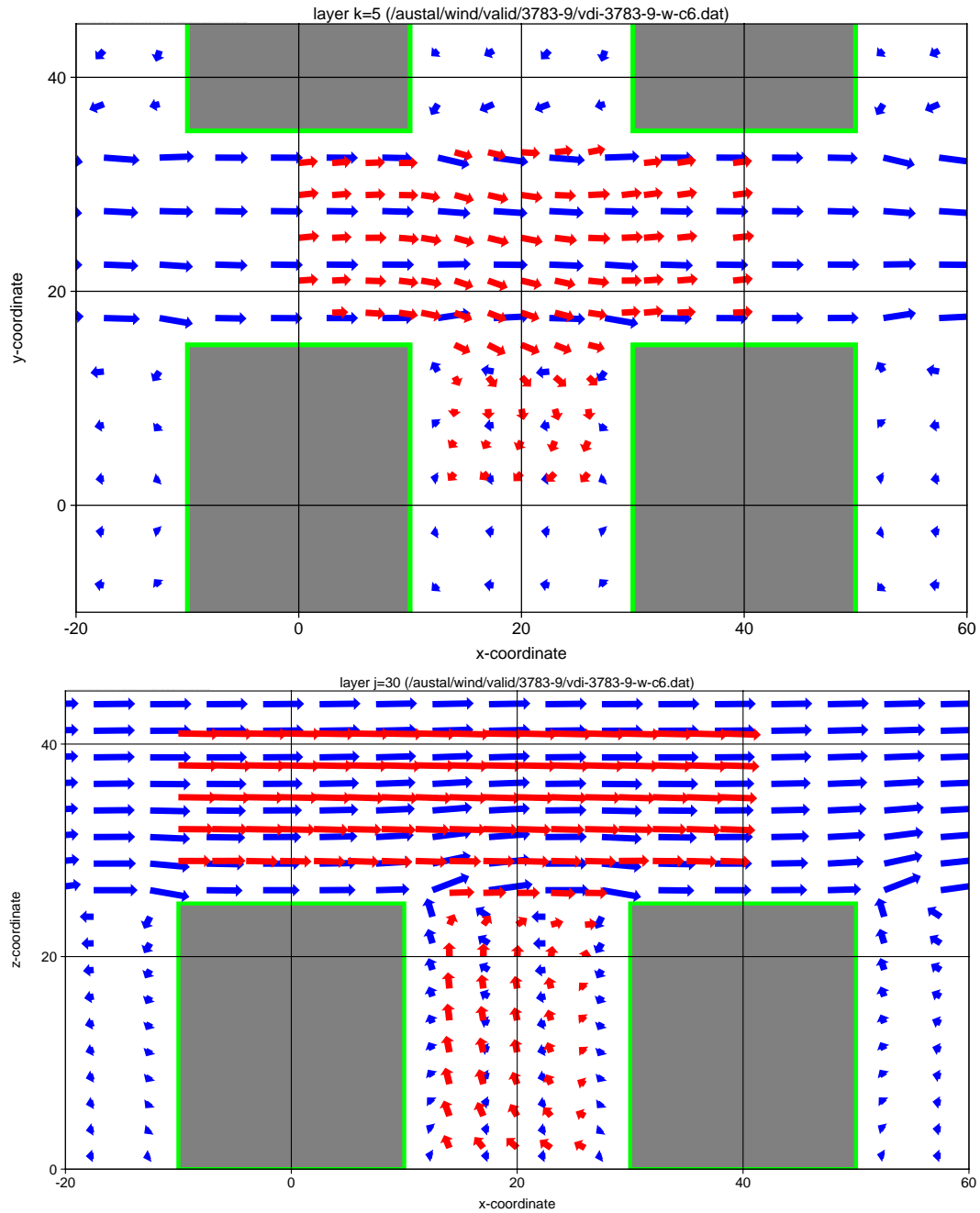


FIGURE 16: Guideline draft VDI 3783 part 9, data set c6, set of 3 times 7 cuboids in a cross flow. Top: Horizontal cut at $z = 12.5$ m. Bottom: Vertical cut at $y = 0$ m.

4.2.2 U-shaped building

At the wind tunnel facility of the University of Karlsruhe (*Institut für Hydrologie und Wasserwirtschaft*), the wind field for an U-shaped building in a cross flow was measured for two different building heights (PEF, 1992). The heights were 28 m and 40 m, the length of the base side 54 m, the length of the outer side walls 40 m, and the building width 12 m ($\Delta z = 3$ m, $\Delta x = 3$ m, $u_A = 5$ m/s, $h_A = 10$ m, $z_0 = 0.4$ m, $d_0 = 0$ m).

The graphical comparisons in Fig. 17 left part, Fig. 18 left part, Fig. 19 left part, and Fig. 20 shows that the observed deceleration of the flow in front of the building and the magnitude of the recirculation in its lee from ground to half a building height are reproduced by the model, the extend of the recirculation zone in flow direction is slightly too short. In the upper half of the building wake, the calculated recirculation ends at a distance of about one building height from the back-side wall, whereas in the experiment it is preserved up to the building height for much larger distances. This difference is probably due to the fact that for the model fields the two side walls of the building have only little influence on the construction of the recirculation field \mathbf{R} inside the patio of the building. Just above the building, both observed and calculated wind field show again good agreement, see Fig. 17 right part, Fig. 18, Fig. 19 right part, and Fig. 20.

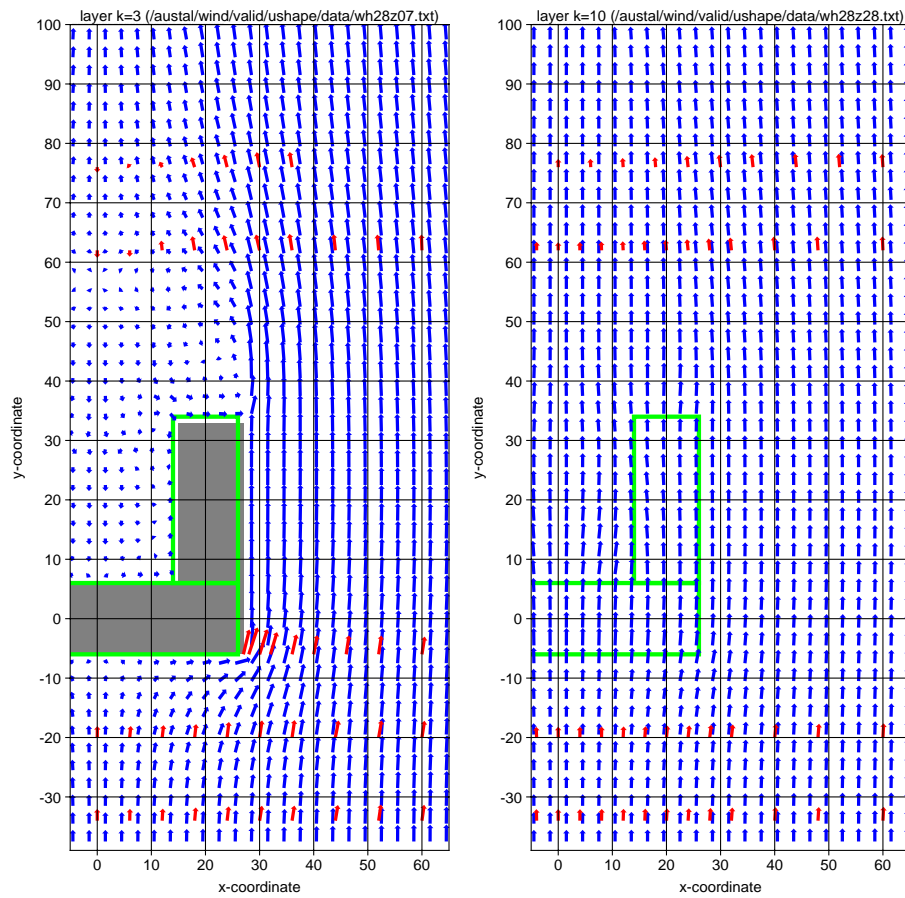


FIGURE 17: U-shaped building ($H = 28$ m). Left: Horizontal cut at $z = 7$ m ($\tau = 0.5$ s). Right: Horizontal cut at $z = 28$ m ($\tau = 0.25$ s).

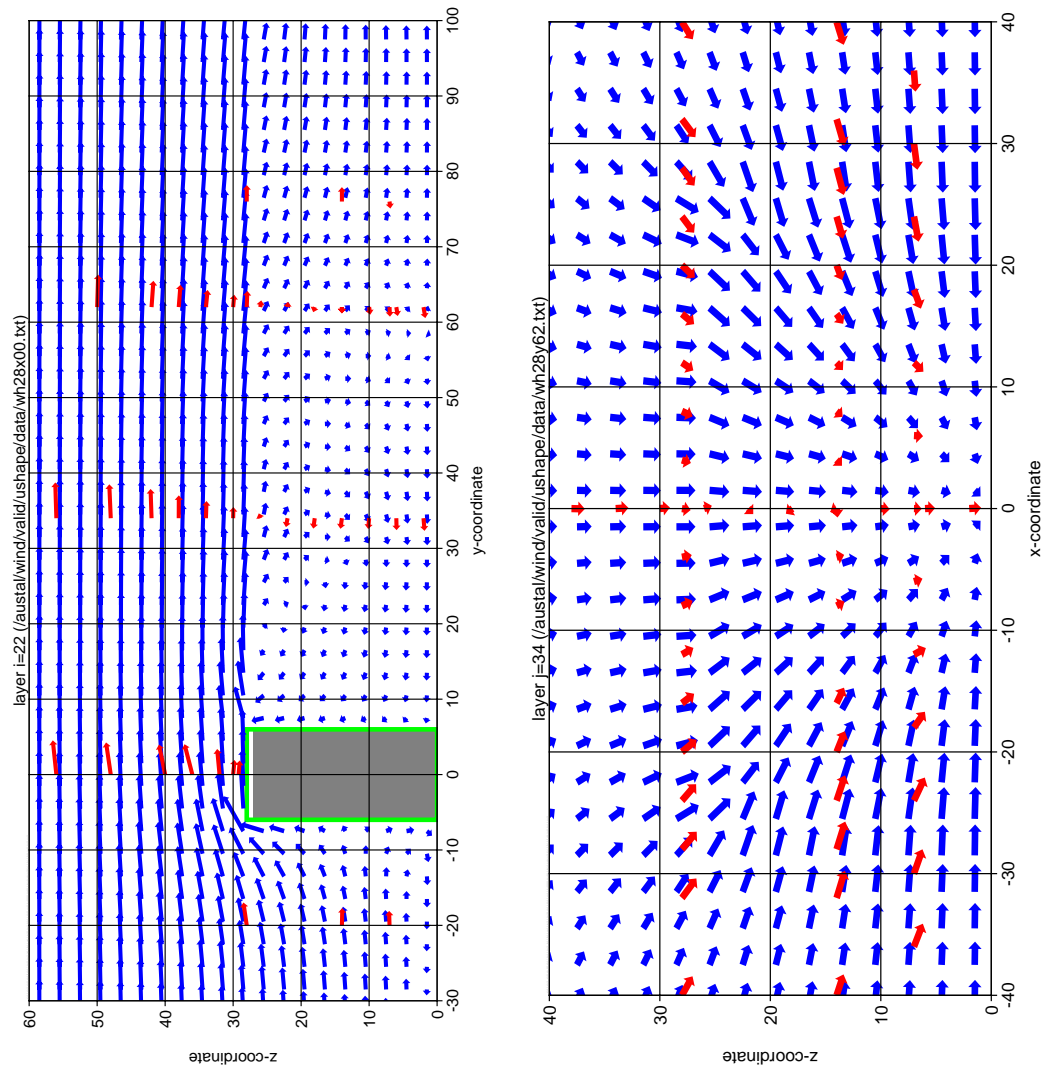


FIGURE 18: U-shaped building ($H = 28$ m). Left: Vertical cut at $x = 0$ m ($\tau = 0.5$ s). Right: Vertical cut at $y = 62$ m ($\tau = 1.5$ s).

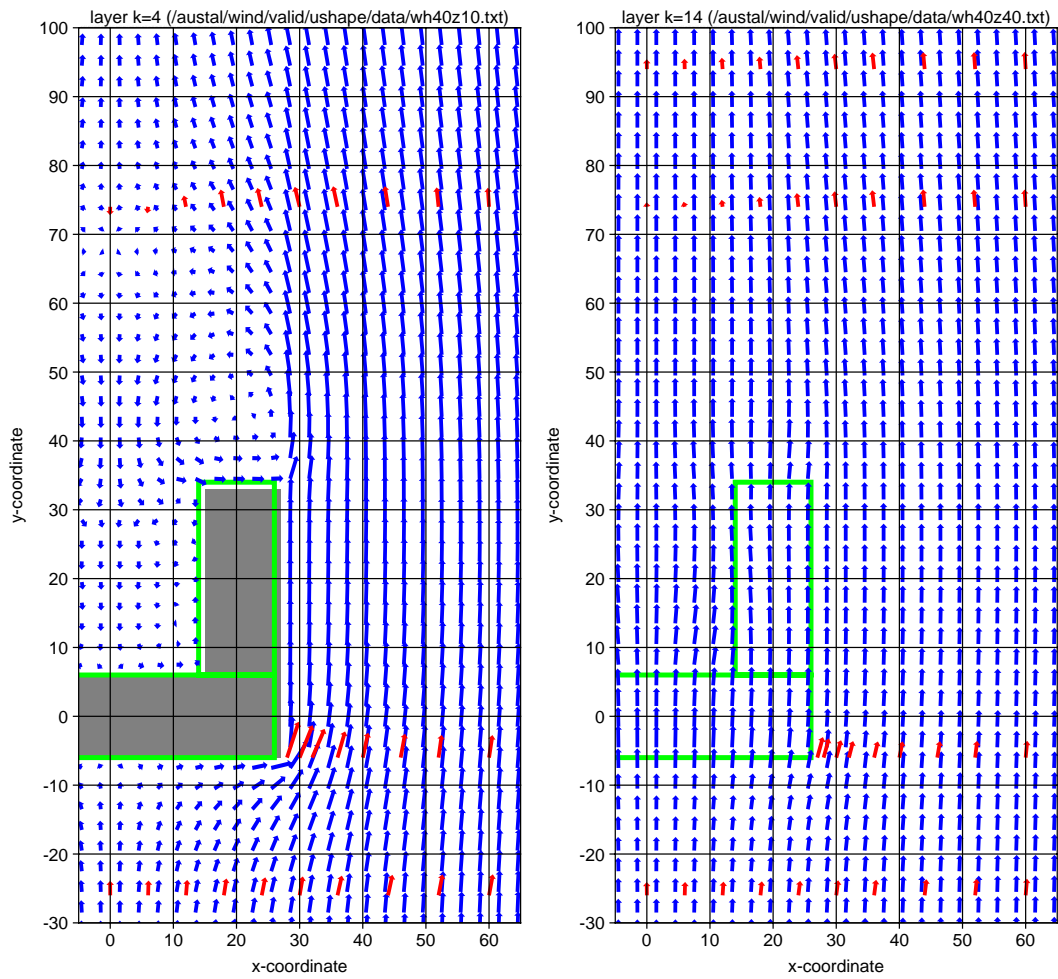


FIGURE 19: U-shaped building ($H = 40$ m). Left: Horizontal cut at $z = 10$ m ($\tau = 0.5$ s). Right: Horizontal cut at $z = 40$ m ($\tau = 0.25$ s).

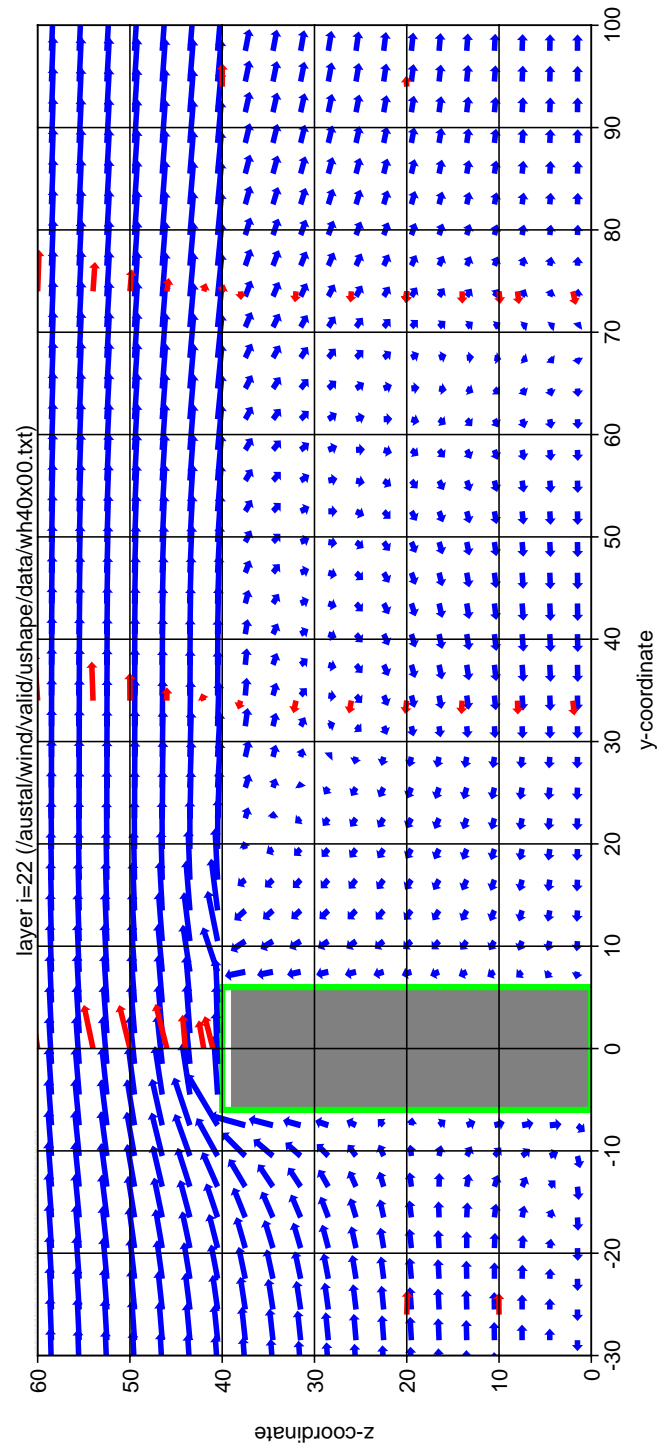


FIGURE 20: U-shaped building ($H = 40$ m, Vertical cut at $x = 0$ m, $\tau = 0.5$ s).

4.2.3 Street crossing

At the wind tunnel facility of the University of Karlsruhe (*Institut für Hydrologie und Wasserwirtschaft*), the wind field at a street crossing formed by four ring-like building complexes was measured for different directions of the incoming flow (PEF, 1994).

The height of the buildings was 18 m, the length of the outer walls 90 m, and both building width and street width 18 m ($\Delta z = 3$ m, $\Delta x = 4.5$ m, $u_A = 5$ m/s, $h_A = 10$ m, $z_0 = 0.1$ m, $d_0 = 0$ m).

For an westward incoming flow along the street canyon ($r = 270$ deg), both observation and calculation show a nearly undisturbed flow at the crossing, see Fig. 21 and Fig. 22. From Fig. 22 it can be seen that the measured backward flow in the side canyon, unlike the calculated one, disappears already at a height of $z = 15$ m, well below the upper edge of the building. This is in some contrast to the observations for case c6 of the guideline draft VDI 3783 part 9, where the backward flow in the side canyon (Fig. reffig:vdi-c6, bottom) extends up to the upper edge of the building, similar to the other test cases with single buildings.

For non-perpendicular flow directions from southwest ($r = 225$ deg, Fig. 23 and Fig. 24) and west-southwest ($r = 240$ deg, , Fig. 25 and Fig. 26), the calculated flow at the crossing is decelerated too strongly near ground.

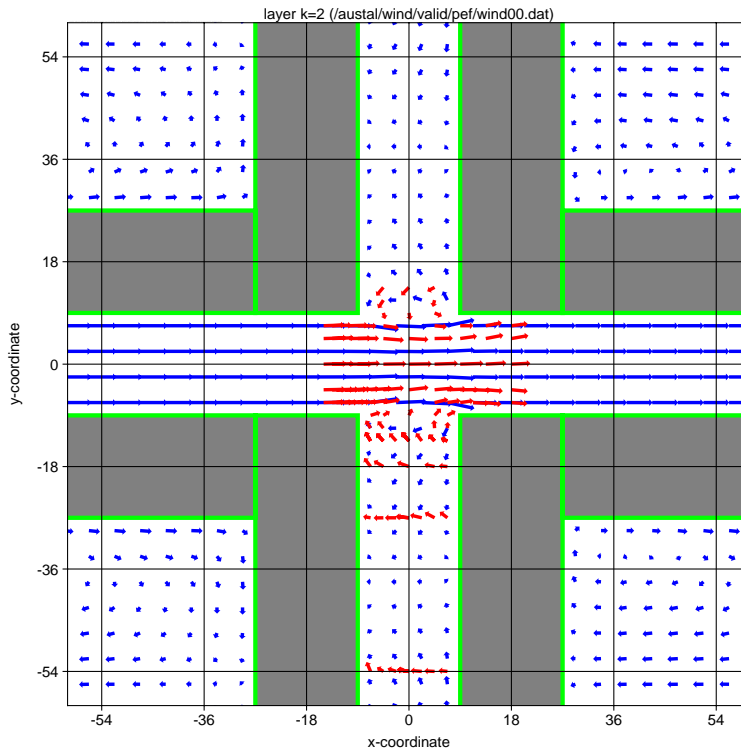


FIGURE 21: Street crossing (incoming flow direction $r = 270$ deg, horizontal cut at $z = 4.5$ m, $\tau = 1$ s).

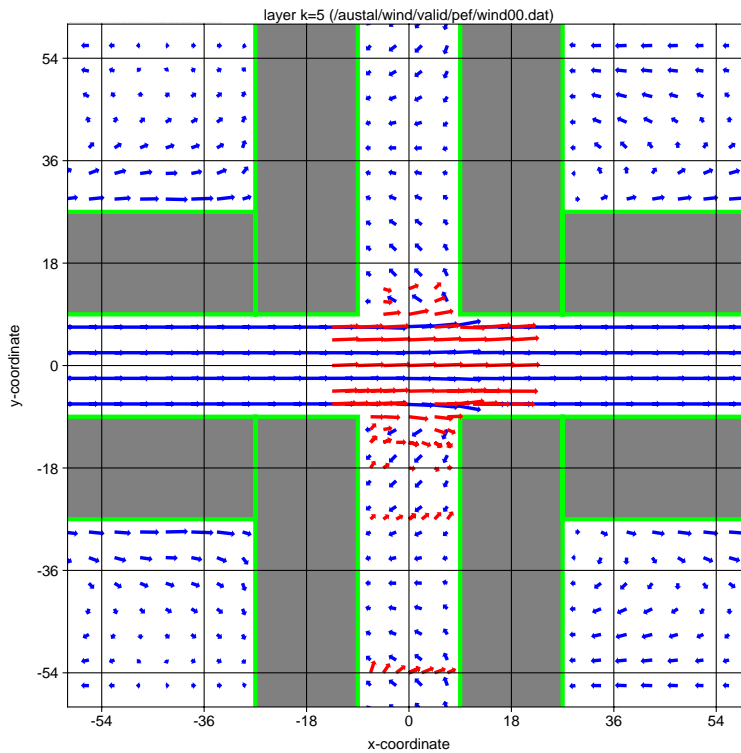


FIGURE 22: Street crossing (incoming flow direction $r = 270$ deg, horizontal cut at $z = 15$ m, $\tau = 1$ s).

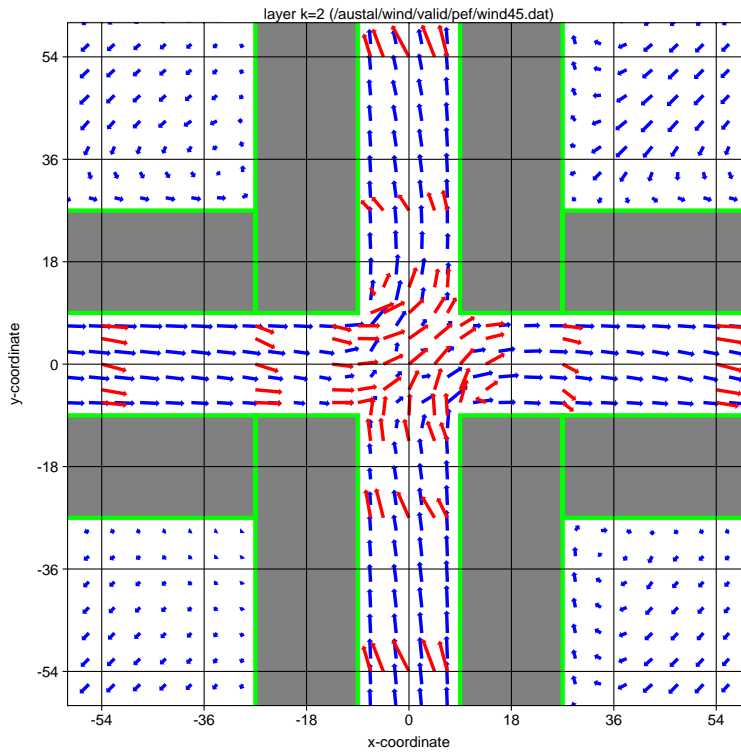


FIGURE 23: Street crossing (incoming flow direction $r = 225$ deg, horizontal cut at $z = 4.5$ m, $\tau = 1$ s).

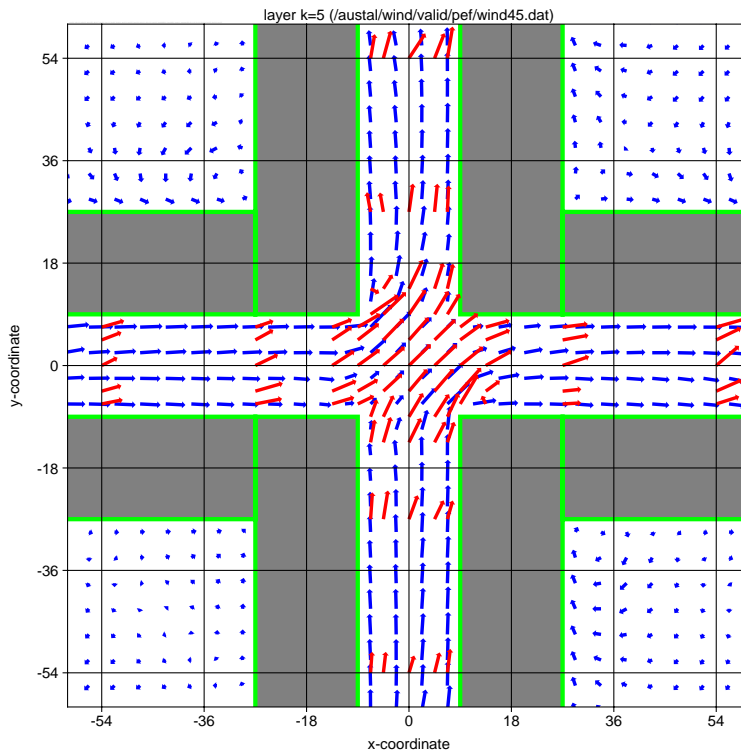


FIGURE 24: Street crossing (incoming flow direction $r = 225$ deg, horizontal cut at $z = 15$ m, $\tau = 1$ s).

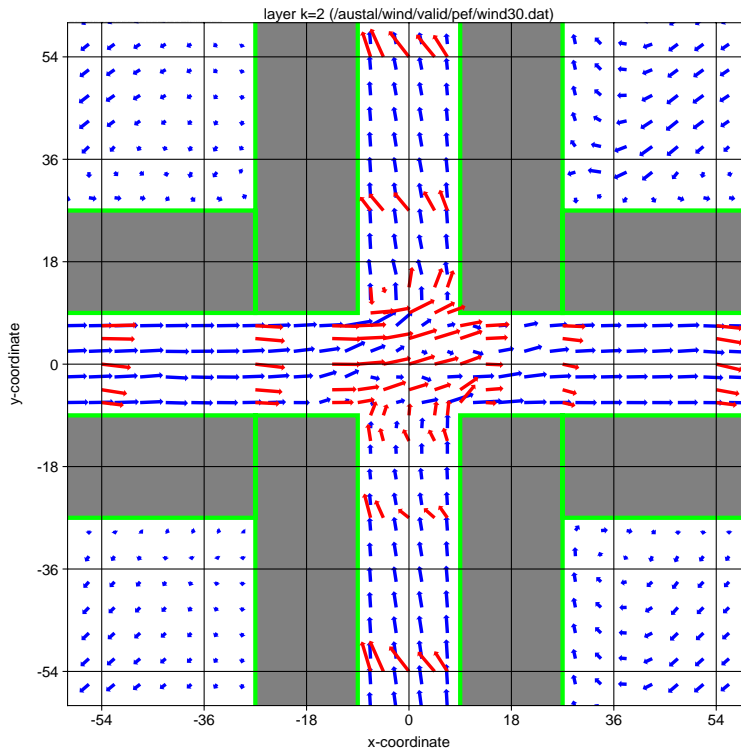


FIGURE 25: Street crossing (incoming flow direction $r = 240$ deg, horizontal cut at $z = 4.5$ m, $\tau = 1$ s).

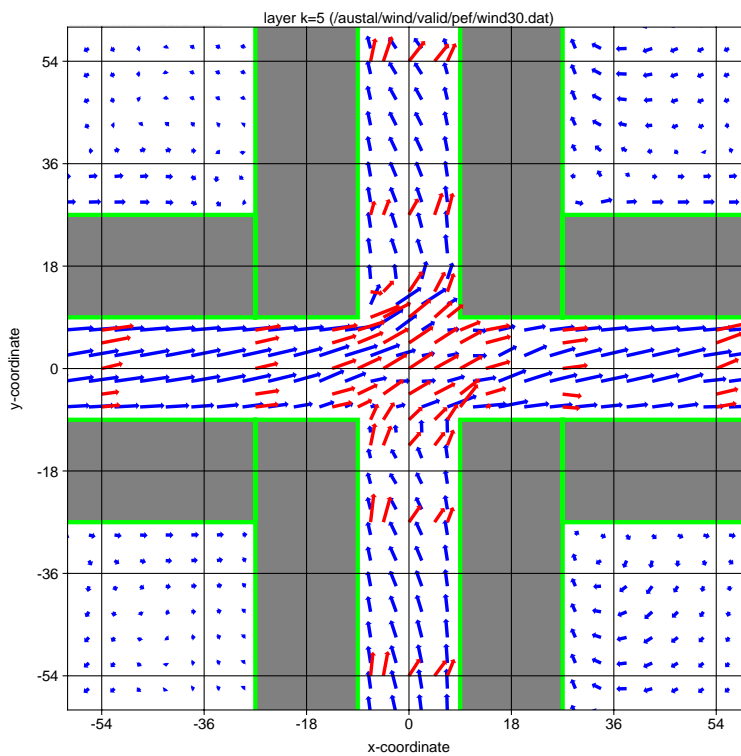


FIGURE 26: Street crossing (incoming flow direction $r = 240$ deg, horizontal cut at $z = 15$ m, $\tau = 1$ s).

4.2.4 Measurements at the streets *Bonnerstrasse* and *Venloerstrasse*

Guideline VDI 3783 part 10 contains data sets from wind field measurements carried out by the Technical Inspection Agency (TÜV) Rheinland. At four measurement positions in the streets *Bonnerstrasse* and *Venloerstrasse*, respectively, the Cartesian components of the wind vector were measured for different wind directions (positions 1 and 3 close to the upper edges of the street canyon, positions 2 and 4 at 4 m above ground at the street sides). For comparisons with model calculations, the measured wind vectors had been scaled with the measured wind speed at a given reference point.

The guideline quotes a roughness length of $z_0 = 0.4$ m and a displacement height of $d_0 = 9.8$ m for the *Bonnerstrasse* and $z_0 = 0.5$ m, $d_0 = 7.9$ m for the *Venloerstrasse* to be used for the theoretical wind profile of the incoming flow. However, these values seemed too large if the buildings are accounted for explicitly, therefore for both cases $z_0 = 0.2$ m and $d_0 = 1.2$ m were applied instead in the model calculations.

The calculations were carried out for a wind rose in steps of 10 deg. Fig. 27 shows the comparison of calculated and measured scaled wind components. Symbols denote measured values and lines calculated ones. The horizontal wind component in direction of the street canyon (v) is shown in blue colour, the horizontal component perpendicular to the canyon (u) in red colour, and the vertical component (w) in green colour. The arrangement of the four diagrams in each figure corresponds to the positions of the measurement points across the street canyon.

The measured horizontal wind component parallel to the street canyon (blue) is reproduced quite well by the model. Both in the measurements and in the model the flow proceeds more or less undisturbed along the street canyon. The measured vertical profile is well reproduced by the utilized values for z_0 and d_0 .

Perpendicular to the street canyon (red) and in the vertical (green), the wind speed near ground (points 2 and 4) is underestimated by the model, the general dependency on wind direction is reproduced. Near the upper edge of the canyon (points 1 and 3), the calculated range of wind speeds is about the same as in the observations, but the change with wind direction is only poorly reproduced. Details like the actual roof shapes that are not accounted for in the calculations may play an important role in this region, where the transition of the backwards directed flow to the incident flow direction occurs.

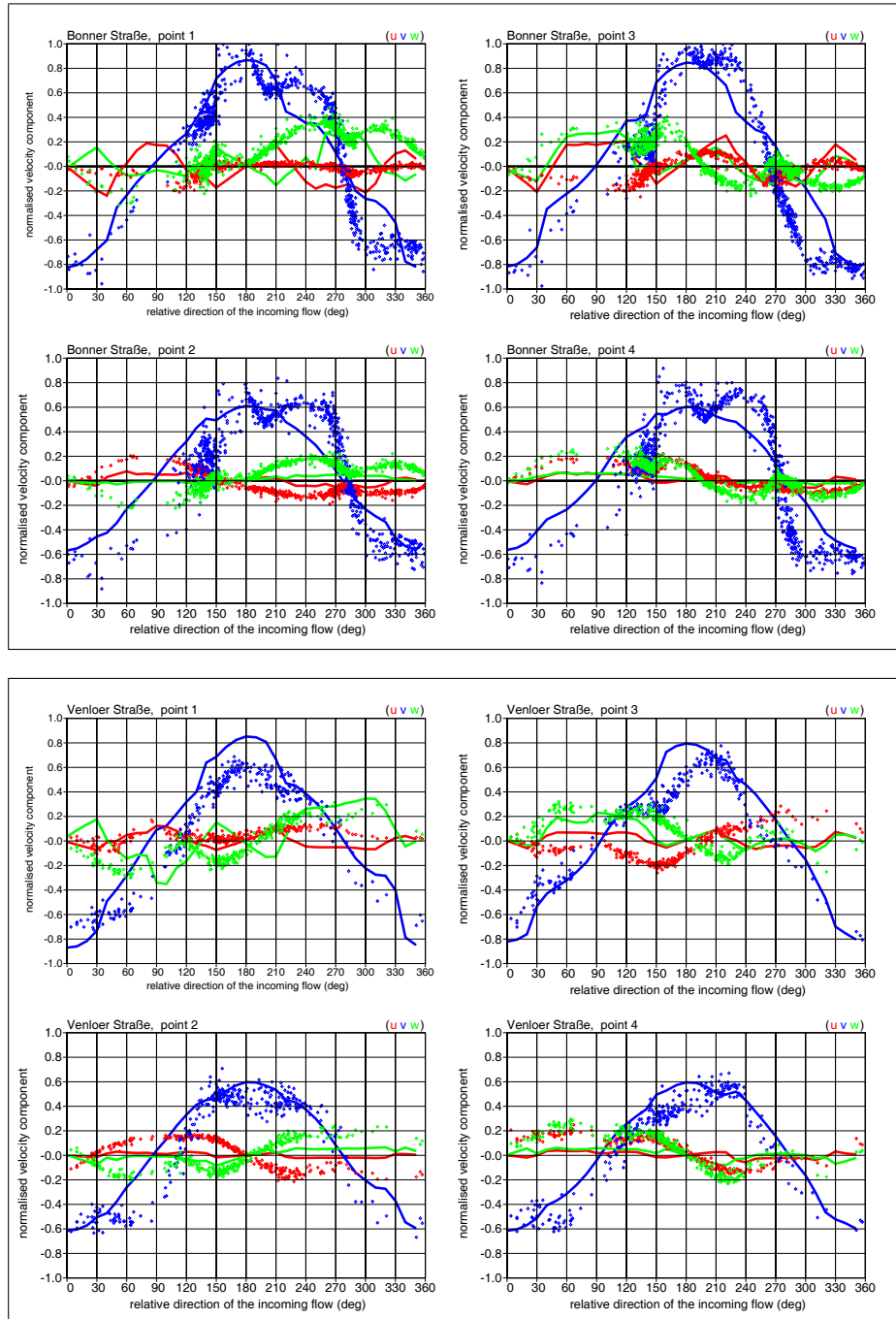


FIGURE 27: Measurements in the streets *Bonnerstrasse* (top) and *Venloerstrasse* (bottom). The diagrams show the normalized measured (symbols) and calculated (lines) wind components parallel to the street canyon (v , blue), across (u , red), and vertically (w , green) for 4 measurement positions and different directions of the incoming flow, respectively ($z_0 = 0.2$ m, $d_0 = 1.2$ m, $\Delta x = 3$ m, $\Delta z = 3$ m). The arrangement of the four diagrams corresponds to the positions of the measurement points across the street canyon.

4.3 Validation of the velocity fluctuations

An obstacle not only influences the mean wind field but as well the velocity fluctuations and diffusion properties of the flow, in particular in its wake. The obstacle-induced additional turbulence can be accounted for in a Lagrangian particle model by means of additional meteorological fields.¹¹ In the present model approach, these additional fields are derived on the basis of the recirculation field, see section 3.3.

The additional field of velocity fluctuations can be compared with measurements. In contrast, the additional field of diffusion coefficients can be validated only indirectly by means of the resulting concentration distribution, see section 4.4.

The following tests check the extend and magnitude of the field of additional velocity fluctuations. The simple model approach being used does not allow to reproduce spatial details of the real field, but this should not be required for the considered application range of source heights above 1.2 times the building height.

4.3.1 CEDVAL data sets A1-1, A1-4, A1-6

The CEDVAL data sets (CEDVAL, 2004) produced at the wind tunnel of the Meteorological Institute of the University of Hamburg contain measurements of the turbulence intensity for the undisturbed flow and the disturbed flow in the presence of a building. In particular near ground the measured data contain a relatively large statistical uncertainty, the range of reported values for a specific location varying up to a factor of 2 in some data sets.

Figs. 28 to 33 depict the fluctuations for the data sets A1-1, A1-4, and A1-6. Shown is the excess fluctuation with respect to the undisturbed flow for the Cartesian components u (parallel to the incoming flow direction), v (horizontal and perpendicular to u), and w (vertical) for different heights (specified in units of the building height $H = 25$ m). The corresponding modelled (isotropic) excess velocity fluctuations are shown below each plot.

The general extend and magnitude of the modelled fluctuations agrees roughly with the measured ones, detailed structures are not reproduced.¹²

¹¹I some areas near the boundary faces the turbulence may be as well reduced, an effect which is not considered further in this context.

¹²The modelled fluctuations are not reduced to zero at h_s times building height (as they should be according to their mathematical construction) because they are calculated first on the centre points of the grid cells and then interpolated to the knot points of the calculation grid.

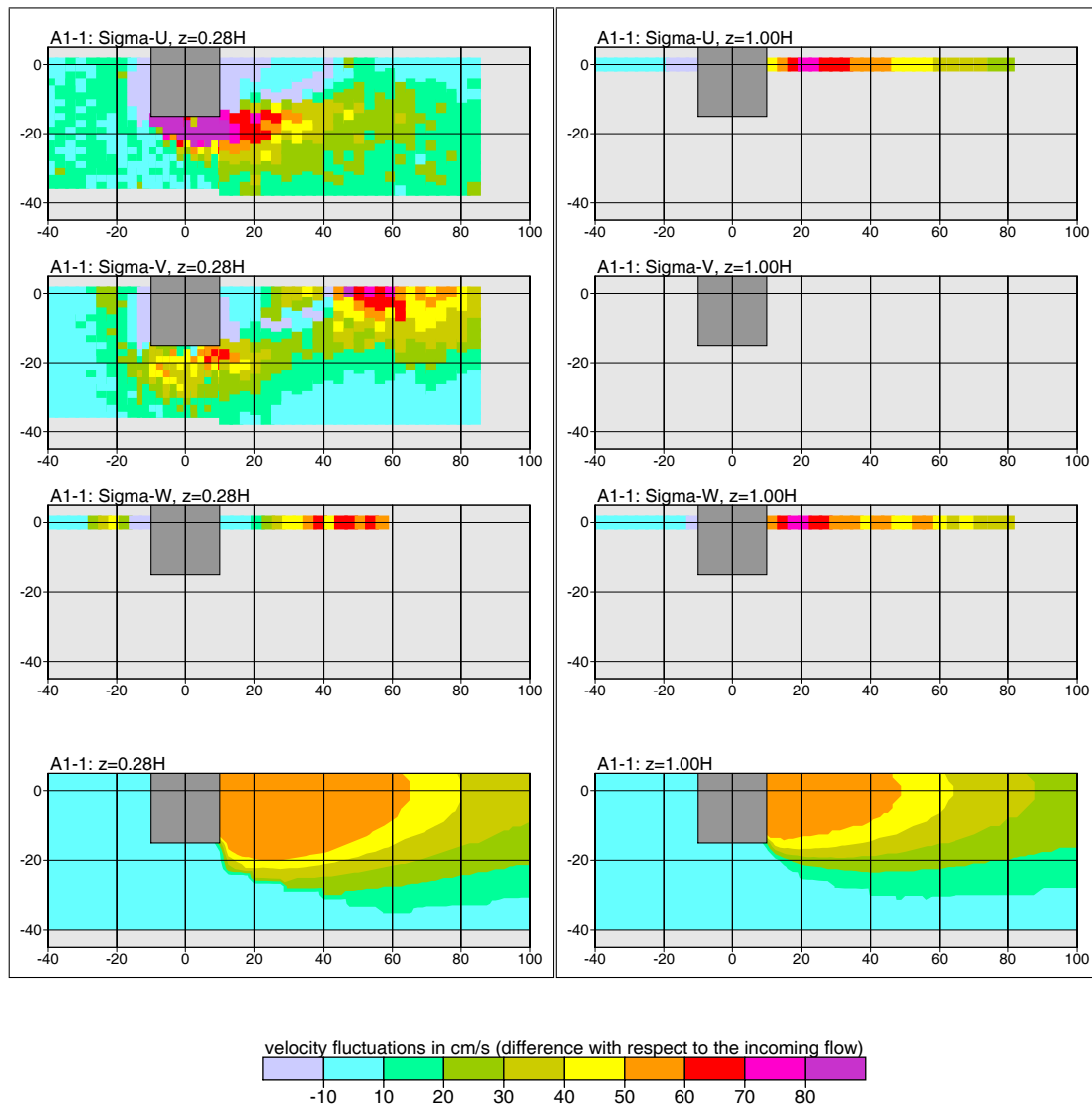


FIGURE 28: Data set A1-1, difference of velocity fluctuations with respect to the undisturbed flow. In each column, the upper three graphs depict the measured values and the lower one the model result.

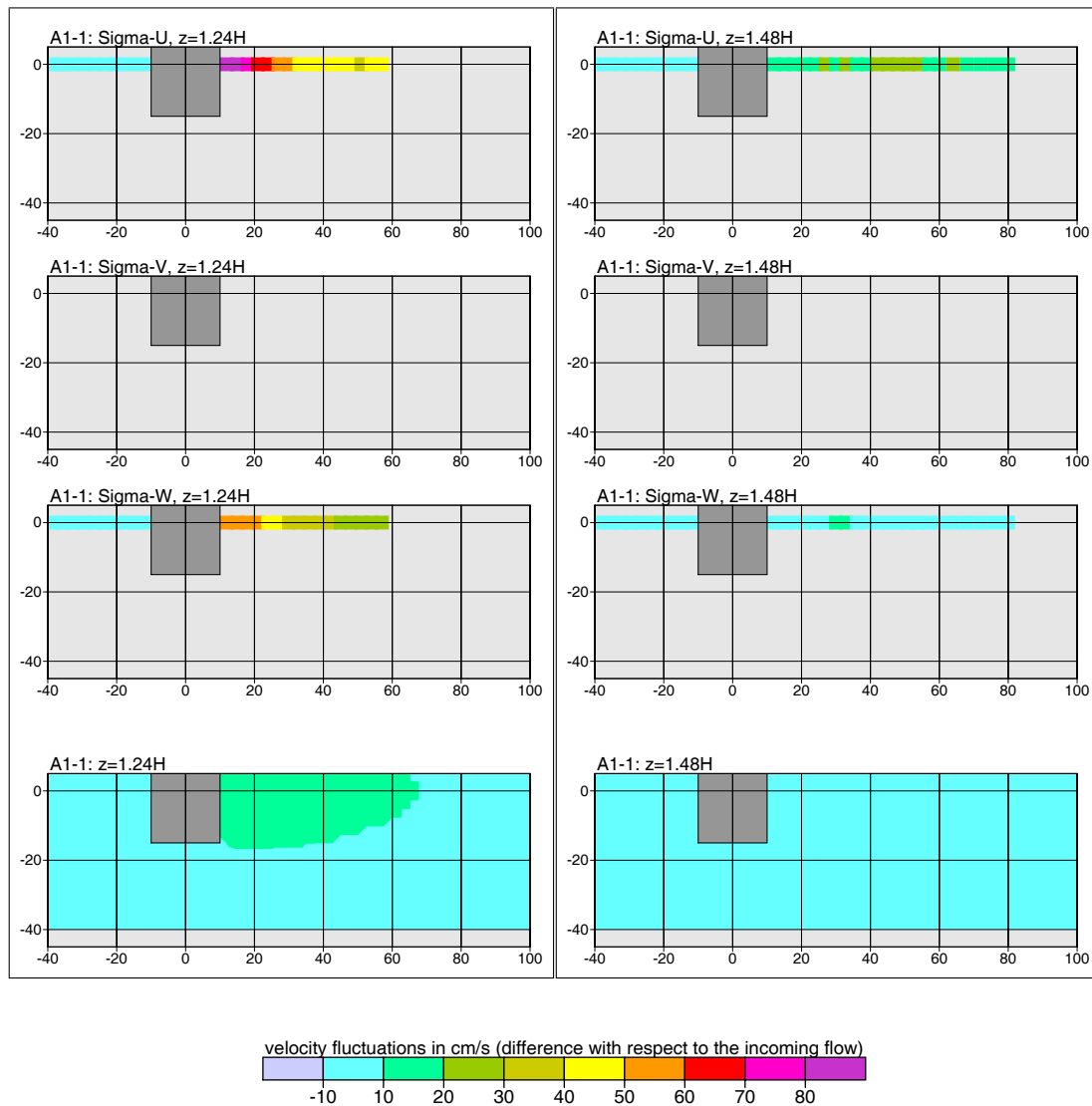


FIGURE 29: Data set A1-1, difference of velocity fluctuations with respect to the undisturbed flow. In each column, the upper three graphs depict the measured values and the lower one the model result.

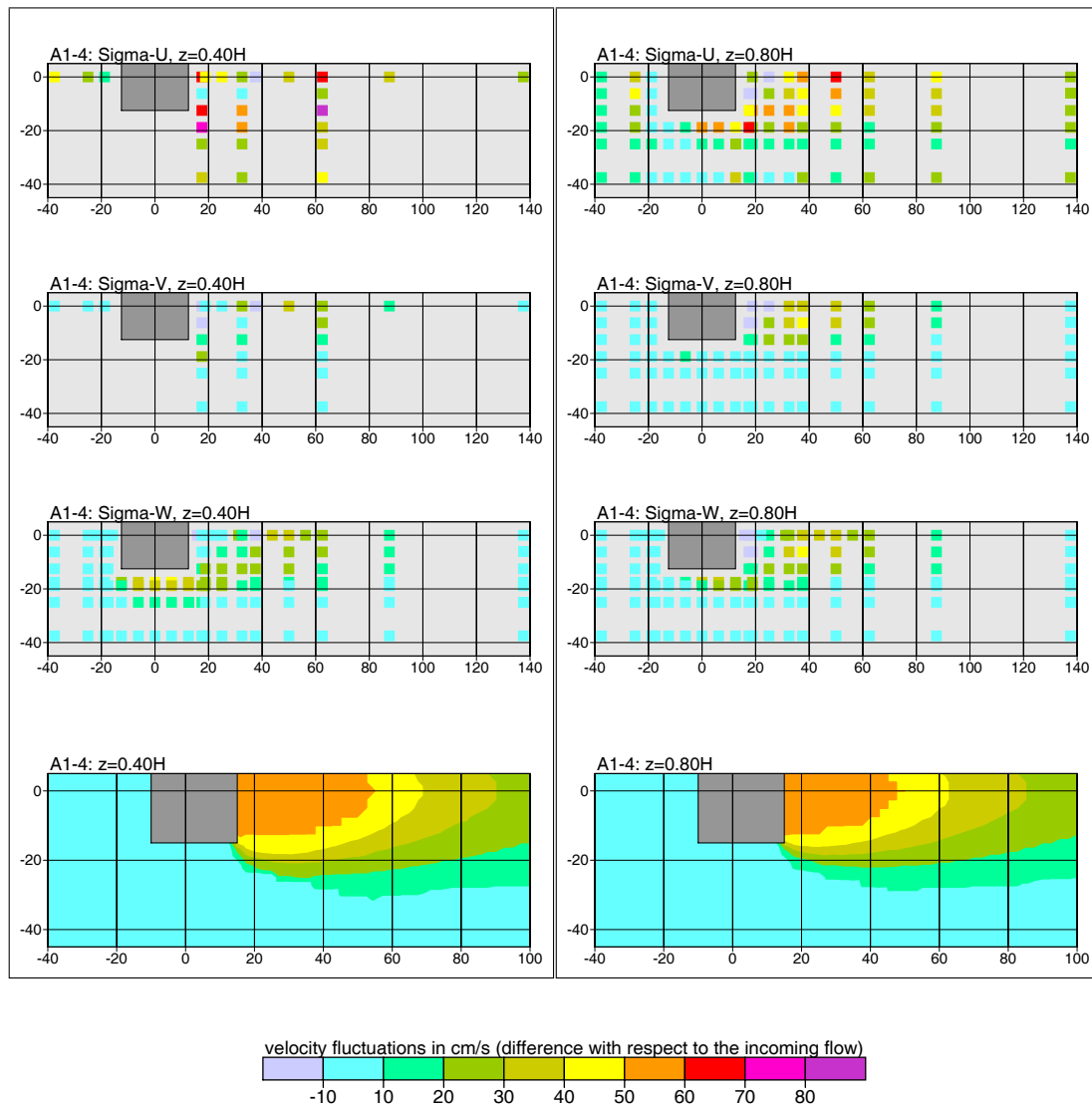


FIGURE 30: Data set A1-4, difference of velocity fluctuations with respect to the undisturbed flow. In each column, the upper three graphs depict the measured values and the lower one the model result.

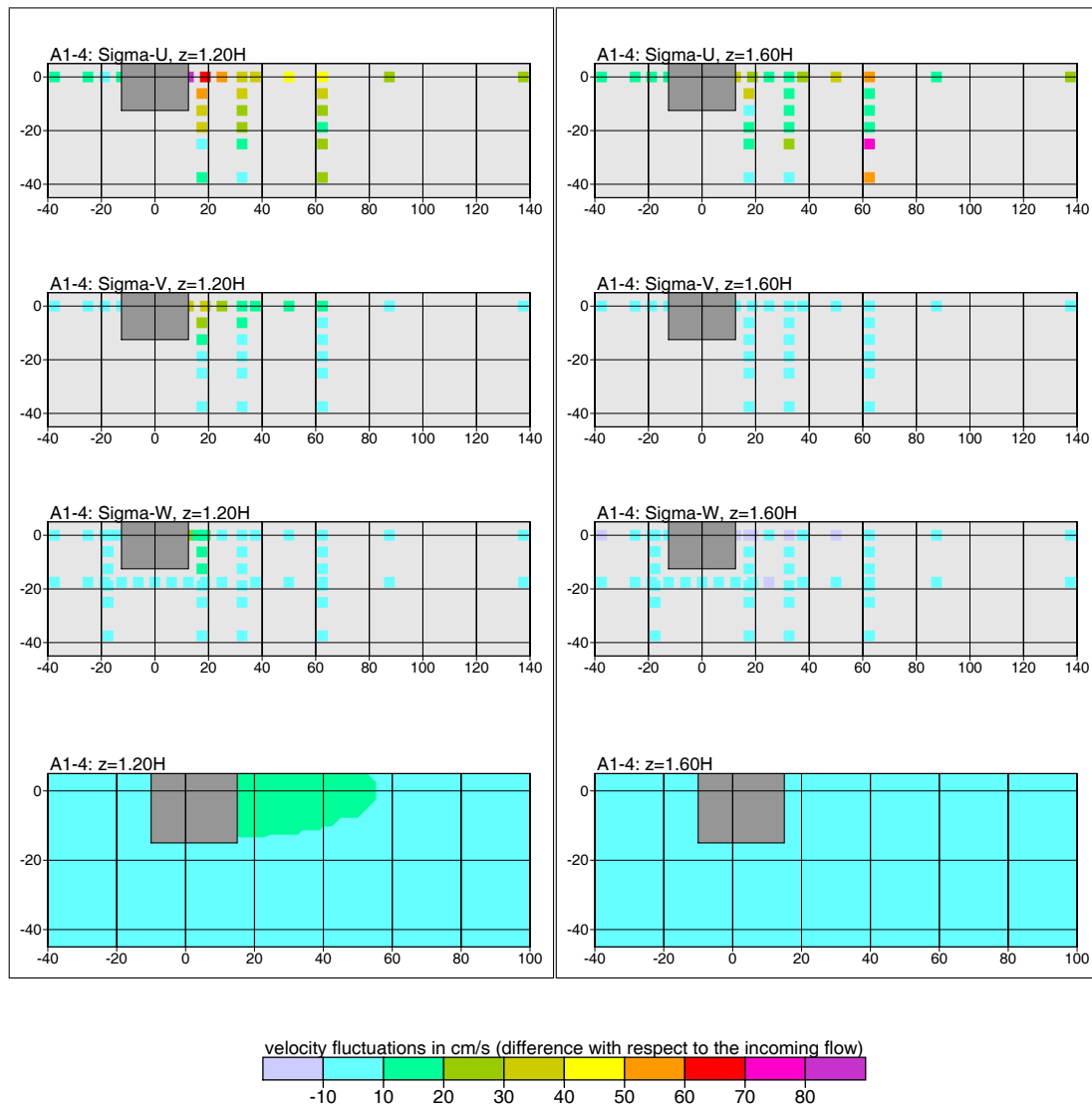


FIGURE 31: Data set A1-4, difference of velocity fluctuations with respect to the undisturbed flow. In each column, the upper three graphs depict the measured values and the lower one the model result.

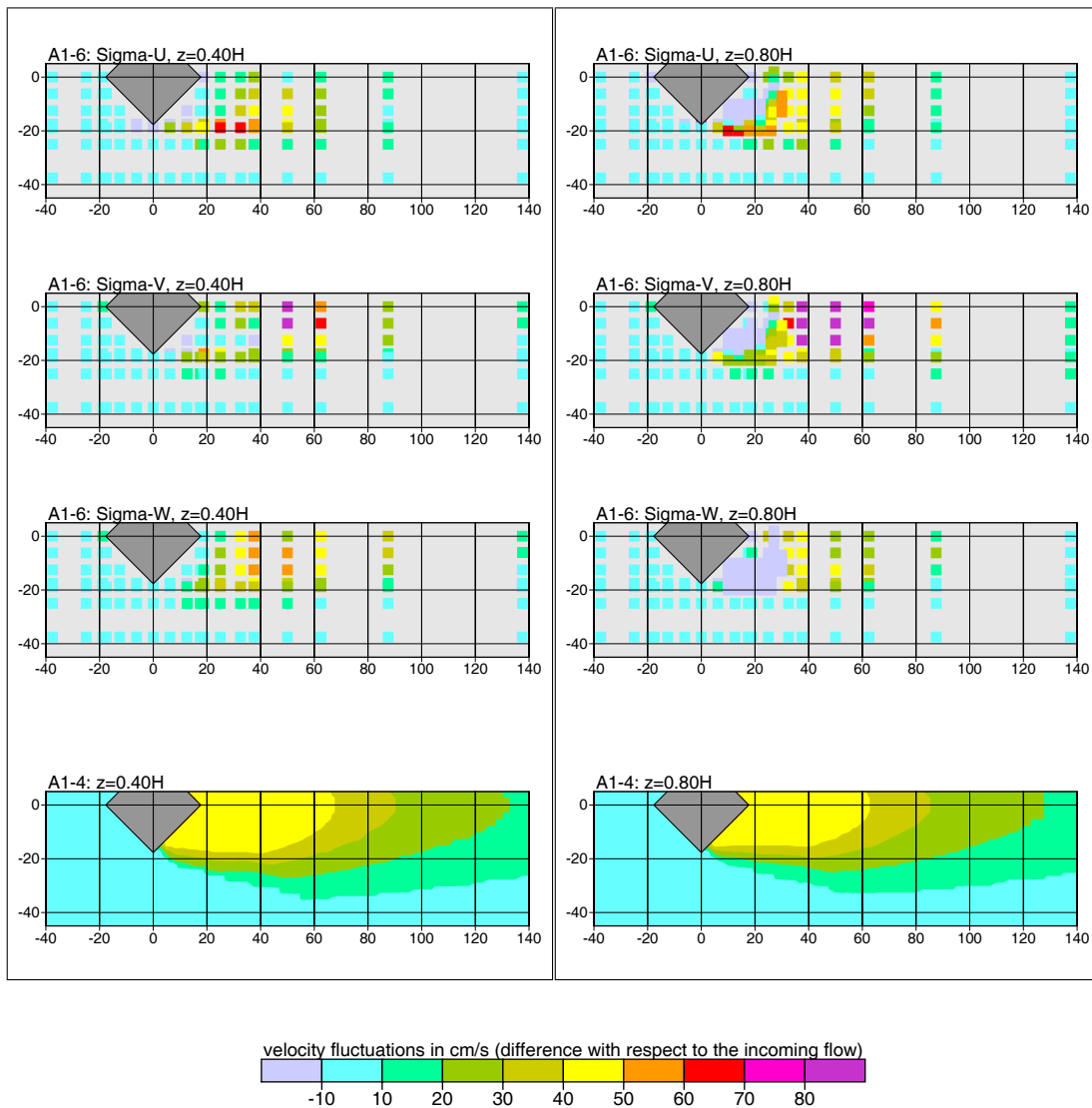


FIGURE 32: Data set A1-6, difference of velocity fluctuations with respect to the undisturbed flow. In each column, the upper three graphs depict the measured values and the lower one the model result.

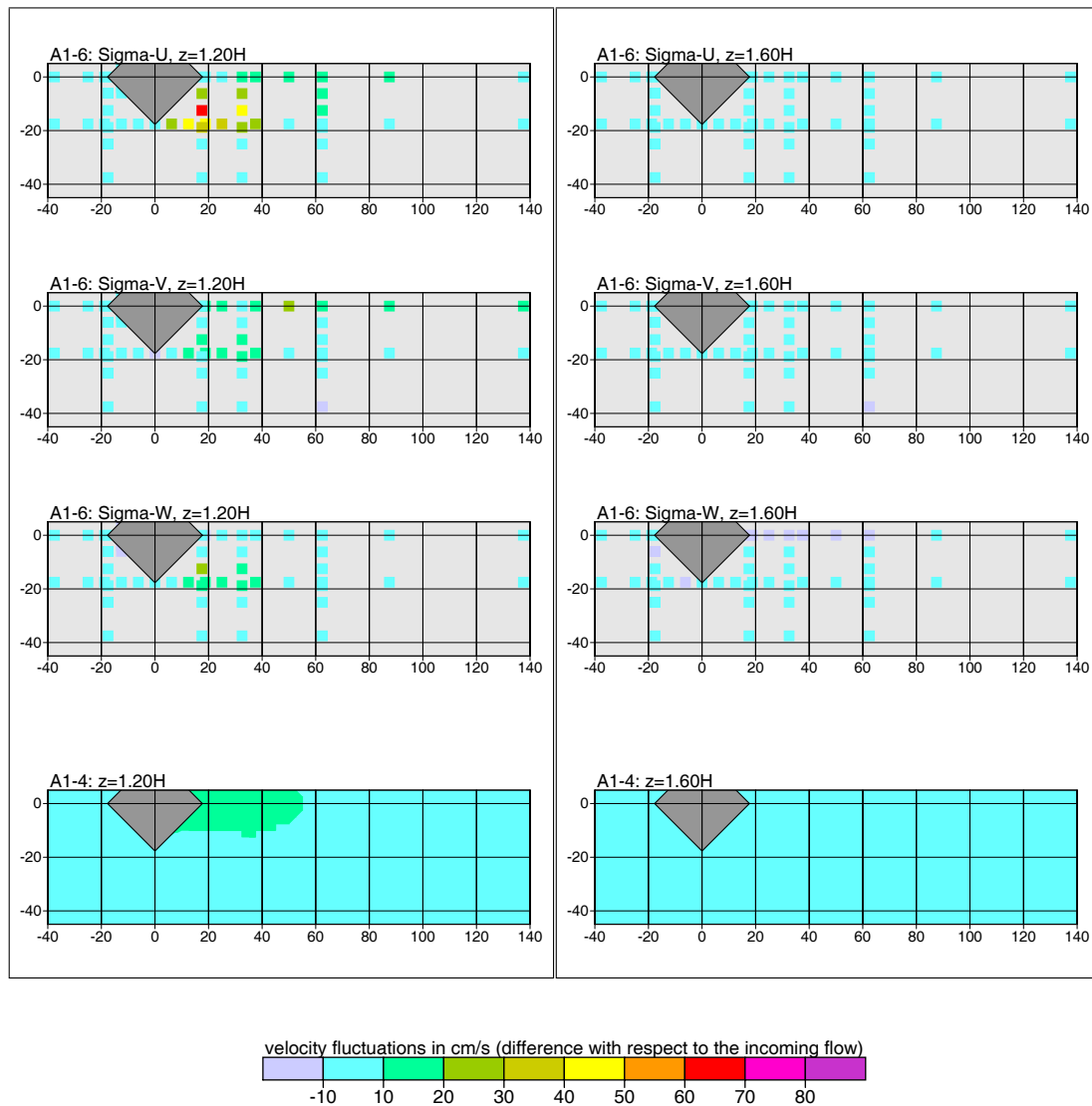


FIGURE 33: Data set A1-6, difference of velocity fluctuations with respect to the undisturbed flow. In each column, the upper three graphs depict the measured values and the lower one the model result.

4.3.2 Cooling tower

In a project that investigated the influence of a cooling tower at a nuclear power station in the district Emsland (SCHATZMANN & LOHMEYER, 1991), wind and concentration measurements were carried out in a wind tunnel for a cooling tower (height 152 m, diameter 80 m) and a 160 m stack located about 340 m apart from the tower. Among other, the velocity fluctuations with and without cooling tower were measured.

Table 1 lists the measured fluctuation changes due to the presence of the cooling tower. The incident wind speed is 23 m/s at 80 m height.¹³ The fluctuations are listed for several stack distances x (distance from the cooling tower $\hat{x} = x - 340$ m), distances y from the centre axis of the perturbed flow (-200 m, -100 m, 0 m, 100 m, 200 m), and heights z above ground.

Fig. 34 shows the result of corresponding model calculations for the heights 40 m and 120 m (at 200 m the modelled fluctuations are fallen of to zero). The comparison with the measured distributions is difficult in view of the strong variations of the measured data, but extend and magnitude of the fluctuation seem to be of similar order. Close to the tower ($\hat{x} = 160$ m) the calculated values are systematically higher than the measured ones.

¹³Numbers were deduced from the values given in report JANICKE (1992) for a flow direction of 120 deg.

TABLE 1: Wind tunnel measurements for a cooling tower. Change of velocity fluctuations due to the cooling tower in cm/s for different distances from the tower, distances from the centre line of the disturbed flow (-200 m to 200 m), and heights above ground (z).

$x = 500 \text{ m}, \hat{x} = 160 \text{ m}$															
$z \text{ (m)}$	$\Delta\sigma_u$					$\Delta\sigma_v$					$\Delta\sigma_w$				
	-200	-100	0	100	200	-200	-100	0	100	200	-200	-100	0	100	200
400	-30	6	6	8	18	15	8	6	8	-5	5	13	3	11	6
200	19	10	28	17	2	13	-2	21	27	26	13	3	8	24	3
120	-14	17	175	100	25	2	17	259	30	7	2	20	171	70	6
80	19	86	148	102	10	12	8	121	73	29	5	30	72	81	23
40	24	65	121	136	33	11	15	84	43	-6	25	75	87	96	21
$x = 1000 \text{ m}, \hat{x} = 660 \text{ m}$															
$z \text{ (m)}$	$\Delta\sigma_u$					$\Delta\sigma_v$					$\Delta\sigma_w$				
	-200	-100	0	100	200	-200	-100	0	100	200	-200	-100	0	100	200
400	2	11	5	-2	-11	-18	9	-2	4	7	-6	1	4	6	0
200	12	-6	20	27	12	-5	17	39	20	-6	-10	23	4	13	14
120	-10	97	19	28	19	-17	36	77	51	9	-13	45	77	62	13
80	56	68	19	-4	19	-1	37	70	53	11	6	59	85	59	16
40	25	10	-1	-49	-6	16	19	28	7	14	-2	19	33	2	22
$x = 1500 \text{ m}, \hat{x} = 1160 \text{ m}$															
$z \text{ (m)}$	$\Delta\sigma_u$					$\Delta\sigma_v$					$\Delta\sigma_w$				
	-200	-100	0	100	200	-200	-100	0	100	200	-200	-100	0	100	200
400	33	11	0	24	23	16	5	8	11	9	15	9	-1	7	14
200	25	21	15	58	27	10	12	58	56	26	17	18	26	30	26
120	96	29	4	20	39	13	34	50	75	33	22	37	54	58	22
80	65	-11	-7	-53	52	24	56	31	42	16	26	40	33	31	38
40	35	-3	14	-21	9	23	28	27	2	7	11	17	19	7	10

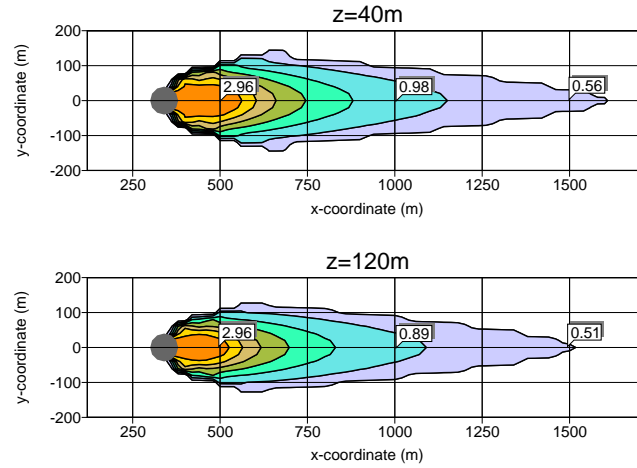


FIGURE 34: Wind tunnel measurements for the cooling tower. Calculated increase of velocity fluctuations due to the cooling tower for the horizontal cuts 40 m and 120 m. The position of the tower is marked as gray circle ($z_0 = 1.5 \text{ m}$, $d_0 = 9 \text{ m}$, $u_A = 23 \text{ m/s}$, $h_A = 80 \text{ m}$, $\Delta x = 20 \text{ m}$, $\Delta z = 10 \text{ m}$).

4.4 Validation of the concentration distributions

4.4.1 U-shaped building

Concentration measurements were carried out for the U-shaped building (see section 4.2.2) for different directions of the incoming flow r_a and building heights H . The source was situated at three different positions:

Position	x (m)	y (m)	z
A (on top of the building)	0	0	$H + 2$ m
B (in the patio)	20	0	2 m
C (at the front side)	-20	0	2 m

The following experimental scenarios were re-calculated with the model ($u_A = 5$ m/s, $h_A = 10$ m, $z_0 = 0.2$ m, $d_0 = 1.2$ m, $\Delta x = 4$ m, $\Delta z = 3$ m, emission strength $Q = 5$ g/s):

Building height H (m)	Flow direction r (deg)	Data set (position A)
28	180	ch28qaw000
28	225	ch28qaw045
28	270	ch28qaw090
28	300	ch28qaw120
28	315	ch28qaw135
16	225	ch28qaw045
16	0	ch28qaw180
40	180	ch28qaw000
40	225	ch28qaw045
40	0	ch28qaw180

Figs. 35 to 40 show both the normalized concentrations $C = cu_A/Q$ near ground of the measurements (coloured squares) and the calculated ones (background).

Overall, the comparison reveals no principle differences in the measured and modelled concentration distributions, on average the concentrations are slightly overestimated by the model. An exception is formed by the top source A and an incident flow direction of 225 deg; here, the measured plume touches ground already inside the patio whereas the modelled one reaches ground only at larger distances and with a higher dilution. For non-perpendicular incident flow, the modelled plume is not mixed sufficiently into the wake zone (see e.g. Fig. 36, bottom left) which can be attributed to a recirculation field that is too narrow (compare to Fig. 14).

In order to demonstrate the influence of additional turbulence on the concentration distribu-

tions, the calculations for the building height 28 m were performed in a separate run without these fields, see Figs. 41 to 43. The reduced turbulence yields less mixing of the plume in the ambient air and therefore smaller plume widths which in turn lead to higher concentrations for the elevated top source and to lower concentrations for the two near-ground sources. For the considered scenarios, the agreement with measured concentrations is considerably reduced if the additional turbulence fields are not taken into account.

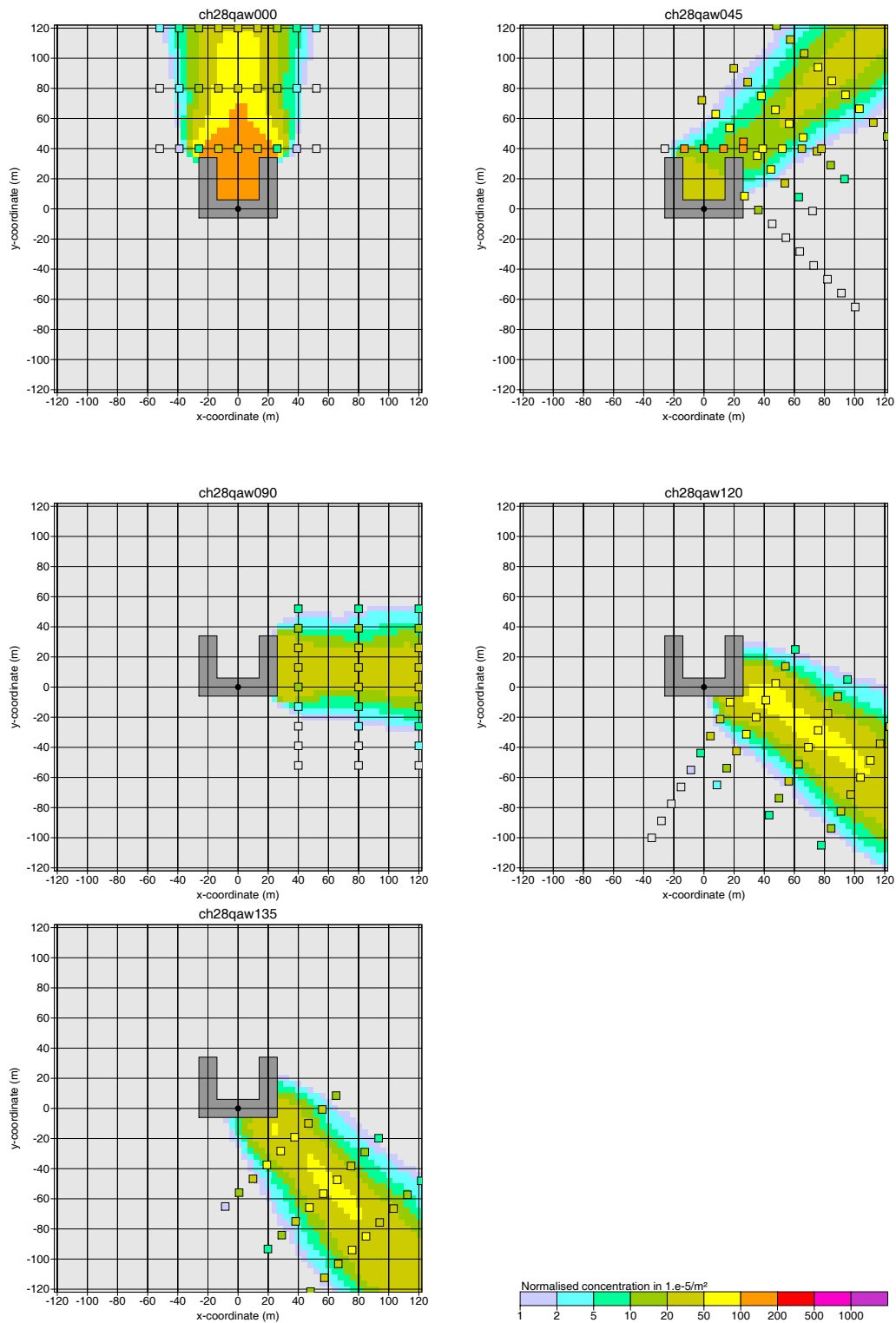


FIGURE 35: Concentration distribution near ground for an U-shaped building ($H = 28$ m) and different directions of the incoming flow (background: model results, squares: measurements). Source A (gray point).

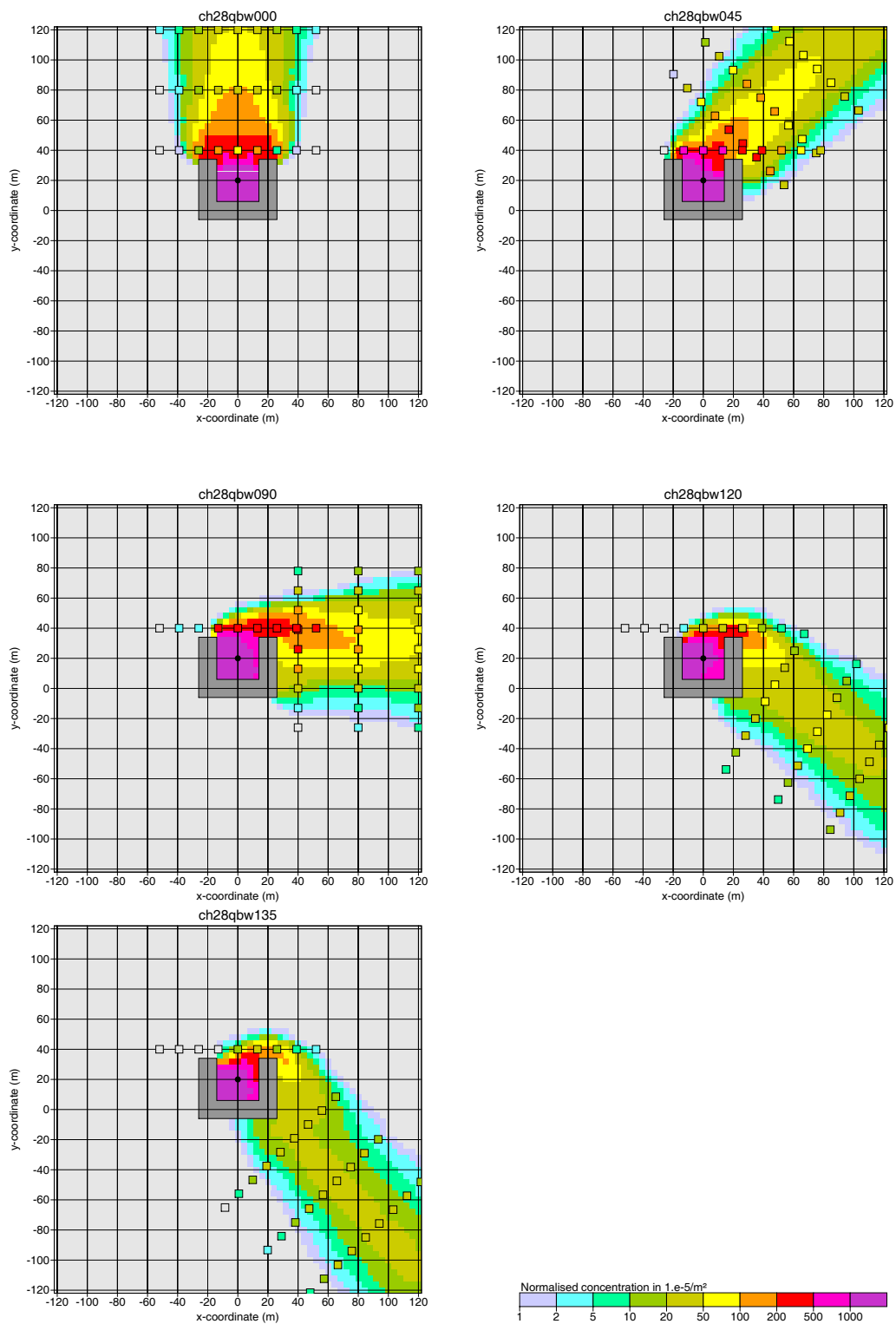


FIGURE 36: Concentration distribution near ground for an U-shaped building ($H = 28$ m) and different directions of the incoming flow (background: model results, squares: measurements). Source B (gray point).

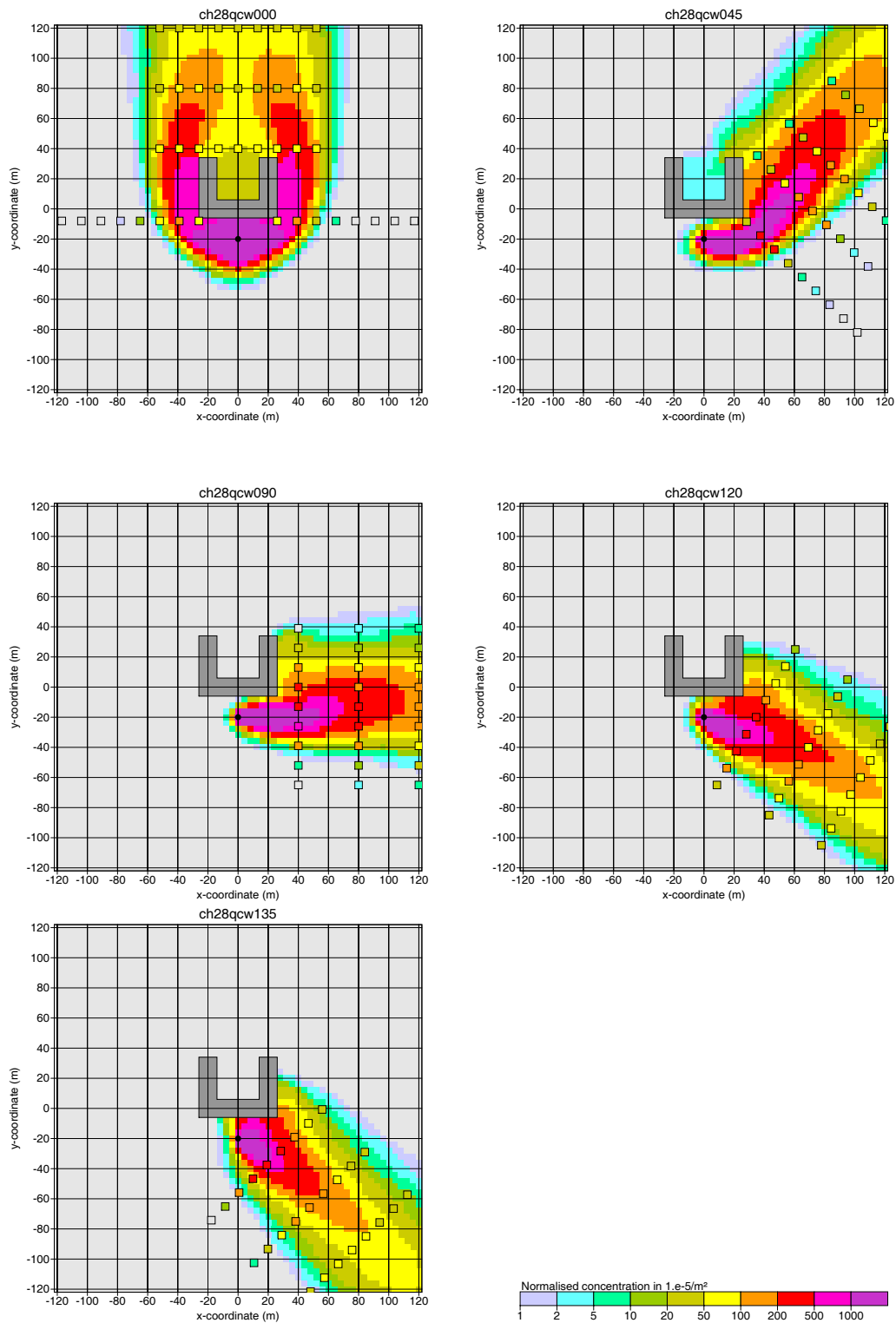


FIGURE 37: Concentration distribution near ground for an U-shaped building ($H = 28$ m) and different directions of the incoming flow (background: model results, squares: measurements). Source C (gray point).

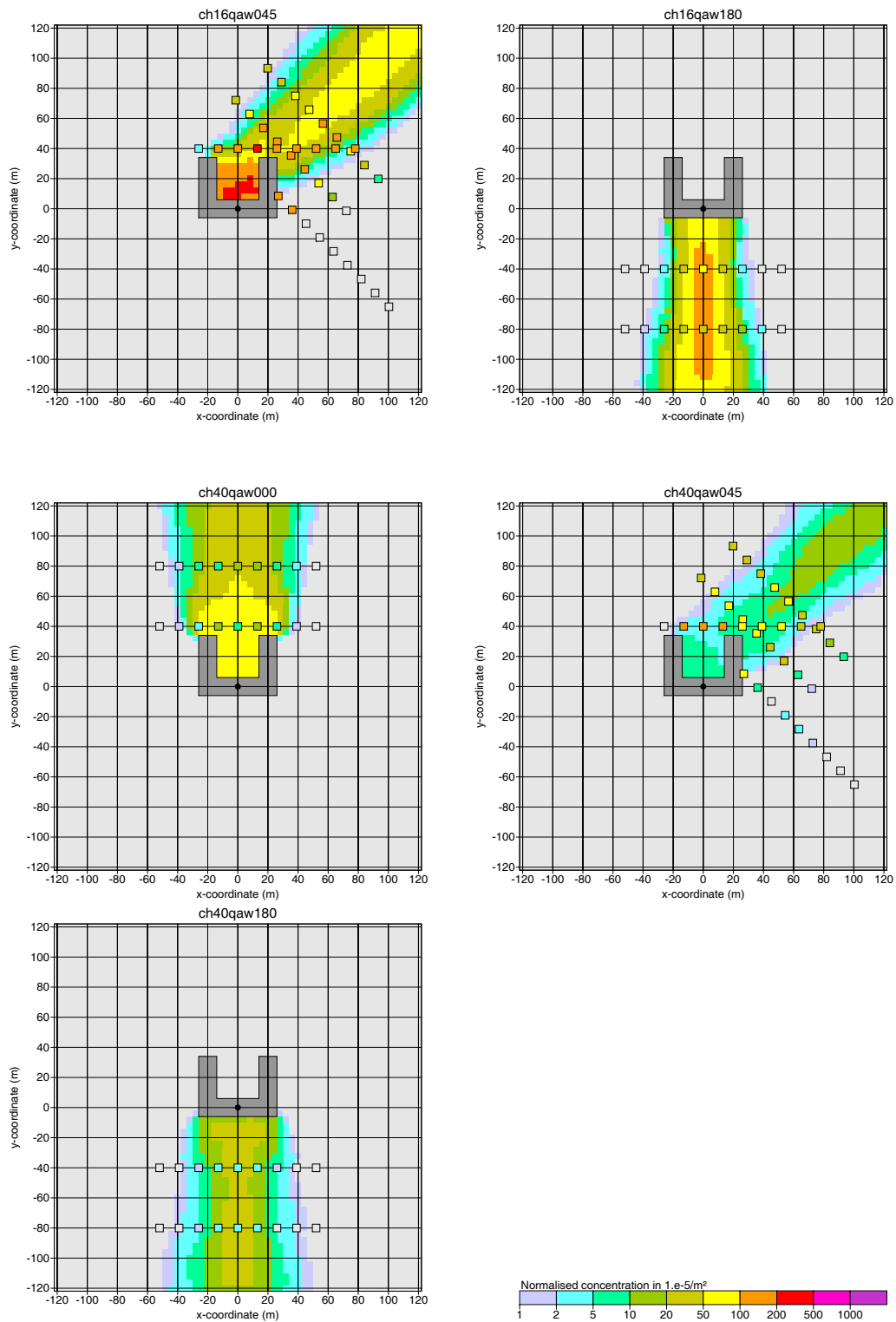


FIGURE 38: Concentration distribution near ground for an U-shaped building (top: $H = 16$ m; middle and bottom: $H = 40$ m) and different directions of the incoming flow (background: model results, squares: measurements). Source A (gray point).

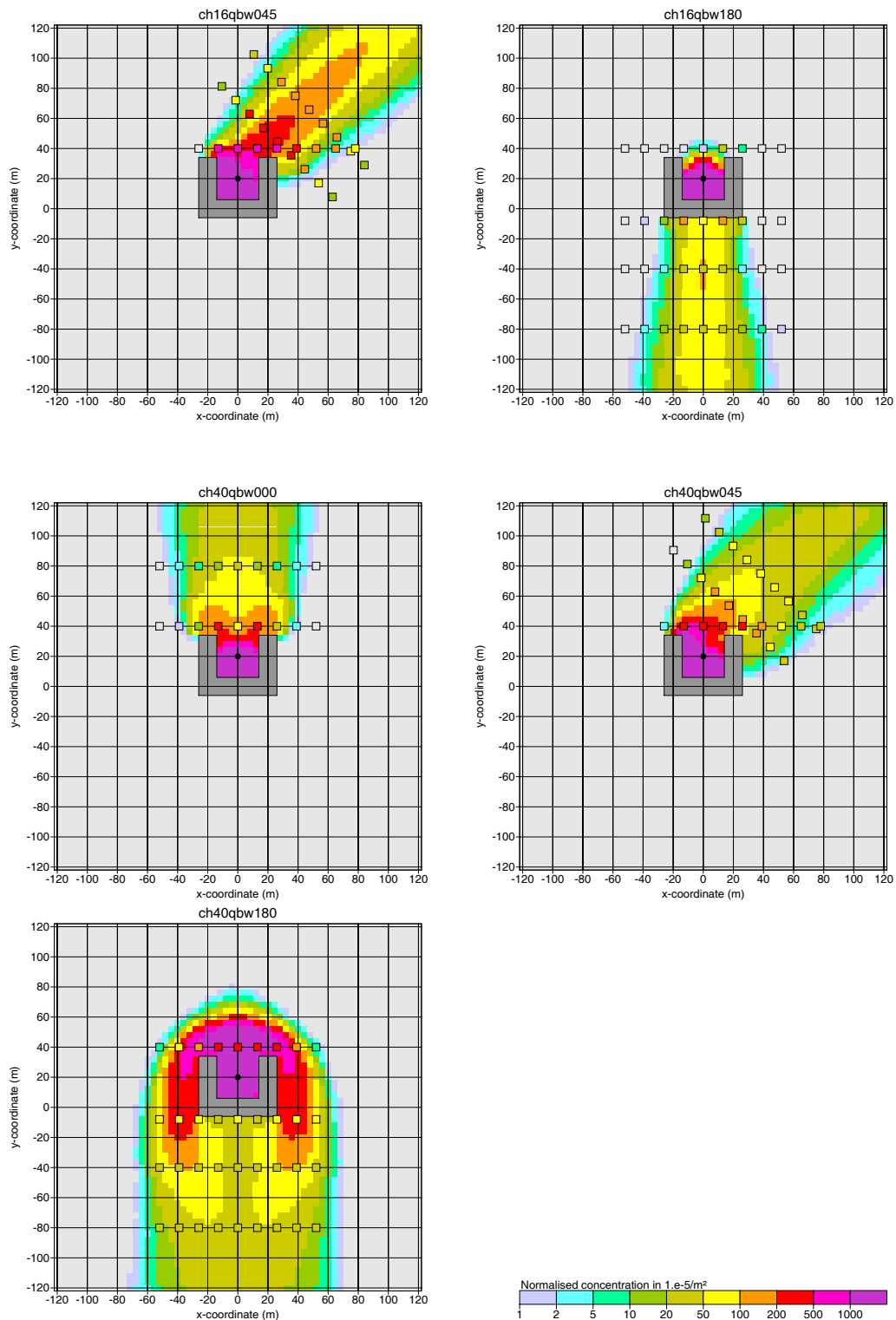


FIGURE 39: Concentration distribution near ground for an U-shaped building (top: $H = 16$ m; middle and bottom: $H = 40$ m) and different directions of the incoming flow (background: model results, squares: measurements). Source B (gray point).

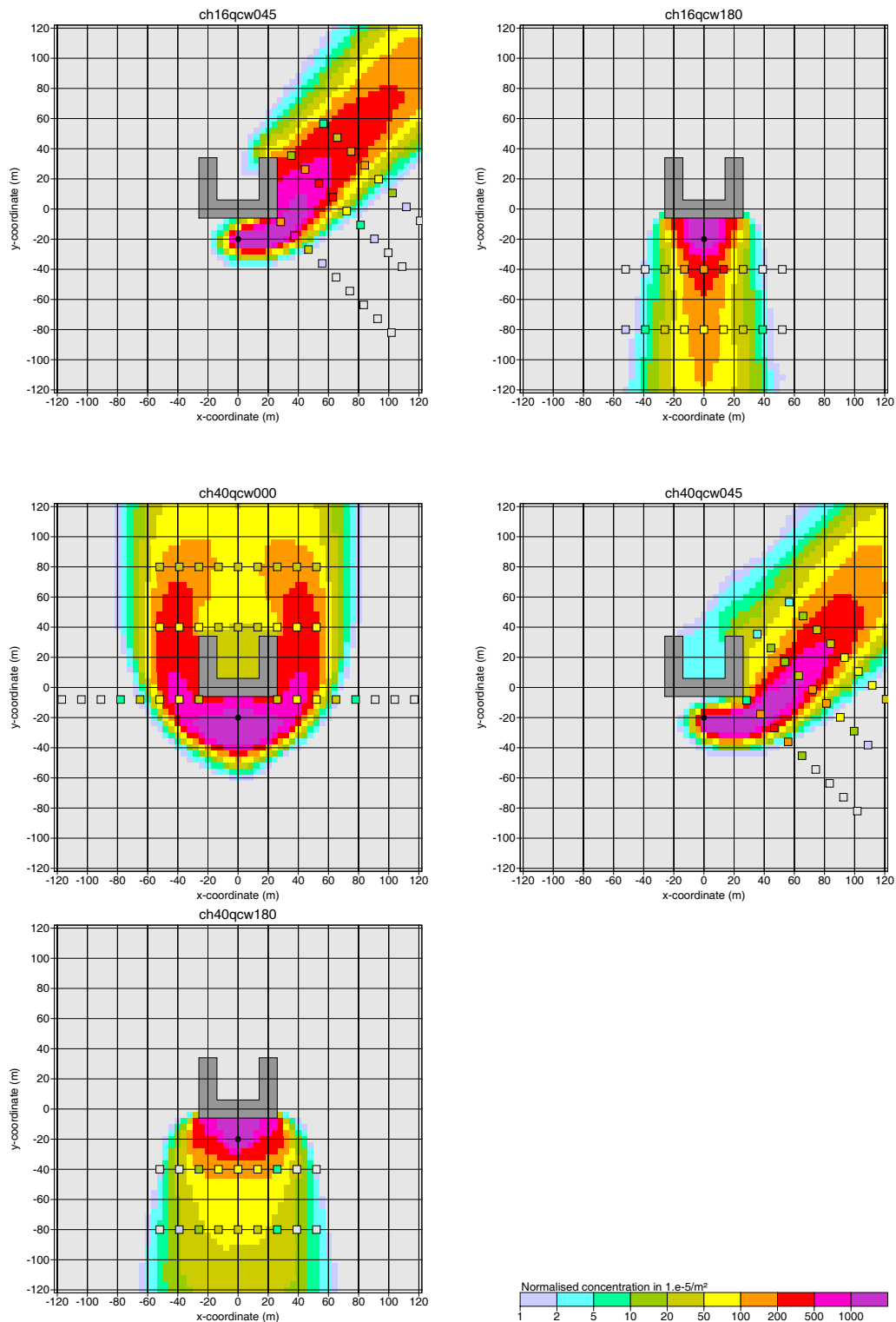


FIGURE 40: Concentration distribution near ground for an U-shaped building (top: $H = 16$ m; middle and bottom: $H = 40$ m) and different directions of the incoming flow (background: model results, squares: measurements). Source C (gray point).

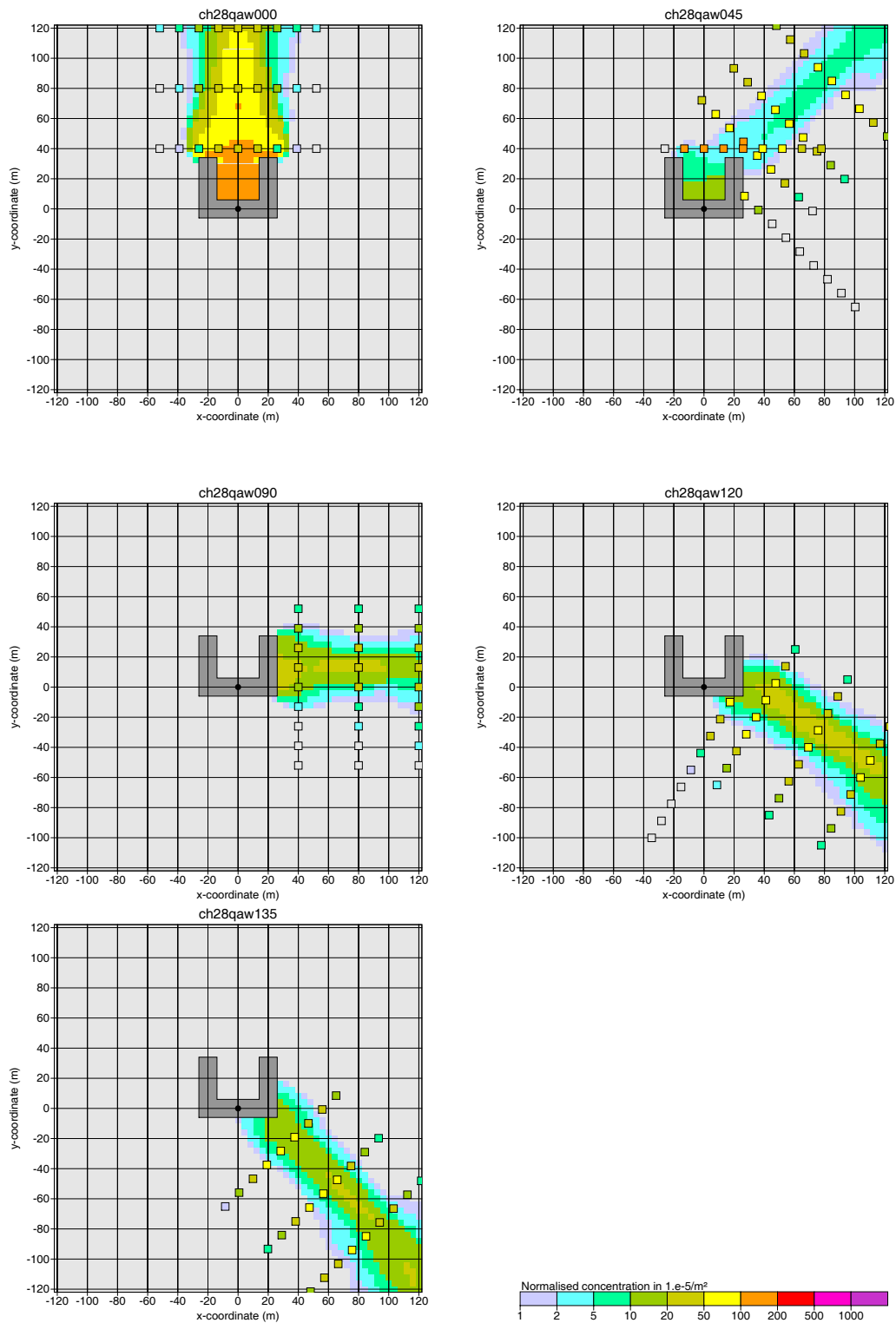


FIGURE 41: Test runs without additional turbulence: Concentration distribution near ground for an U-shaped building ($H = 28$ m) and different directions of the incoming flow (background: model results, squares: measurements). Source A (gray point).

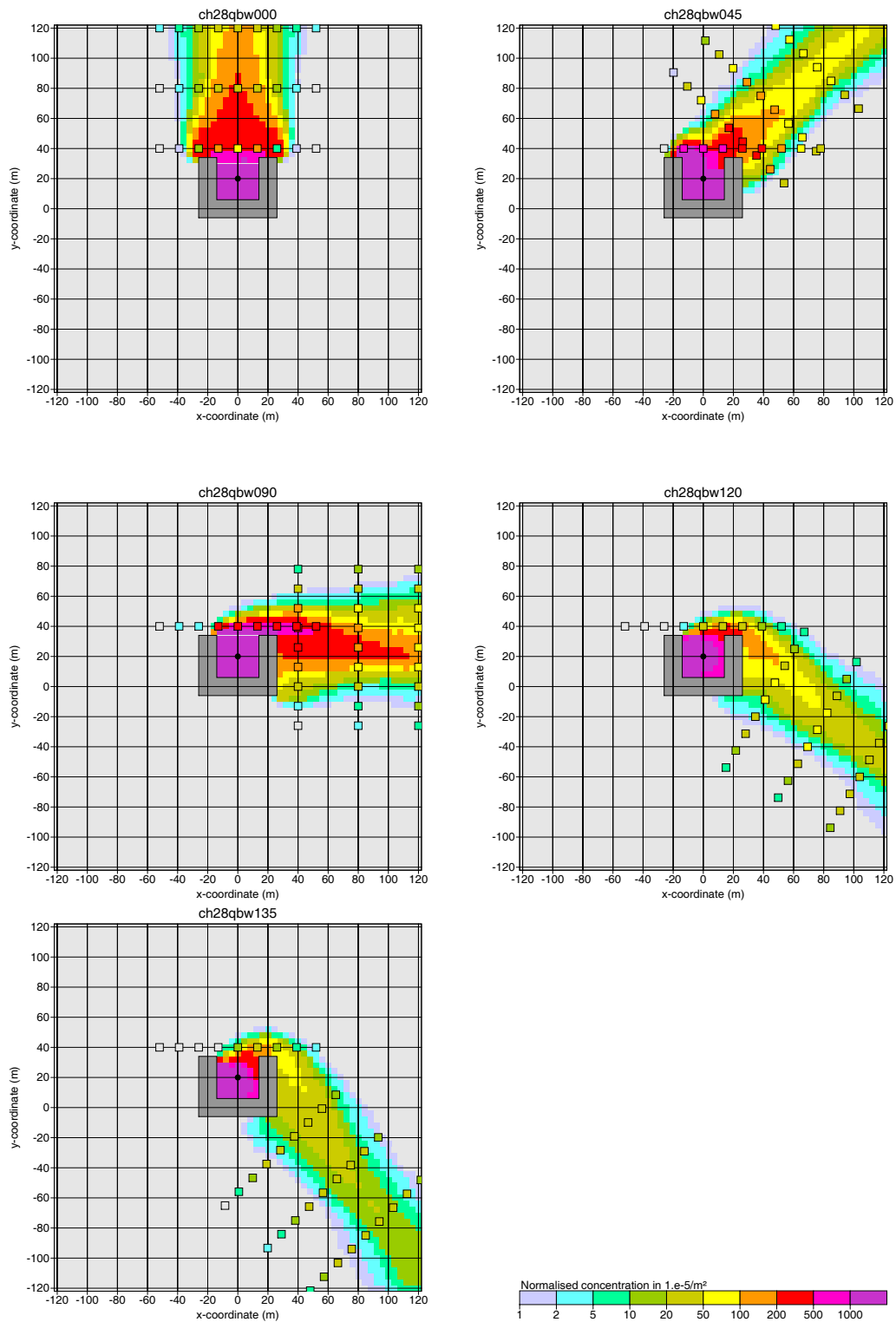


FIGURE 42: Test runs without additional turbulence: Concentration distribution near ground for an U-shaped building ($H = 28$ m) and different directions of the incoming flow (background: model results, squares: measurements). Source B (gray point).

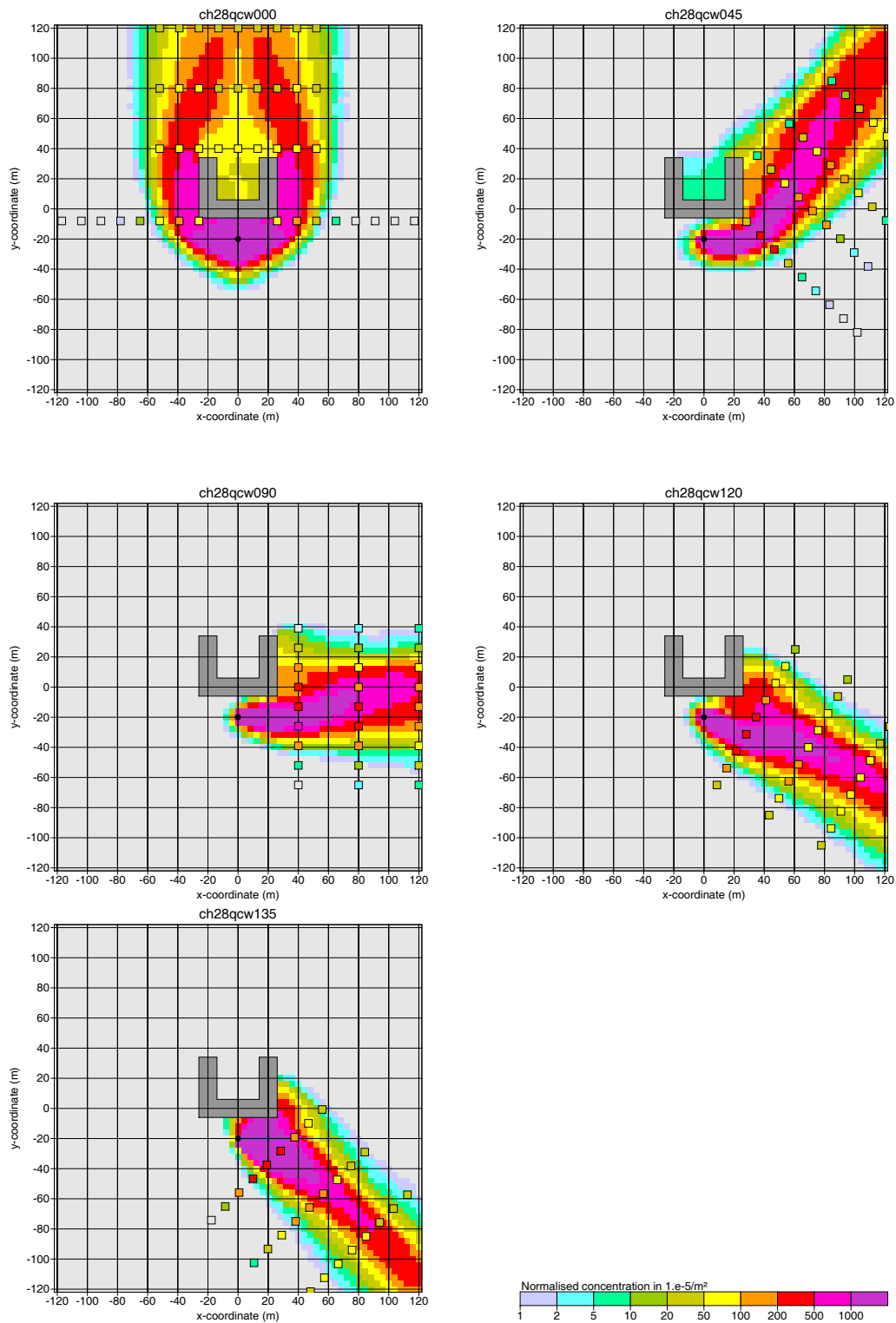


FIGURE 43: Test runs without additional turbulence: Concentration distribution near ground for an U-shaped building ($H = 28$ m) and different directions of the incoming flow (background: model results, squares: measurements). Source C (gray point).

4.4.2 Cooling tower

The wind tunnel measurements ($u_A = 2.4$ m/s, $h_A = 80$ m) carried out for the cooling tower in Emsland (see section 4.3.2) yielded the following main results with respect to the concentration distributions near ground (SCHATZMANN & LOHMEYER, 1991):

- For the zero case (no buildings) the maximum concentration due to the stack of height 160 m appeared at a source distance of about 1700 m.
- In the presence of the cooling tower (height 152 m, diameter 80 m), the concentration maximum increased by a factor of 1.5 when the source was located in the front of the tower (wind direction 120 deg) and by a factor 1.7 when the source was located in the lee of the tower (wind direction 295 deg). The distance of the maximum from the source was in both cases reduced to about 1000 m to 1100 m.

When applying these experimental findings it must be taken into account that even for the zero case the data contain a vertical plume offset for which a satisfactory explanation had not been found (Janicke, 1992) and that had been accounted for in accompanying model calculations by a reduction of the source height from 160 m to 130 m. This modified emission height was used as well in the following dispersion calculations. In addition, the default meteorological profiles were used without considering the specific features of the wind tunnel (see Janicke, 1992).

Fig. 44 and Fig. 45 show the concentration distribution near ground for the incoming flow directions 120 deg and 295 deg without and with cooling tower, respectively. The distance between source and tower is 340 m. The x axis is oriented parallel to the wind direction 116 deg for which the tower is located exactly in the lee of the source. The blue point denotes the location of the source, the gray circle the location of the tower. In addition, location and value of the maximum concentration is displayed in the graphs ($u_A = 2,4$ m/s, $h_A = 80$ m, $z_0 = 1.5$ m, $d_0 = 9$ m, $\Delta x = 20$ m, $\Delta z = 20$ m).¹⁴

The concentration maximum near ground appears in the model calculations at a source distance of about 2000 m for the zero case and in the presence of the tower at about 1000 m. The amplification factor is 1.4 for the incident flow direction of 120 deg and 1.6 for 295 deg. This is in close agreement with the experimental observations.

If the additional turbulence fields are not taken into account in the dispersion calculation, the amplification factor is about unity, hence the concentration enhancement near ground is primarily caused by the enhanced turbulence in the wake zone of the cooling tower.

¹⁴In principle, the concentration distribution for the zero case is identical for both directions of the incoming flow. The small differences in the source distance and height of the maximum concentration are due to the statistical uncertainty of the calculated concentration values (about 2 %).

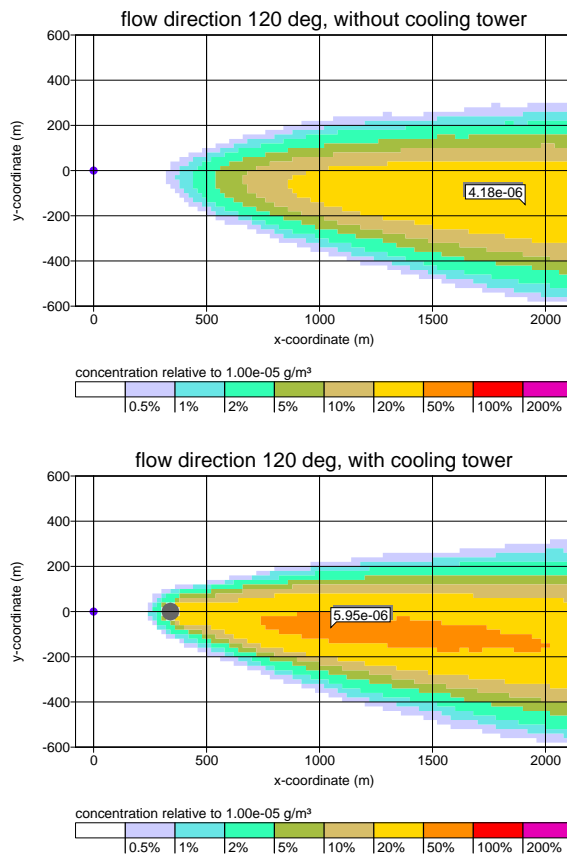


FIGURE 44: Cooling tower in Emsland, calculated concentration distribution near ground for an incoming flow direction of 120 deg. Top: Without tower (zero case). Bottom: With tower. The text fields denote the concentration maxima.

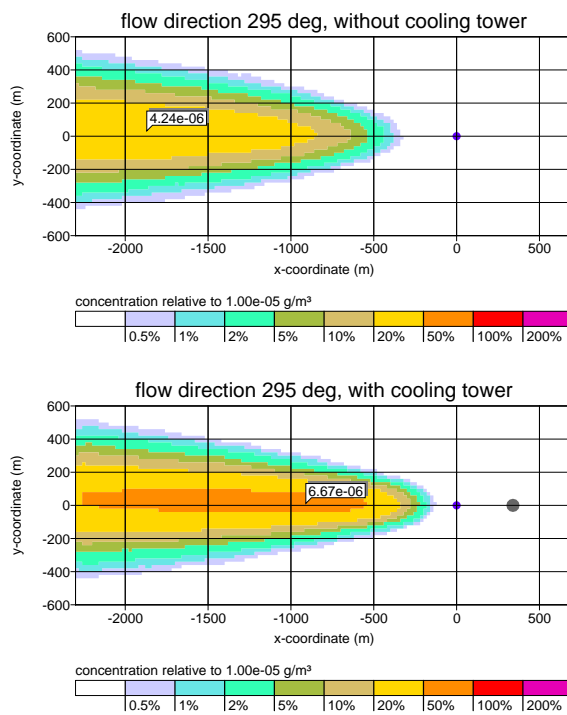


FIGURE 45: Cooling tower in Emsland, calculated concentration distribution near ground for an incoming flow direction of 295 deg. Top: Without tower (zero case). Bottom: With tower. The text fields denote the concentration maxima.

4.4.3 CEDVAL data set D1-4 (Uttenweiler)

The CEDVAL data set D1-4 contains concentrations measurements carried out at the wind tunnel of the Meteorological Institute of the University of Hamburg in the context of a BW-PLUS project (odour field inspections for a barn complex at Uttenweiler; BÄCHLIN ET AL., 2002; LEITL ET AL., 2002).

The concentration distribution of a tracer gas emitted from two stacks SI and SII located at the roof of a pig barn was determined in the wind tunnel. A somewhat higher forage stable was located at the side of the barn. The locations of buildings, sources, and the coordinate system are displayed in Fig. 46. For the calculations, the source height was set to 8.5 m and the building heights were set equal to the according ridge heights (in rounded numbers 8 m for the pig barn and 10 m for the forage stable).¹⁵

For an incoming flow from the direction of the forage stable, the maximum concentrations of the plume were measured at the lee side of the pig barn at distances of $x = 50$ m and $x = 100$ m from source SII for different heights. Both the sum and the individual concentrations resulting from source SI and SII were determined.

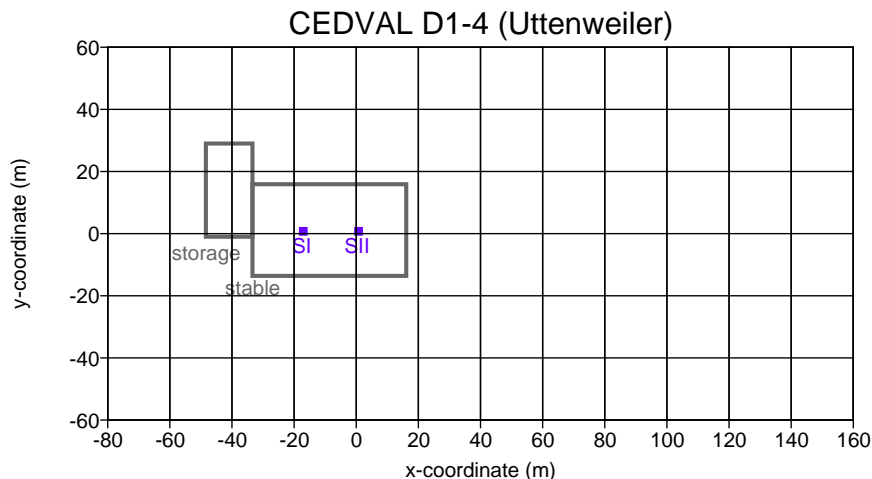


FIGURE 46: Location of buildings and sources applied in the dispersion calculations for the CEDVAL data set D1-4.

The measured concentrations and the results of the dispersion calculation are shown in Fig. 47 ($u_A = 3$ m/s, $h_A = 10$ m, $z_0 = 0.06$ m, $d_0 = 0$ m, $\Delta x = 3$ m, $\Delta z = 2$ m, source exit velocity 3 m/s, source diameter 1.5 m). The centre graph contains in addition the model results at $x = 75$ m. The diamonds represent the measured values and the bars the modelled ones (red: source SI, green: source SII, blue: sum of both sources). The graphs show the maximum concentration normalized by the concentration at the source exit C_s , C_m . For the

¹⁵The cited numbers for source and ridge heights differ in the two referenced project reports. The values used in the present study are consistent with the ones given in the report of the Meteorological Institute which according to an enquiry are the correct ones. On the other hand, the assignment of the source names SI and SII given in that report are not consistent with the ones given in the documentation of the CEDVAL data set D1-4. According to an enquiry the assignments of the latter are correct and were applied in this study.

calculations, C_s was determined from the given values of emission strength, exit velocity, and source diameter.

The measured concentration near ground takes its maximum at a distance of about 50 m, the modelled one at about 80 m. Both measured and modelled data show slightly larger concentration values for the lee-side source SII.

The following aspects can play a role in the differences between the measured and modelled concentrations:

- It is not clear whether for the present situation plume rise is described adequately by the formulas given in guideline VDI 3782 part 3 for cold sources that were applied in the calculations. For example, the more detailed plume rise model PLURIS yields a slightly different slope of the plume axis. In addition, plume rise and local wind and turbulence fields are treated independently in the dispersion calculation.
- The actual roof slopes are neglected in the calculations.
- The boundary layer model of guideline VDI 3783 part 8 that was applied in the calculation is known to yield plumes that are too small for the studied situation (low source heights, small roughness length).

Because the last item has probably the strongest influence on the concentration distribution, a test calculation was carried out for comparison using the default boundary layer model of LASAT which is known to yield more realistic plume widths.¹⁶ The results in Fig. 48 show that application of this boundary layer model gives almost exact agreement between measured and calculated concentrations at a distance of 100 m.

¹⁶For a comparison, see the validation results for the Prairie Grass Experiments in guideline VDI 3783 part 8 and in the BZU report No. 2 (JANICKE, L., JANICKE, U., 2000) which explains the boundary layer model applied in LASAT.

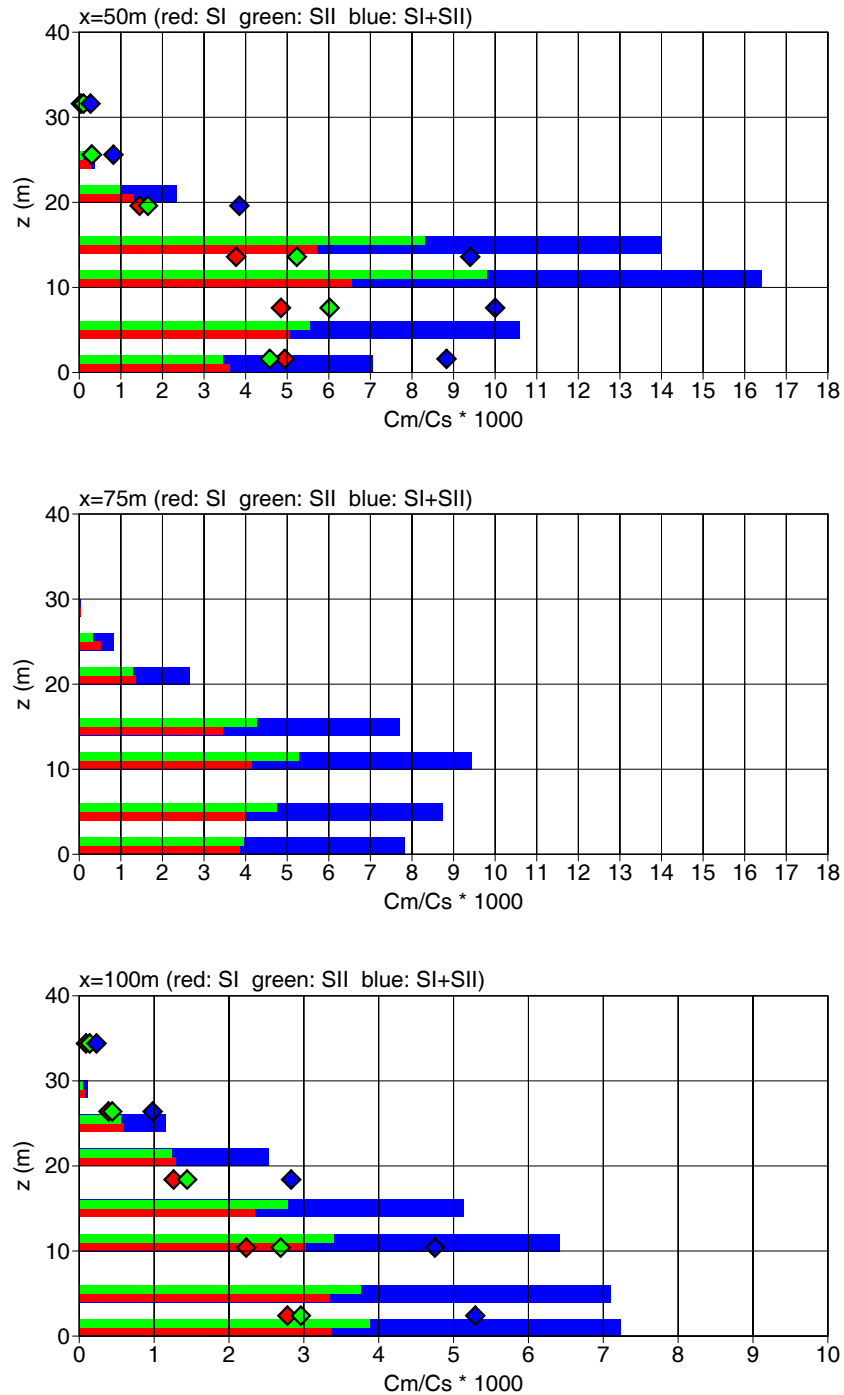


FIGURE 47: Maximum concentrations measured in the wind tunnel (diamonds) and calculated by the model (bars) for three distances from source SII.

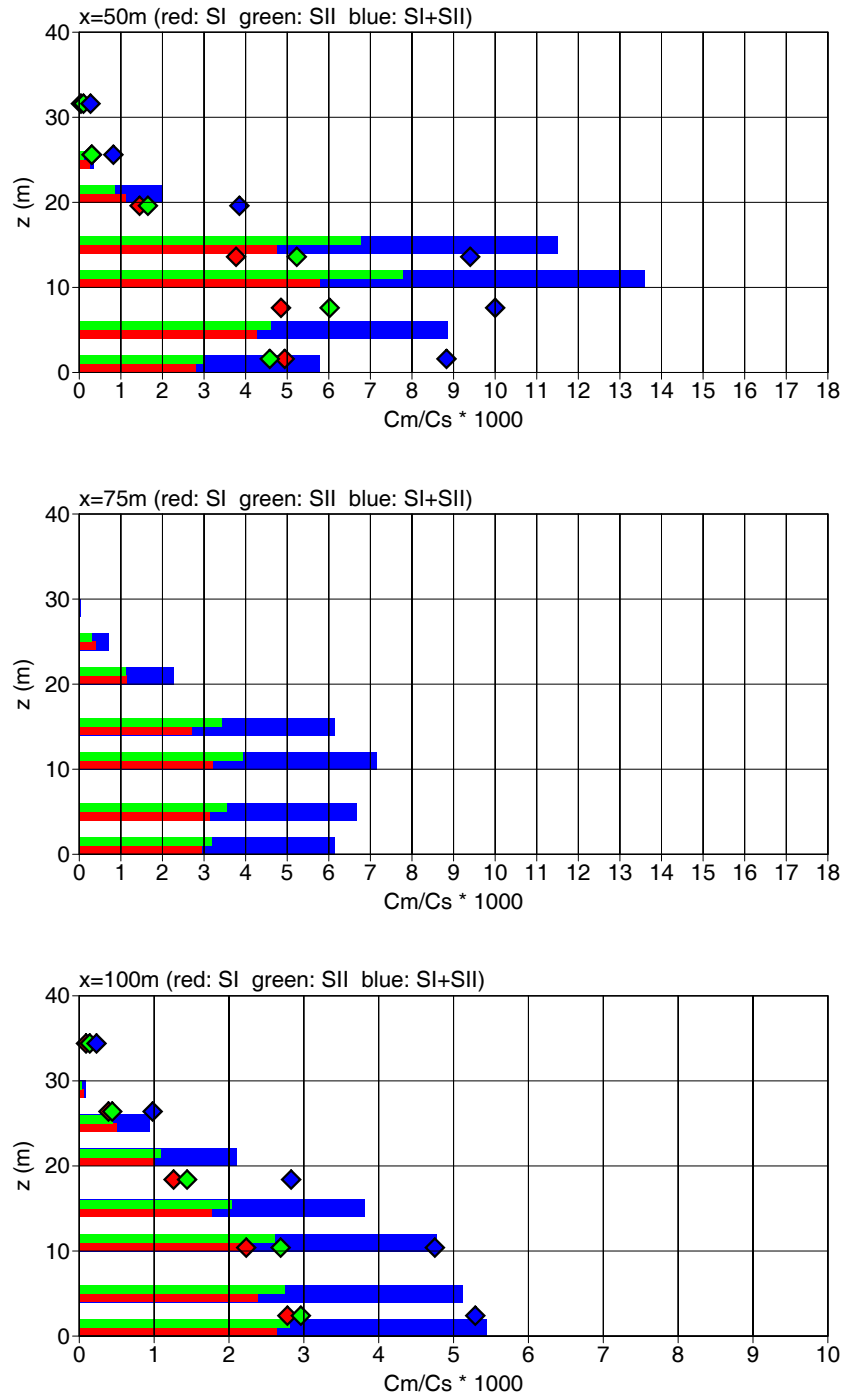


FIGURE 48: Like Fig. 47, but with application of the default boundary layer model of LASAT instead of the one of guideline VDI 3783 part 8.

4.4.4 Comparison with the prognostic wind field model MISKAM

So far the concentration comparisons were carried out for source heights that are not within the intended application range. For this range, i.e. source heights between 1.2 and 1.7 times the building height, no experimental validation data were available. In order to fill this gap to some extent, a dispersion calculation using the results of the prognostic wind field model MISKAM (version 4.22) was performed for comparison.¹⁷ The MISKAM fields were calculated and provided by Uwe Hartmann (Regional Environmental Authority (LUA), Essen).

Beside the wind field, MISKAM provided the complete field of diffusion coefficients which was applied in the dispersion calculations, too. Velocity fluctuations were not provided, here the undisturbed fluctuations according to guideline VDI 3783 part 8 were used instead. Hence, the following turbulence fields were applied:

Quantity	MISKAM	DMK
Diffusion coefficients	MISKAM	VDI 3783 part 8 plus additional fields from DMK
Velocity fluctuations	VDI 3783 part 8	VDI 3783 part 8 plus additional fields from DMK

Even for the zero case without buildings, MISKAM applies diffusion coefficients different from guideline VDI 3783 part 8. Fig. 49 depicts the concentration distribution near ground (source height 25 m) which results from an application of the boundary layer profiles of MISKAM and guideline VDI 3783 part 8, respectively ($z_0 = 0.2$ m, $d_0 = 0$ m, $h_A = 50$ m, $u_A = 5.17$ m, $\Delta x = 5$ m, $\Delta z = 3$ m). The MISKAM profiles yield smaller plume widths, the concentration integral across the plume is roughly the same for both cases.

A complex build-up area was used for the case with buildings. It was constructed from the building definitions of the street *Venloerstrasse* (see section 4.2.4) by twofold reflection, see Fig. 50. The heights of the grid-like buildings varied between 3 m and 21 m, the average building height was 9 m. A passive source of height 25 m was located once in the centre of symmetry (175 m/175 m) and once at the upper edge of a street canyon southwest(85 m/110 m). The maximum building height within a circle of 6 source heights around the source was 21 m, hence the source height equals 1.2 times this relevant building height.

Wind and turbulence fields were calculated for a wind rose in steps of 10 degree. The average over the isotropic wind rose of the near ground concentration is shown in Figs. 51 and 52 (parameters as for the zero case). For the centre source, both sets of model fields yield similar maximum concentrations, height concentration values being dominantly located within the street canyons. The details of the two concentration distributions are partly different. For the southwest source, the fields of the present model yield a maximum concentration that is about 30 % higher than the one obtained with the MISKAM fields; the high concentration values are located roughly in the same areas, but here as well the details of the distributions

¹⁷In both cases without a change of wind direction with height for the incident flow.

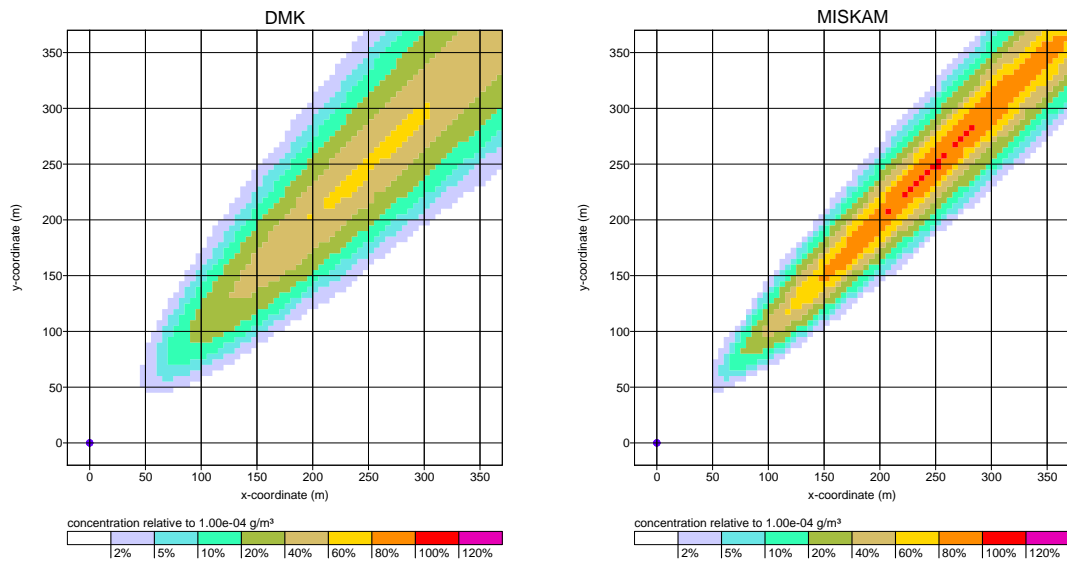


FIGURE 49: Concentration distribution near ground for the zero case without buildings and a constant wind direction. Left: Application of the profiles according to guideline VDI 3783 part 8. Right: Application of the MISKAM profiles.

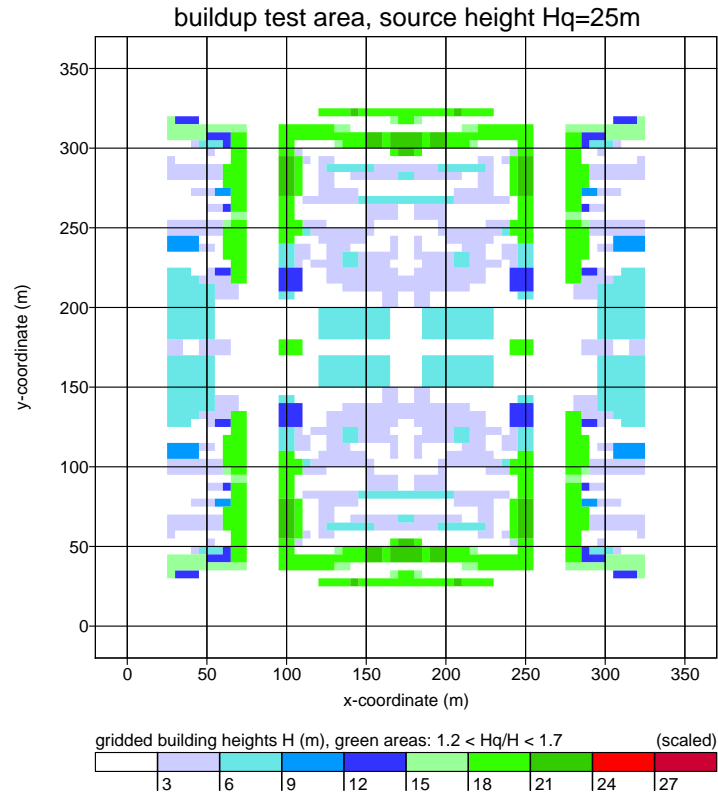


FIGURE 50: Rastered building shapes used for the comparison with MISKAM ($\Delta x = 5$ m, $\Delta z = 3$ m).

differ.¹⁸

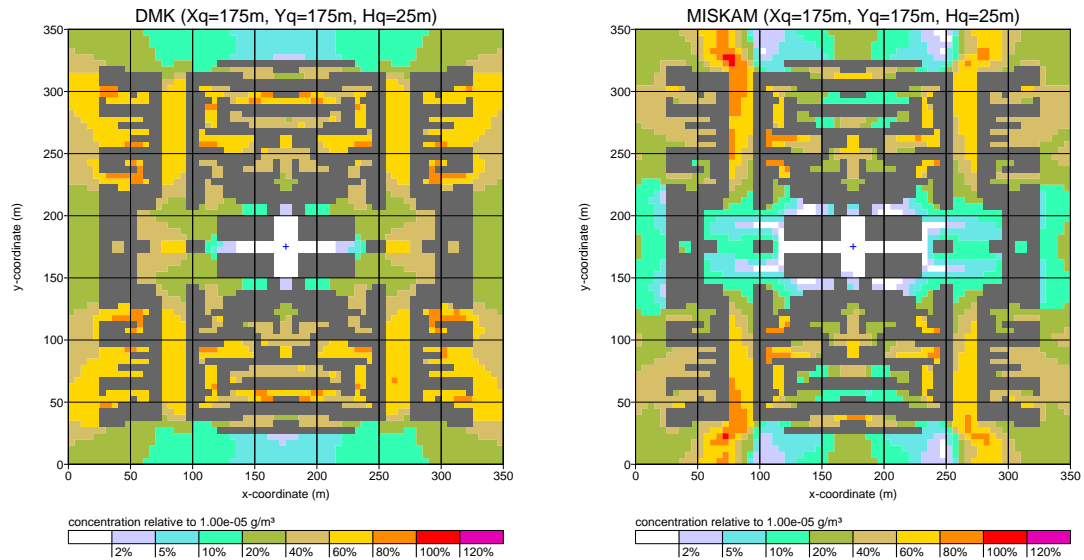


FIGURE 51: Concentration distribution near ground for an isotropic wind rose, centre source. Left: Application of the fields of the present model. Right: Application of the MISKAM fields.

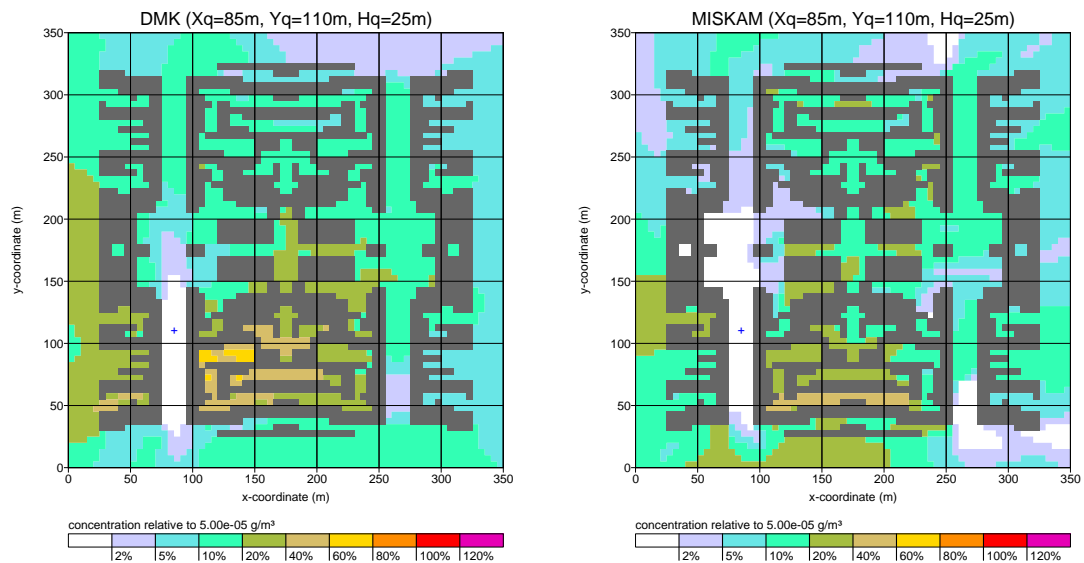


FIGURE 52: Concentration distribution near ground for an isotropic wind rose, southwest source. Left: Application of the fields of the present model. Right: Application of the MISKAM fields.

¹⁸On applying the MISKAM fields, systematically higher concentrations appear in the western street canyon despite the fact that the configuration is symmetric. The reason for this is under investigation.

5 Transition to elevated sources

According to the instructions of the *TA Luft*, buildings can be accounted for by means of a roughness length and displacement height instead of a diagnostic wind field model if the source height exceeds 1.7 times the building height. This approach is based on the idea that for emissions well above the top edge of a building, the main effect of the building with respect to the concentration near ground is an enhancement of the vertical mixing – which can be produced also by means of an increased surface roughness.

For emissions close to an isolated building, the influence of the building decreases with increasing elevation of the source above the building because the plume disperses more and more in a region that is not affected by the building. For extended build-up structures or larger distances between emission source and building, building effects become the smaller the more homogeneous the undisturbed plume is spread out within the influence zone of the buildings. Finally, the effects of enhanced vertical mixing due to buildings are small if the dilution capability of the undisturbed atmosphere is already good; the more unstable the atmospheric stratification and the larger the surface roughness length, the better the dilution capability.

In order to test these dependencies and to study the transition from an application of a diagnostic wind field model to a consideration of buildings by means of a surface roughness length and displacement height, the following test scenarios were investigated:

1. *Extended build-up structure from the comparison with MISKAM, source at 1.7 times the maximum building height, isotropic wind rose.*

The concentration distribution near ground, calculated by accounting for the complex build-up structure explicitly with $z_0 = 0.2$ m and $d_0 = 0$ m (see section 4.4.4), is compared to the one calculated without buildings but with $z_0 = 1.5$ m and $d_0 = 7.2$ m (d_0 corresponds to 0.8 times the average building height in accordance with appendix 3 of the *TA Luft*). The value $z_0 = 0.2$ m used in the former calculation is in agreement with the findings for the streets *Bonnerstrasse* and *Venloerstrasse*, see section 4.2.4.

2. *Single building, source heights of 1.7, 2.0, and 2.5 times the building height, different values for z_0 , isotropic wind rose.*

The building height is 20 m, the source is located on top of the building and in a second run 40 m in front of the building. Using the roughness lengths 0.2 m, 0.5 m, 1 m, and 1.5 m according to the classes given in the *TA Luft*, the calculations are carried out both with and without accounting for the building explicitly. In addition, a calculation with $z_0 = 2$ m without building is performed. The displacement height is set according to the *TA Luft* to 6 times the roughness length.

3. *Single building, source height of 1.7 times the building height, different values for z_0 , meteorological statistics anonym.aks.¹⁹*

¹⁹The statistics anonym.aks is part of the program package AUSTAL2000 and provided by the German Meteorological Service (DWD) free of charge.

The building is the same as in test set 2, the source is located on top of the building. The applied roughness lengths are 0.2 m, 0.5 m and 1.5 m, both with and without accounting for the building explicitly. In addition, a calculation with $z_0 = 2$ m without building is performed. The displacement height is set according to the *TA Luft* to 6 times the roughness length.

For test set 3, the effective anemometer height was set according to the specifications of the German Meteorological Service (14.4 m for $z_0 = 0.5$ m, 24.4 m for $z_0 = 1.5$ m, 28.3 m for $z_0 = 2$ m). They result from the condition that the wind speed derived from the standard logarithmic wind profile is independent of the roughness length at a height of 60 m. In agreement with this methodology, the wind speed was set to a fixed value at a height of 60 m for the first two test sets (5.17 m/s for test set 1, 5.0 m/s for test set 2). Neutral atmospheric stratification was assumed for the first two test sets.

The results are shown in Figs. 53 (test set 1), 54 to 56 (test set 2), and 57 (test set 3).²⁰

For the build-up case of test set 1, the maximum concentrations derived with $z_0 = 0.2$ m and explicit modelling of the buildings are comparable to the ones obtained with $z_0 = 1.5$ m without buildings.

For the individual building in test sets 2 and 3 and a source height of 1.7 times the building height, the maximum concentrations derived with explicit modelling of the building are comparable to the ones obtained without building and a surface roughness length increased by two classes. For a source height of 2.5 times the building height (test set 2), an increase by one class is sufficient for a conservative estimate of the maximum concentration.

Based on these findings, the following recommendations can be made for an application of the *TA Luft* to source heights exceeding 1.7 times the building heights and roughness lengths between 0.2 m and 1.5 m:

- For densely build-up areas and explicit modelling of the buildings by means of a diagnostic wind field model, the values $z_0 = 0.2$ m and $d_0 = 0$ m can be used by default. If buildings are accounted for via an increased roughness length and displacement height, z_0 should be set to at least 1.5 m and d_0 according to the *TA Luft* to 0.8 times the average building height to estimate the maximum long term average of the concentration near ground.
- For a source close to an isolated building complex, the maximum long term average of the concentration near ground can be estimated in a calculation without wind field model by means of a roughness length increased by two classes (classes according to the *TA Luft* and $d_0 = 6z_0$). For source heights exceeding 2.5 times the building height, an increase by one class is sufficient.

²⁰The absolute concentration maximum in test set 2 for a source height of 50 m and roughness lengths 0.2 m and 0.5 m is located outside the computation area.

Hence, in a calculation for source heights exceeding 1.7 times the building heights and without explicitly accounting for the buildings by means of a wind field model, one must sort out a suitable roughness length instead of applying the average roughness length that is proposed by AUSTAL2000. The recommendations given in this section can assist here. However, they may not be sufficient or may lead to an overestimation of the concentrations. In case of doubts it is preferable not to use the simplified approach of an increased roughness length but to account for the buildings by means of a wind field model explicitly.

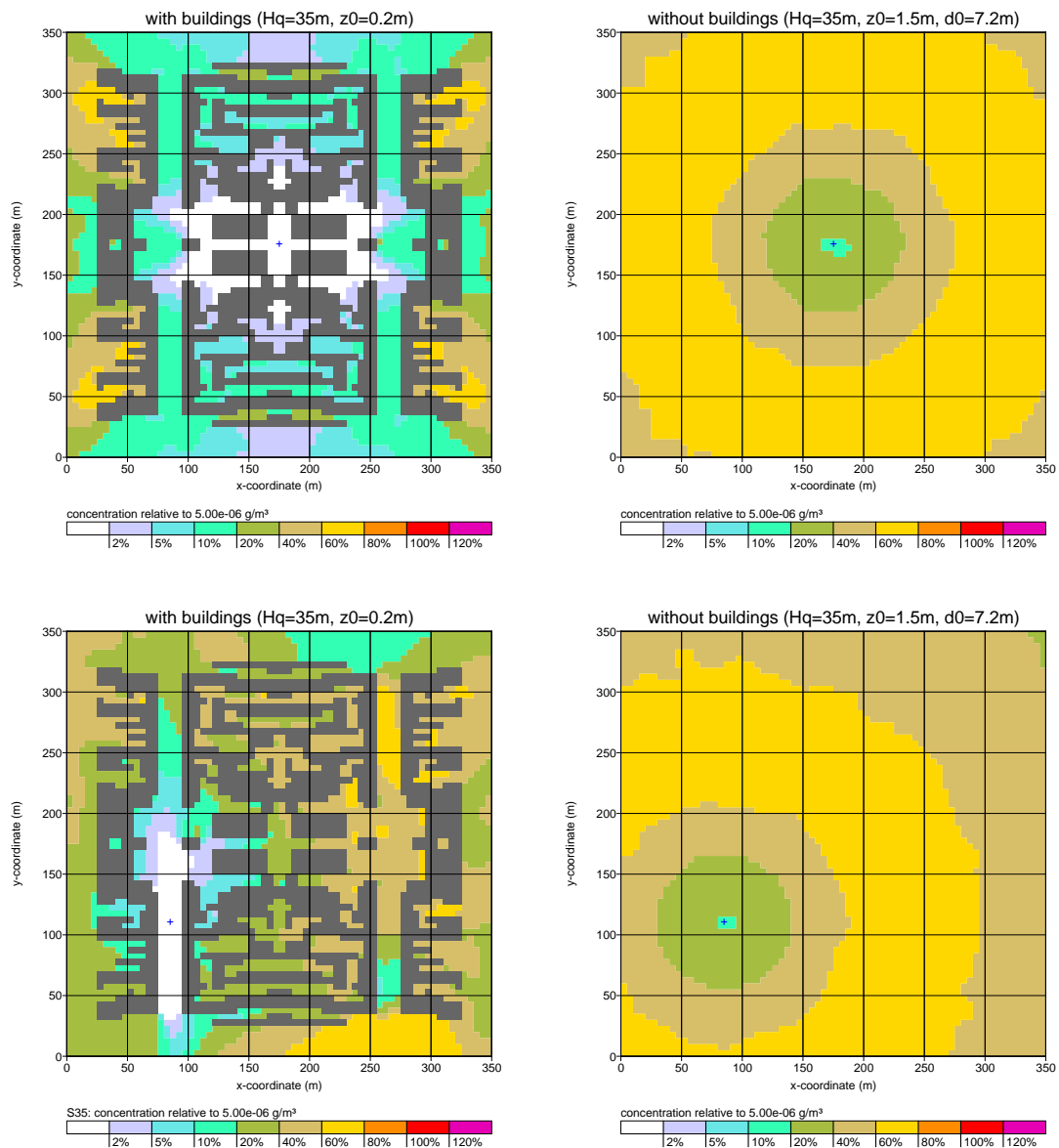


FIGURE 53: Transition to elevated sources. Isotropic wind rose, densely build-up area, source height 35 m (1.7 times the building heights). Concentration distribution near ground obtained by explicit modelling of the buildings (left) and by applying an increased roughness length (right). In the upper two graphs, the source (blue cross) is located in the centre of symmetry, in the two lower ones in the street canyon southwest.

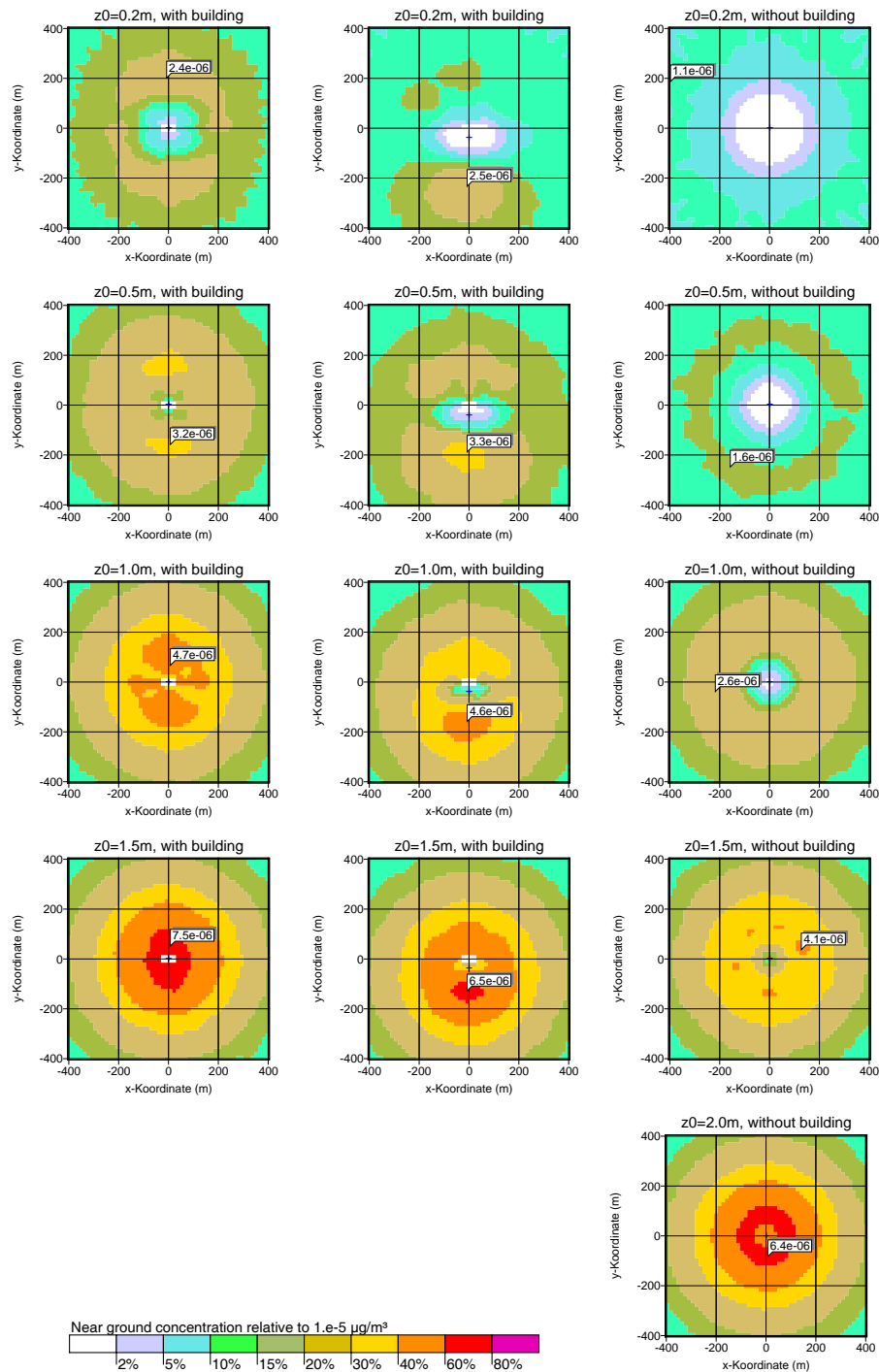


FIGURE 54: Transition to elevated sources. Isotropic wind rose, source height 34 m (1.7 times the building height). Concentration distribution near ground. Left: Source at 0 m/0 m with building. Middle: Source at 0 m/-40 m with building. Right: Source at 0 m/0 m without building. Roughness lengths from top to bottom: 0.2 m, 0.5 m, 1.0 m, 1.5 m, 2 m.

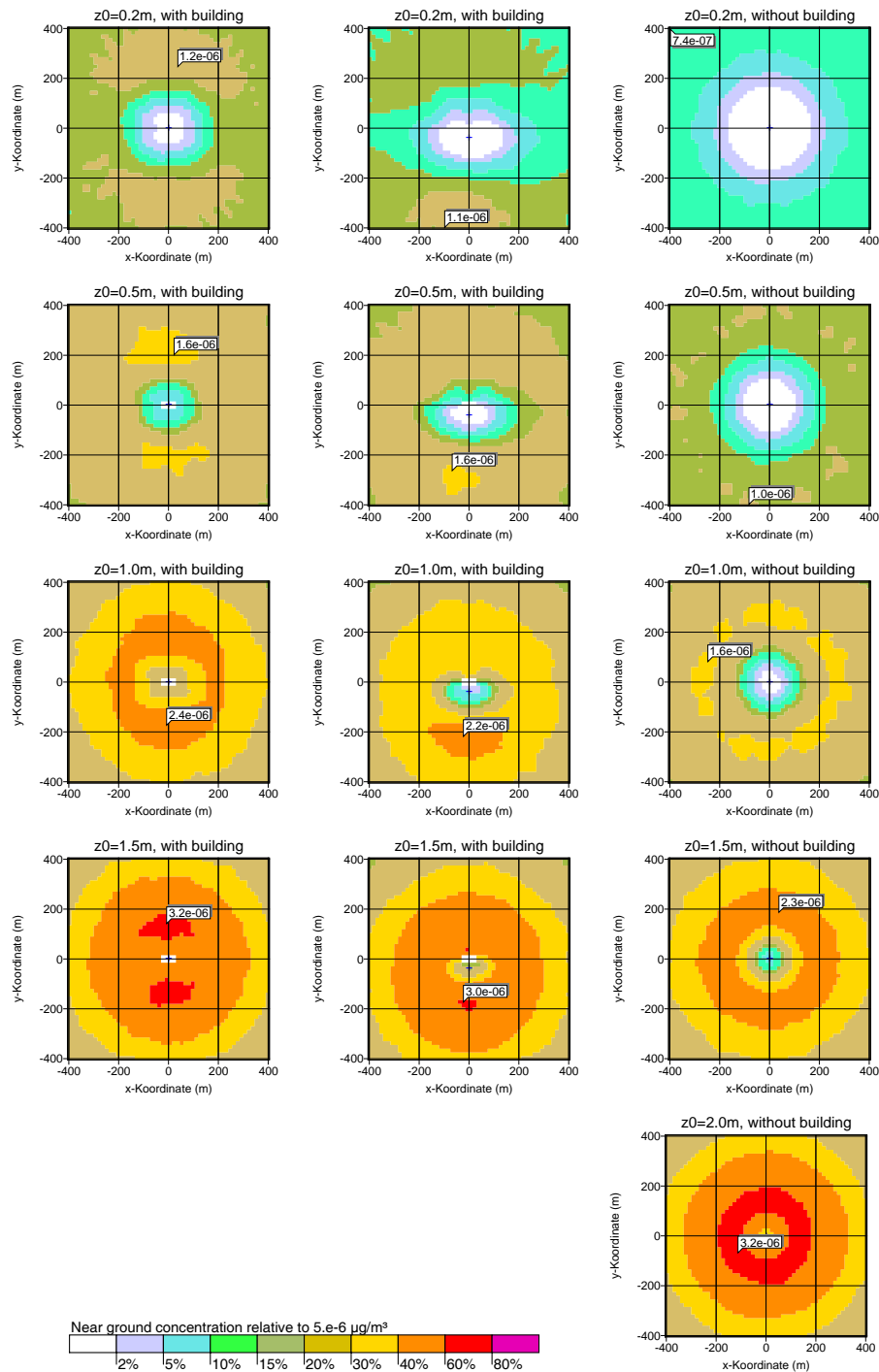


FIGURE 55: Transition to elevated sources. Isotropic wind rose, source height 40 m (2 times the building height). Concentration distribution near ground. Left: Source at 0 m/0 m with building. Middle: Source at 0 m/-40 m with building. Right: Source at 0 m/0 m without building. Roughness lengths from top to bottom: 0.2 m, 0.5 m, 1.0 m, 1.5 m, 2 m.

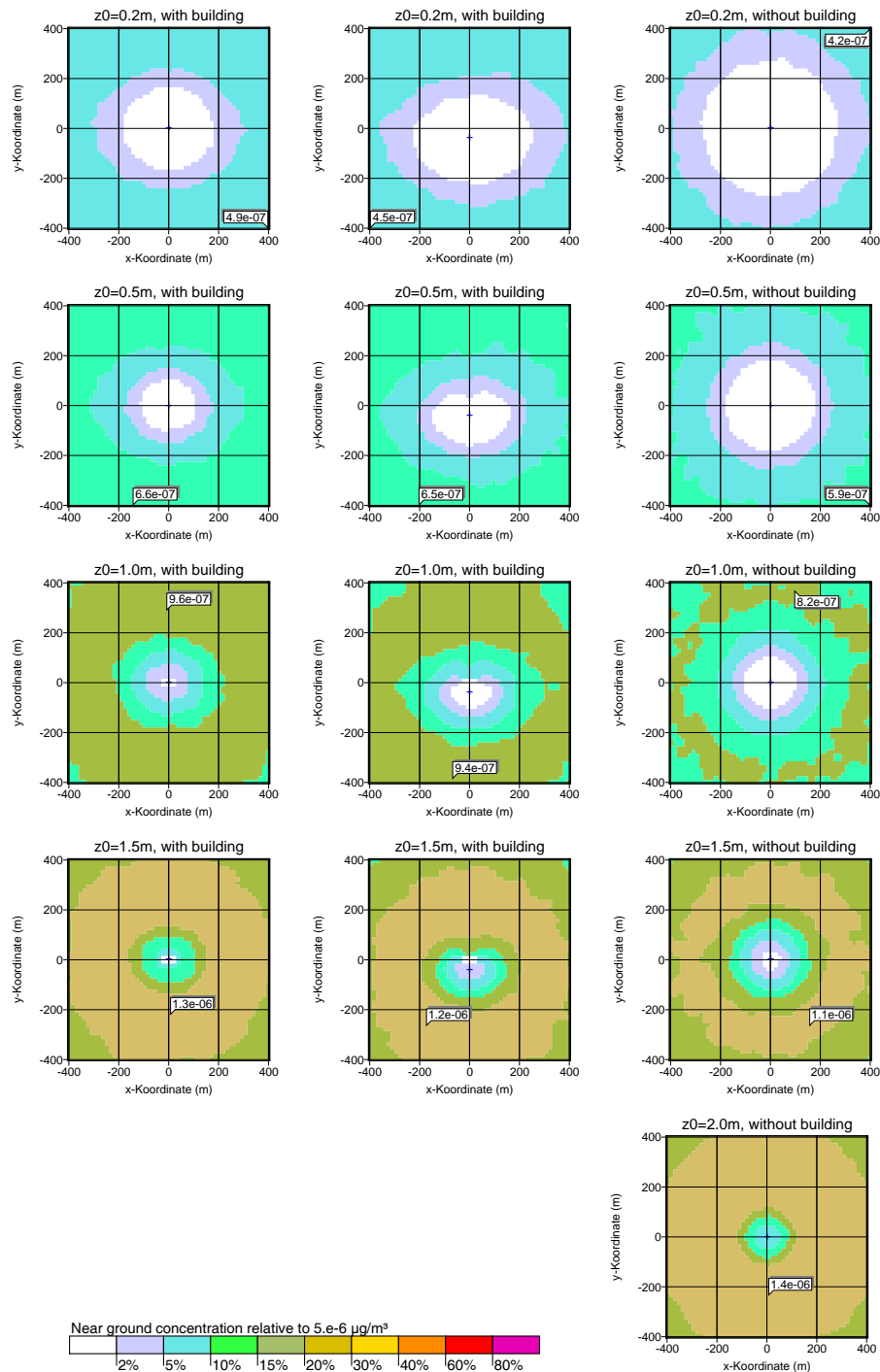


FIGURE 56: Transition to elevated sources. Isotropic wind rose, source height 50 m (2.5 times the building height). Concentration distribution near ground. Left: Source at 0 m/0 m with building. Middle: Source at 0 m/-40 m with building. Right: Source at 0 m/0 m without building. Roughness lengths from top to bottom: 0.2 m, 0.5 m, 1.0 m, 1.5 m, 2 m.

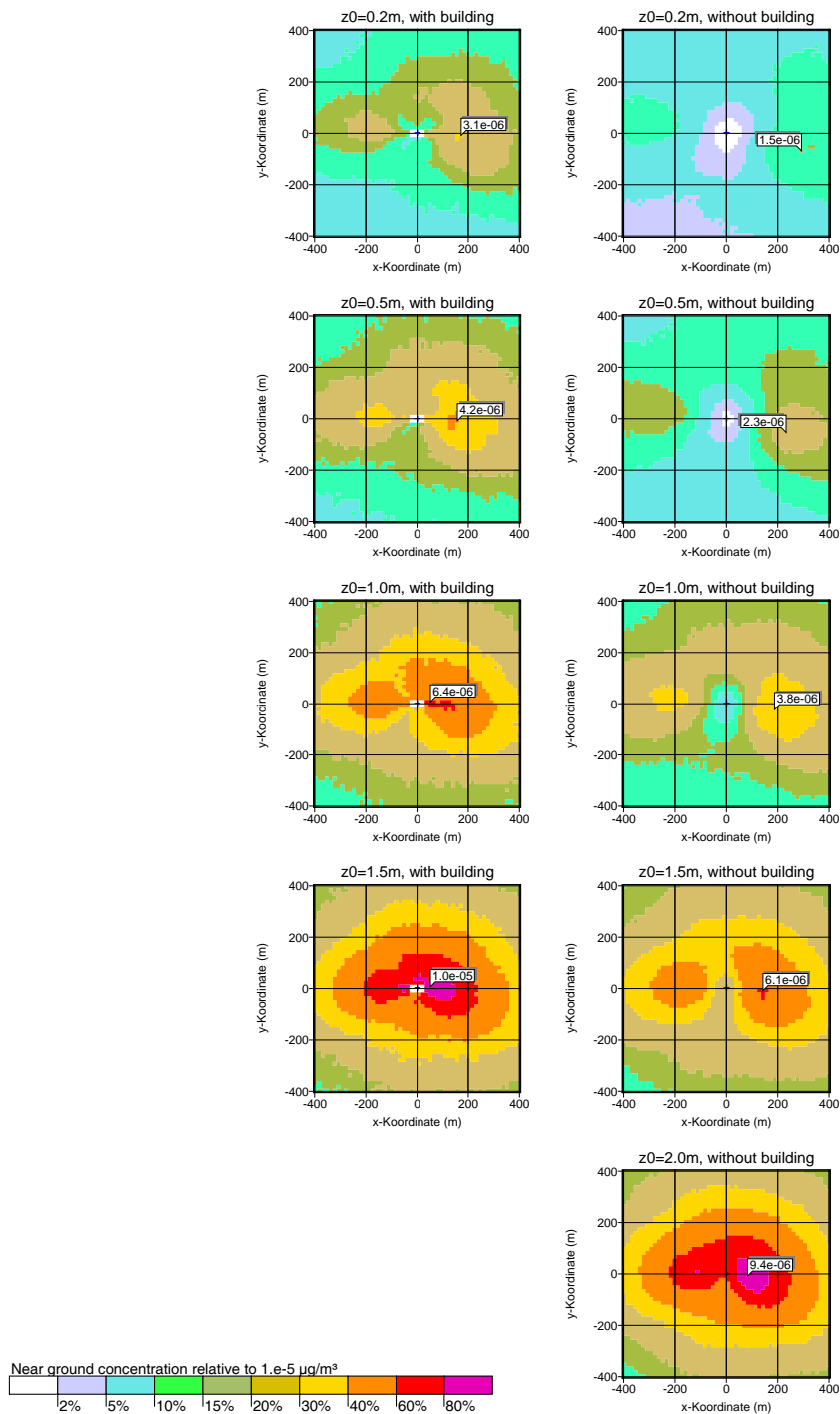


FIGURE 57: Transition to elevated sources. Meteorological statistics anonym. aks, source height 34 m (1.7 times the building height). Concentration distribution near ground. Left: With building. Right: Without building. Roughness lengths from top to bottom: 0.2 m, 0.5 m, 1.0 m, 1.5 m, 2 m.

6 Summary

The technical instruction *TA Luft* envisions for source heights between 1.2 and 1.7 times the building height the application of a diagnostic wind field model. So far such a model has not been part of AUSTAL2000 as the model DMW (model according to guideline VDI 3783 part 10) envisioned originally had turned out not to be well suited. Aim of this project was the development of a diagnostic wind field model (called DMK) that would overcome the shortcomings of DMW.

The verification showed that the model results are, as demanded, to a large extent independent of the way buildings are specified and on their orientation relative to the calculation grid. In addition, a simple approach was developed that allows to account in a dispersion calculation for the additional velocity fluctuations and diffusion coefficients induced by the buildings.

Model fields and concentration distributions obtained in combination with AUSTAL2000 were validated on the basis of various experimental data sets. For concentration distributions, experimental data sets were only available for source heights below 1.2 times the building height. The validations show good overall agreement of model results and experimental observations without systematic overestimations or underestimations.

The tests for elevated sources above 1.7 times the building height indicate that for the calculation of long time means, a relatively smooth transition from the application of a wind field model to an increased roughness length can be achieved, as envisioned by the *TA Luft*.

The comparisons with a more complex wind field model and the tests along the concept change for elevated sources imply that one must reckon on uncertainties of up to 30 % for the calculation of long time means of the concentration near ground due to the chosen modelling concept when building influences play an important role. The uncertainty may be higher for individual situations.

7 References

TA LUFT (2002): Technical Instruction on Air Quality Control (*TA Luft*) from 2002-06-24. GMBI. 2002, Volume 25-29, p. 511-605. Internet: www.bmu.de/files/taluft.pdf.

VDI 3783 PART 8 (2002): Environmental Meteorology; Measurement-Based Turbulence Parameterization for Dispersion Models. Beuth, Berlin.

VDI 3783 PART 9 (DRAFT) (2003): Environmental Meteorology; Prognostic Wind Field Models for the Microscale; Evaluation of the Flow around Buildings and Obstacles. Beuth, Berlin.

VDI 3783 PART 10 (2001): Environmental Meteorology; Diagnostic Wind Field Models for the Microscale; Flow around Buildings and Obstacles. Beuth, Berlin.

BÄCHLIN, W., RÜHLING, A., LOHMEYER A. (2002): Bereitstellung von Validierungsdaten für Geruchsausbreitungsmodelle – Naturmessungen / *preparation of validation data sets for odour dispersion models – outdoor measurements*. Ing.-Büro Lohmeyer, Forschungsbericht FZKA-BWPLUS, Förderkennzeichen BWE 20003 / *Lohmeyer Consulting, Research Report FZKA-BWPLUS, Grant Number BWE 20003*.

CEDVAL (2004): The CEDVAL Project (compilation of experimental data for the validation of microscale dispersion models), supported by the Federal Environmental Agency, Grant Number 296 43 831). Internet: <http://www.mi.uni-hamburg.de/cedval>.

HOSKER, R.P. (1984): *Flow and diffusion near obstacles*, in: Atmospheric Science and Power Production, SOE/TIC-27601. ISBN 0-87079-126-5.

JANICKE, L. (1992): Programm zur Prüfung der Kühlturmeinflüsse beim Kernkraftwerk Emsland – Ausbreitungsmodellierung / *program for testing the influences of the cooling tower at the nuclear power station Emsland – dispersion modelling*. Ing.-Büro Janicke, im Auftrag des Ing.-Büros Lohmeyer / *Janicke Consulting, on behalf of Lohmeyer Consulting*.

JANICKE, L., JANICKE, U. (2000): Vorschlag eines meteorologischen Grenzschichtmodells für Lagrangesche Ausbreitungsmodelle / *proposal for a meteorological boundary layer model for Lagrangian dispersion models*. *Berichte zur Umweltphysik / Reports on Environmental Physics* Nummer / *Number 2*, Auflage / *Edition 1*, Ingenieurbüro Janicke / *Janicke Consulting*, ISSN 1439-8222.

KASTNER-KLEIN, P., PLATE, E.J. (1998): Windkanalversuche zur Verbesserung der Ermittlung von KFZ-bedingten Konzentrationsverteilungen in Stadtgebieten / *wind tunnel measurements towards a better determination of concentration distributions in urban areas caused by motor traffic*. Forschungsbericht FZKA-PEF 295001, Institut für Hydrologie und Wasserwirtschaft, Universität Karlsruhe / *Research Report FZKA-PEF 295001, Institute of Hydrology and Water Economy, University of Karlsruhe*.

KLEIN, P., RAU, M. WANG, Z., PLATE, E.J. (1994): Ermittlung des Strömungs- und Konzen-

trationsfeldes im Nahfeld typischer Gebäudekonfigurationen (Experimente) / *determination of flow and concentration fields in the near field of typical building configurations (experiments)*. Forschungsbericht KfK-PEF 124, Kernforschungszentrum Karlsruhe / *Research Report KfK-PEF 124, Nuclear Research Centre Karlsruhe*.

LEITL, B., AUBRUN, S., SCHATZMANN, M. (2002): Bereitstellung systematischer Vergleichsdaten für die Entwicklung und Validierung numerischer Geruchsausbreitungsmodelle – Windkanalversuche im Verbundprojekt Geruchsfreisetzung und -ausbreitung / *preparation of systematic data sets for the development and validation of numerical odour dispersion models – wind tunnel measurements in the context of the project odour emission and dispersion*. Meteorologisches Institut der Universität Hamburg, Forschungsbericht FZKA-BWPLUS, Förderkennzeichen BWE 20001 / *Meteorological Institute of the University of Hamburg, Research Report FZKA-BWPLUS, Grant Number BWE 20003*.

SCHATZMANN, M., LOHMEYER, A. (1991): Programm zur Prüfung der Kühlturmeinflüsse, Kernkraftwerk Emsland, Veränderung der Abluftausbreitung durch Kühlturm und Gebäude / *project to examine the influence of cooling towers, nuclear power station Emsland, modification of dispersion due to cooling tower and buildings*. Projekt 172, im Auftrag des NLOE / *project 172, on behalf of the Regional Environmental Agency of Lower Saxony (NLOE)*.

A Mathematical calculation of the diagnostic wind field

The aim is to find a diagnostic wind field \mathbf{v} that is divergence-free and fulfills the boundary condition of vanishing normal component at the boundary faces, and that agrees at the same time as good as possible with a given empirical wind field \mathbf{u} .

An approach based on the quadratic mean error yields the following variational problem with the spatially dependent Lagrange multiplier $\lambda(\mathbf{r})$:²¹

$$\delta \left\{ \int d^3r \left[\frac{1}{2}(\mathbf{v} - \mathbf{u})^2 - \lambda \nabla \cdot \mathbf{v} \right] \right\} = 0 \quad (13)$$

The Lagrange equation corresponding to this variational problem is

$$\mathbf{v} = \mathbf{u} - \nabla \lambda \quad (14)$$

with the constraint

$$\delta \left\{ \int d^2f \cdot (\lambda \mathbf{v}) \right\} = 0 \quad (15)$$

For the boundary faces of the volume of interest, this constraint implies that λ must be zero if the normal component of \mathbf{v} is not specified and that λ is varied if the normal component is zero. The Lagrange equation yields

$$\nabla \cdot \mathbf{v} = \nabla \cdot \mathbf{u} - \nabla \cdot \nabla \lambda \quad (16)$$

Because the final wind field is divergence-free, this takes the form of a Poisson equation,

$$\nabla \cdot \nabla \lambda = \nabla \cdot \mathbf{u} \quad (17)$$

Hence, the diagnostic wind field \mathbf{v} is obtained by adding a gradient field $\nabla \lambda$ to the given empirical field \mathbf{u} . The gradient field is fixed by Eq. (17) and the boundary condition (15). The Poisson equation is solved numerically on a Cartesian grid using difference techniques.

²¹For diagnostic models on the mesoscale, different weighting factors are applied in the variational term for the deviations of horizontal and vertical components in order to account for the atmospheric stratification. For the flow around buildings this can be omitted.

Definition of the calculation grid

For each of the Cartesian coordinates x, y, z a point raster (x_i, y_j, z_k) is defined:

$$x_i \text{ for } i = 0..n_x$$

$$y_j \text{ for } j = 0..n_y$$

$$z_k \text{ for } k = 0..n_z$$

The intervals of a raster have their centre point at the coordinates

$$\hat{x}_i = (x_{i-1} + x_i)/2 \text{ for } i = 1..n_x$$

$$\hat{y}_j = (y_{j-1} + y_j)/2 \text{ for } j = 1..n_y$$

$$\hat{z}_k = (z_{k-1} + z_k)/2 \text{ for } k = 1..n_z$$

The intervals in the three axis directions, $\mathcal{D}_{x,i}, \mathcal{D}_{y,j}, \mathcal{D}_{z,k}$, own the same index values as their centre point. For example, $\mathcal{D}_{x,i}$ contains all x values in the range x_{i-1} to x_i ,

$$\mathcal{D}_{x,i} = \{x \mid x_{i-1} \leq x \leq x_i\}$$

The lengths \hat{d} of the intervals are

$$\hat{d}_{x,i} = x_i - x_{i-1} \tag{18}$$

$$\hat{d}_{y,j} = y_j - y_{j-1} \tag{19}$$

$$\hat{d}_{z,k} = z_k - z_{k-1} \tag{20}$$

The three point raster constitute a three-dimensional grid. The cells \mathcal{V}_{ijk} of the three-dimensional grid own the same indices as the corresponding axis intervals,

$$\begin{aligned} \mathcal{V}_{ijk} = \{(x, y, z) \mid x_{i-1} \leq x \leq x_i, y_{j-1} \leq y \leq y_j, z_{k-1} \leq z \leq z_k\} \\ \text{for } i = 1..n_x, j = 1..n_y, k = 1..n_z \end{aligned}$$

The volumes τ of the cells \mathcal{V} are given by

$$\tau_{ijk} = \hat{d}_{x,i} \hat{d}_{y,j} \hat{d}_{z,k} \tag{21}$$

In the following it is assumed that the horizontal mesh width of the grid is constant and the same for the two coordinate directions,

$$\hat{d}_{x,i} = \hat{d}_{y,j} = d \tag{22}$$

In an Arakawa-C grid, the velocity components are defined at the grid points for the axis direction that corresponds to the component and at the centre points for the two other directions. For example, v_x is defined at the points $(x_i, \hat{y}_j, \hat{z}_k)$. The index values of v_x are the same as the points at which the component is defined. hence the following relations apply:

$v_{x;ijk}$ is the value of v_x at $(x_i, \hat{y}_j, \hat{z}_k)$ with $i = 0..n_x$, $j = 1..n_y$, $k = 1..n_z$

$v_{y;ijk}$ is the value of v_y at $(\hat{x}_i, y_j, \hat{z}_k)$ with $i = 1..n_x$, $j = 0..n_y$, $k = 1..n_z$

$v_{z;ijk}$ is the value of v_z at $(\hat{x}_i, \hat{y}_j, z_k)$ with $i = 1..n_x$, $j = 1..n_y$, $k = 0..n_z$

Discretization of the Poisson equation

The field $\lambda(\mathbf{r})$ is defined at the centre points of the grid cells and its gradient, $\nabla\lambda = (\lambda_x, \lambda_y, \lambda_z)$, according to the specifications of Arakawa-C:

$$\hat{\lambda}_{ijk} = \lambda(\hat{x}_i, \hat{y}_j, \hat{z}_k) \quad (23)$$

$$\lambda_{x;ijk} = (\hat{\lambda}_{i+1,j,k} - \hat{\lambda}_{i,j,k})/d \quad (24)$$

$$\lambda_{y;ijk} = (\hat{\lambda}_{i,j+1,k} - \hat{\lambda}_{i,j,k})/d \quad (25)$$

$$\lambda_{z;ijk} = (\hat{\lambda}_{i,j,k+1} - \hat{\lambda}_{i,j,k})/d_{z;k} \quad (26)$$

$$d_{z;k} = (\hat{d}_{z;k} + \hat{d}_{z;k+1})/2 \quad (27)$$

The divergence of a vector field $\mathbf{v}(\mathbf{r})$ is calculated for every grid cell according to the Gaussian integral theorem, i.e. by the surface integral of the normal components divided by the cell volume,

$$\hat{D}_{ijk}\{\mathbf{v}\} = \frac{1}{\tau_{ijk}} \left[(v_{x;i,j,k} - v_{x;i-1,j,k})F_{x;k} + (v_{y;i,j,k} - v_{y;i,j-1,k})F_{y;k} + (v_{z;i,j,k} - v_{z;i,j,k-1})F_{z;k} \right] \quad (28)$$

$$F_{x;k} = d\hat{d}_{z;k} \quad (29)$$

$$F_{y;k} = d\hat{d}_{z;k} \quad (30)$$

$$F_z = d^2 \quad (31)$$

The divergence of the gradient of a scalar field $\lambda(\mathbf{r})$ is defined likewise. Hence, Eq. (17) reads in discretized form

$$\hat{D}_{ijk}\{\lambda\} = \hat{D}_{ijk}\{\mathbf{u}\} \quad (32)$$

for all grid cells \mathcal{V}_{ijk} belonging to the calculation area \mathcal{R} . As for every grid cell exactly one value of λ must be determined, the number of equations is equal to the number of unknowns.

The calculation of the right side of Eq. (32) is straightforward because the empirical field \mathbf{u} is defined for the whole calculation area and in particular at the boundary faces of all grid cells. It is assumed that \mathbf{u} fulfills the boundary conditions, i.e. vanishing normal components at the fixed impermeable boundary faces.

The left side of Eq. (32) cannot be solved by means of Eqs. (24) to (26) for cells \mathcal{V}_{ijk} in contact with a boundary of the calculation area, i.e. either the boundary of an obstacle or the outer boundary of the total calculation area. To make this point clear, let us imagine that this is the case for face $x = x_i$ (boundary face of $\mathcal{V}_{i,j,k}$ at the "right" side). Then $\lambda_{x;i,j,k}$ cannot be computed by means of Eq. (24) because $\hat{\lambda}_{i+1,j,k}$ is not defined.

If the boundary face is a fixed one, the boundary condition (flow throw this face) is already fulfilled by \mathbf{u} and the field λ should not change this flow, i.e. $\lambda_{x;i,j,k} = 0$ must be set. If the

boundary face is open, λ must be 0 at this face according to condition (15). In this case, $\lambda_{x;i,j,k} = -2\hat{\lambda}_{i,j,k}/d$ must be set. The boundary faces in x and y direction must be treated likewise.

Solving the system of equations

Eq. (32) is a system of equations for the unknowns $\hat{\lambda}_{ijk}$ in the form

$$\begin{aligned} R_{i,j,k}\{\lambda\} \equiv & A_{i,j,k}^{(111)}\hat{\lambda}_{i,j,k} + A_{i,j,k}^{(011)}\hat{\lambda}_{i-1,j,k} + A_{i,j,k}^{(211)}\hat{\lambda}_{i+1,j,k} \\ & + A_{i,j,k}^{(101)}\hat{\lambda}_{i,j-1,k} + A_{i,j,k}^{(121)}\hat{\lambda}_{i,j+1,k} + A_{i,j,k}^{(110)}\hat{\lambda}_{i,j,k-1} + A_{i,j,k}^{(112)}\hat{\lambda}_{i,j,k+1} - B_{i,j,k} \\ = & 0 \end{aligned} \quad (33)$$

The quantity $R_{i,j,k}\{\lambda\}$ is the residuum, i.e. the divergence of the field $\nabla\lambda - \mathbf{u}$, for the cells of the calculation grid. The system of equations is solved iteratively by successive overrelaxation.²² If an approximate solution λ^{old} is known, the new approximate solution λ^{new} is calculated according to

$$\hat{\lambda}_{i,j,k}^{\text{new}} = \hat{\lambda}_{i,j,k}^{\text{old}} - \omega \frac{R_{i,j,k}\{\lambda^{\text{old}}\}}{A_{i,j,k}^{(111)}} \quad (34)$$

The start value is typically 0. The relaxation parameter ω is a number between 1 and 2 and determines the convergence properties of the iterative procedure. An optimum choice is

$$\omega = \frac{2}{1 + \sqrt{1 - \rho_J^2}} \quad (35)$$

where ρ_J is the spectral radius of the Jacobi iteration. For two-dimensional problems it is approximately given by

$$\rho_J \approx \frac{\cos\left(\frac{\pi}{n_x}\right)/d_x^2 + \cos\left(\frac{\pi}{n_y}\right)/d_y^2}{1/d_x^2 + 1/d_y^2} \quad (36)$$

An extension to the three-dimensional case seems straightforward but it is problematic due to the fact that the vertical grid may not have a constant mesh width for the envisioned application. Practical applications show that an extension is suitable if the vertical mesh width is kept constant at least within the area occupied by the buildings. When calculating several wind fields for the same geometry (wind field libraries), it is more efficient first to determine in a series of test runs the value ρ_J that yields optimum convergence.

The algorithm in Eq. (34) has the special feature that calculating the new value of a given grid cell only requires the old value and the values from neighbouring cells with an index value increased or decreased by 1. Dividing the whole grid into cells with an index sum $i + j + k$ of even number (red grid) and odd number (black grid), the situation can be described as

²²W.H. PRESS, S.A. TEUKOLSKY, W.T. VETTERLING, B.P. FLANNERY: *Numerical Recipes in C*, Cambridge University Press, 1999.

follows: if the new value for a red cell is calculated, only its old value and values from the black grid are required, and vice versa.

It is therefore efficient to apply intermediate steps: first to calculate all new values for the red cells and from these all new values for the black cells. This procedure can be further optimized if ω is not kept constant but varied in every step. The reason is that the value of Eq. (35) leads to optimum convergence only asymptotically, i.e. for long iterations, whereas during the first iteration steps the residuum may increase substantially. The so-called Chebyshev acceleration circumvents this effect by setting ω as follows:

$$\begin{aligned}\omega^{(0)} &= 1 \\ \omega^{(1/2)} &= 1/(1 - \rho_J^2/2) \\ \omega^{(n+1/2)} &= 1/(1 - \rho_J^2 \omega^{(n)}/4) \quad \text{for } n = 1/2, 1, 3/2, \dots\end{aligned}\tag{37}$$

The iterations are continued until a given maximum number of iterations is exceeded or the mean or maximum of the residuum is below a given threshold value.

B Parameter variations

In order to demonstrate to which degree the concentration distributions obtained with the model approach depend on the specific value of a model parameter, the concentration distribution near ground for an isotropic wind rose and a source on top of an U-shaped building at 1.2 and 1.7 times the building height was calculated for the following parameter sets:²³

Varied parameter	Parameter meaning	Default value	Tested values
a_1, a_3	Extension and magnitude of the recirculation	$a_1 = 6, a_3 = 0.3$	$a_1 = 9, a_3 = 0.2$; $a_1 = 5, a_3 = 0.4$
a_2	Weighting of the recirculation with the incident flow direction	1	0.5; 1.5
a_5	Reduction of the z component	0.7	0.5; 1
h_s	Extension of the additional turbulence above the upper building edge	1.2	1.0; 1.5
f_s	Magnitude of the additional velocity fluctuations	0.5	0.25; 1.0 ($f_s f_k = \text{const.}$)
f_k	Magnitude of the additional diffusion coefficients	0.3	0.15; 0.6

The parameters not being varied were set to their default values.

Figs. 58 to 63 show the results in comparison with the default calculation ($z_0 = 0.2$ m, $d_0 = 1.2$ m, $h_a = 11.2$ m, $u_a = 3$ m/s, $\Delta z = 4$ m, $\Delta x = 6$ m, $H = 20$ m).²⁴ The following table lists the change of maximum concentration near ground with respect to the default calculation (in rounded units of 10 %):

Varied parameter	$H_Q/H = 1.2$	$H_Q/H = 1.7$
a_1, a_3	+10%; +20%	+10%; +0%
a_2	-10%; +20%	+0%; -0%
a_5	+0%; -0%	-0%; +0%
h_s	-0%; +10%	-10%; +0%
f_s	+10%; +30%	-0%; +0%
f_k	-10%; +20%	-20%; +20%

As expected, the influence of the parameters a_1, a_2, a_3, a_5 that determine the wind field in the

²³When changing the value of f_s, f_k was reset so that the additional diffusion being proportional to the product $f_s f_k$ remained unchanged.

²⁴The statistical uncertainty of the concentration values for the elevated source is rather high because of the small horizontal mesh width being used. At larger distances a star-like structure can appear due to the discretization of wind directions in sectors of 10 degree.

near wake zone of the building is stronger for the lower source than for the elevated one. In contrast, the parameter f_k that controls the long-reaching additional diffusion affects as well the concentrations from the elevated source.

The comparisons show that for a variation of single parameter values by up to a factor of 2, the change in the model results are considerable smaller, hence they do not depend in a very sensitive way on the default values that have been chosen.

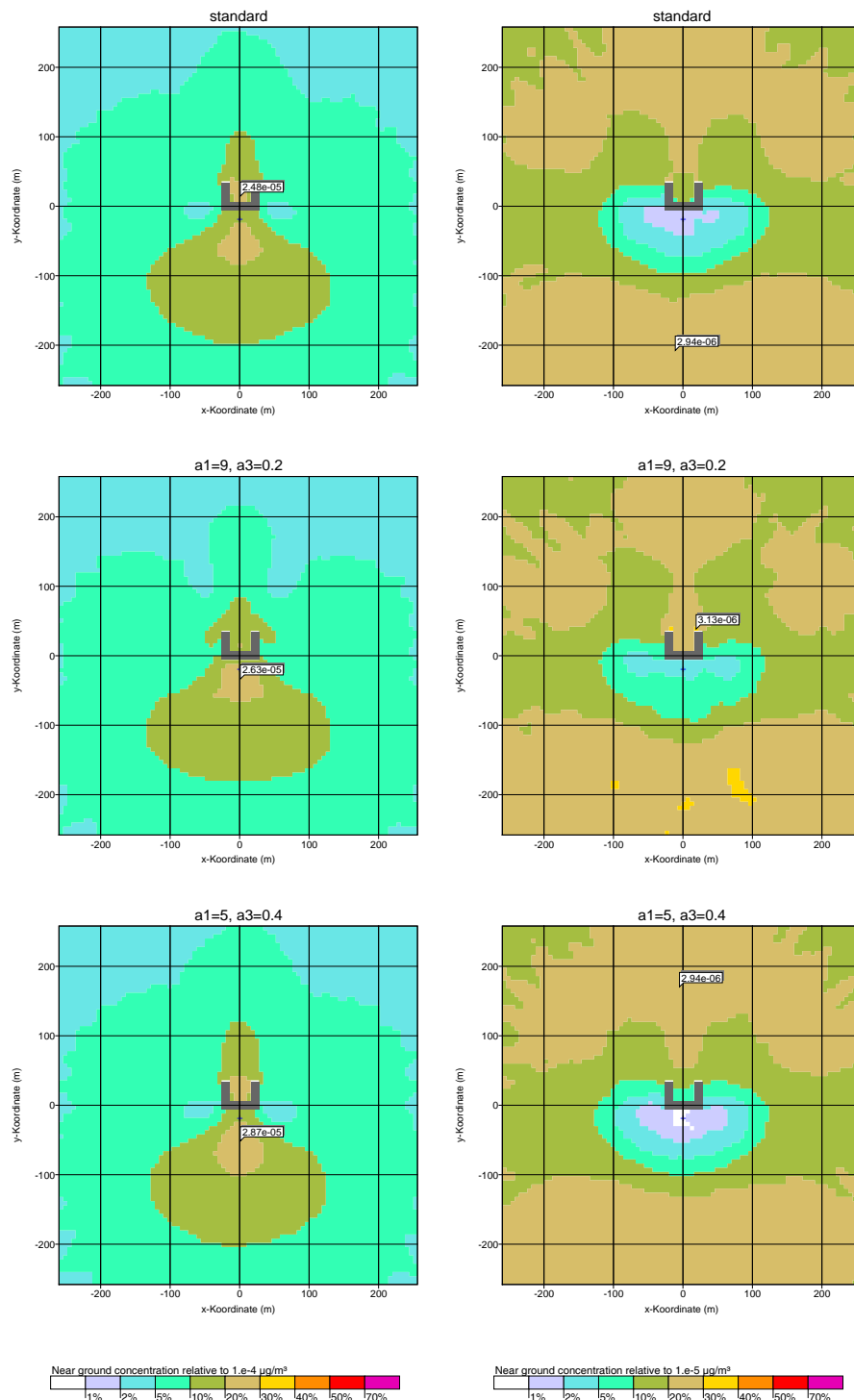


FIGURE 58: Parameter variations, parameters a_1 and a_3 . Concentration distribution near ground for an isotropic wind rose and a source height of 1.2 times (left column) and 1.7 times (right column) the building height. The graphs at the top of each column contain the results of a calculation using the default parameter values. Shown as well in every graph is the position and value of the maximum concentration.

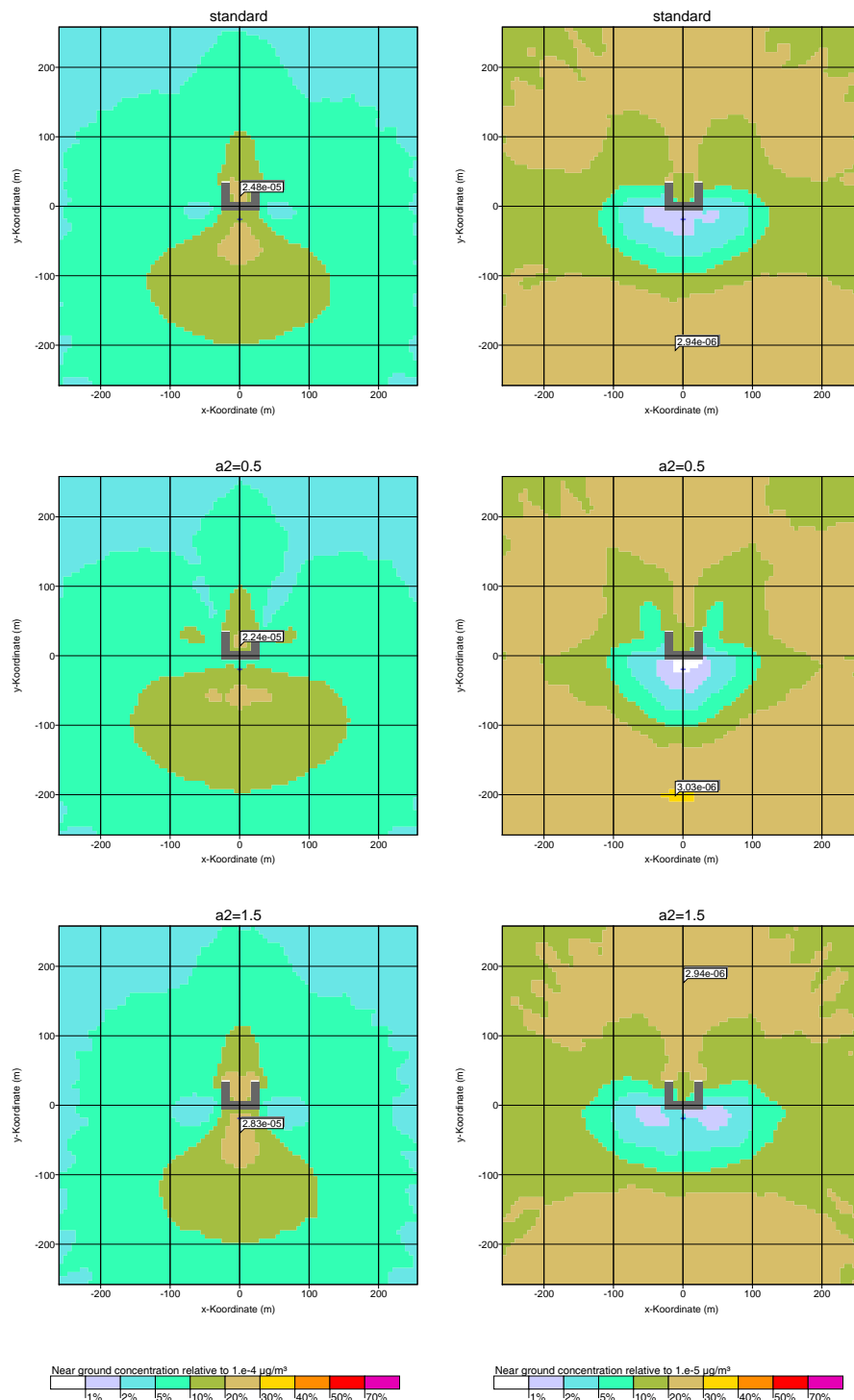


FIGURE 59: Parameter variations, parameter a_2 . Concentration distribution near ground for an isotropic wind rose and a source height of 1.2 times (left column) and 1.7 times (right column) the building height. The graphs at the top of each column contain the results of a calculation using the default parameter values. Shown as well in every graph is the position and value of the maximum concentration.

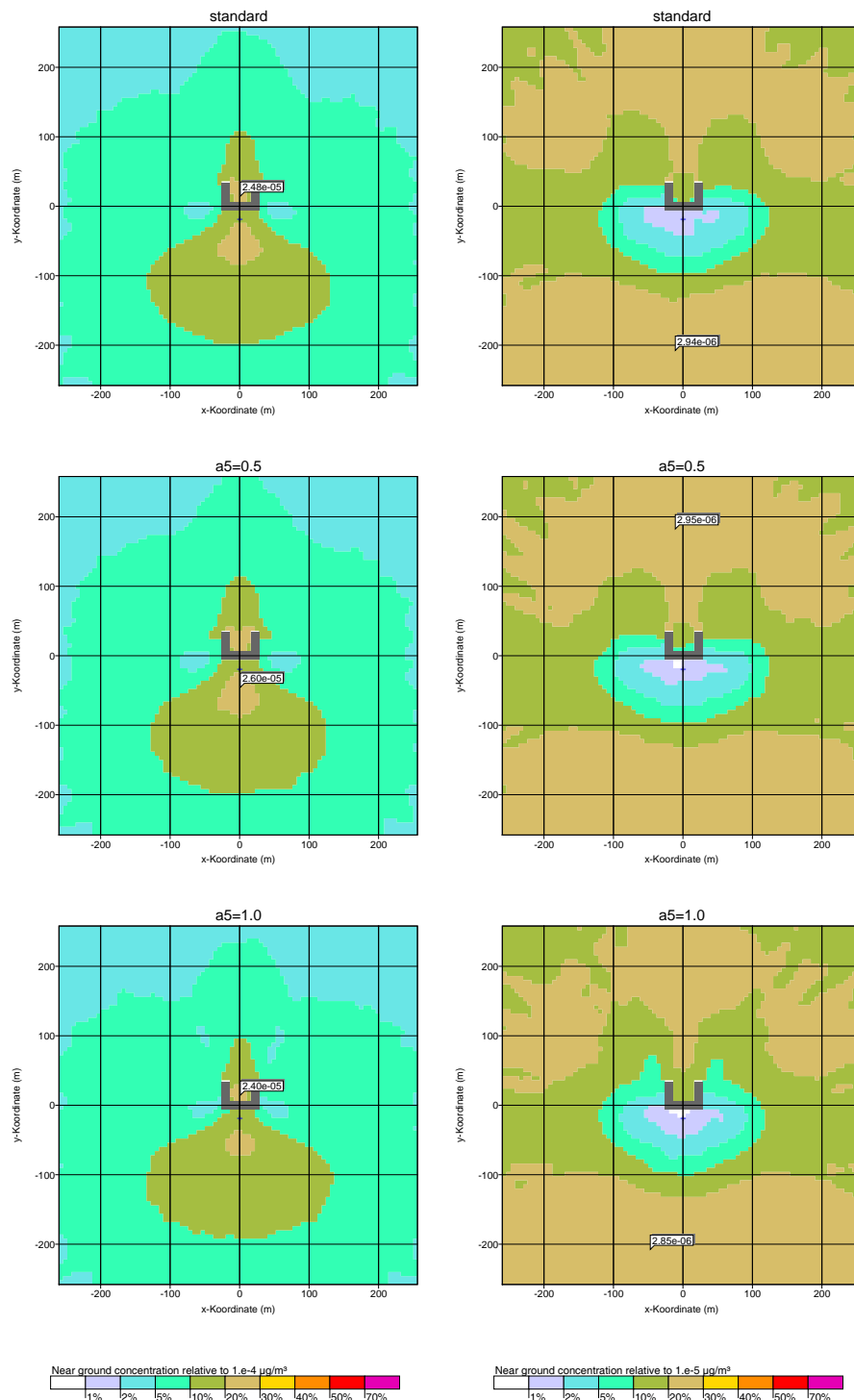


FIGURE 60: Parameter variations, parameter a_5 . Concentration distribution near ground for an isotropic wind rose and a source height of 1.2 times (left column) and 1.7 times (right column) the building height. The graphs at the top of each column contain the results of a calculation using the default parameter values. Shown as well in every graph is the position and value of the maximum concentration.

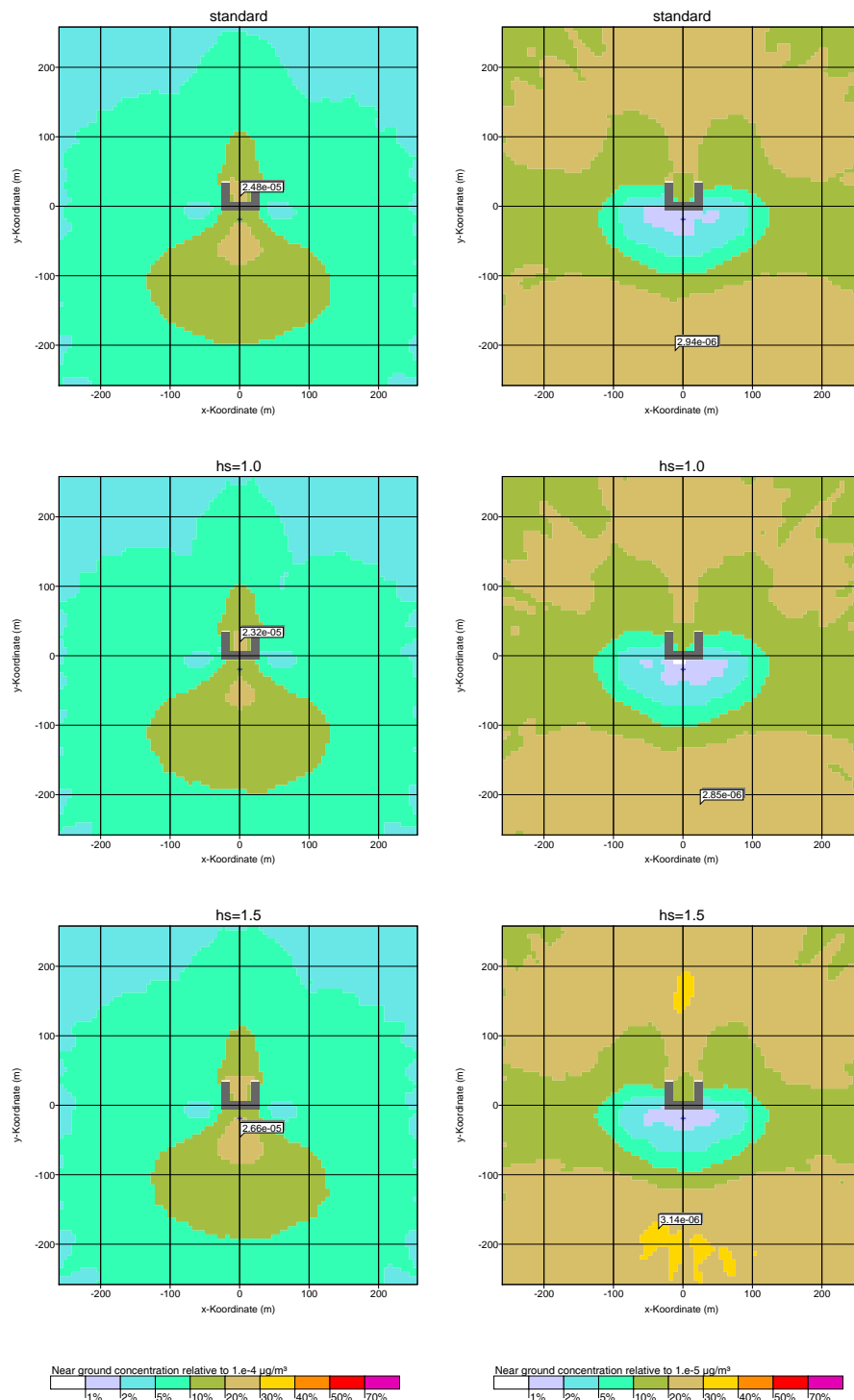


FIGURE 61: Parameter variations, parameter h_s . Concentration distribution near ground for an isotropic wind rose and a source height of 1.2 times (left column) and 1.7 times (right column) the building height. The graphs at the top of each column contain the results of a calculation using the default parameter values. Shown as well in every graph is the position and value of the maximum concentration.

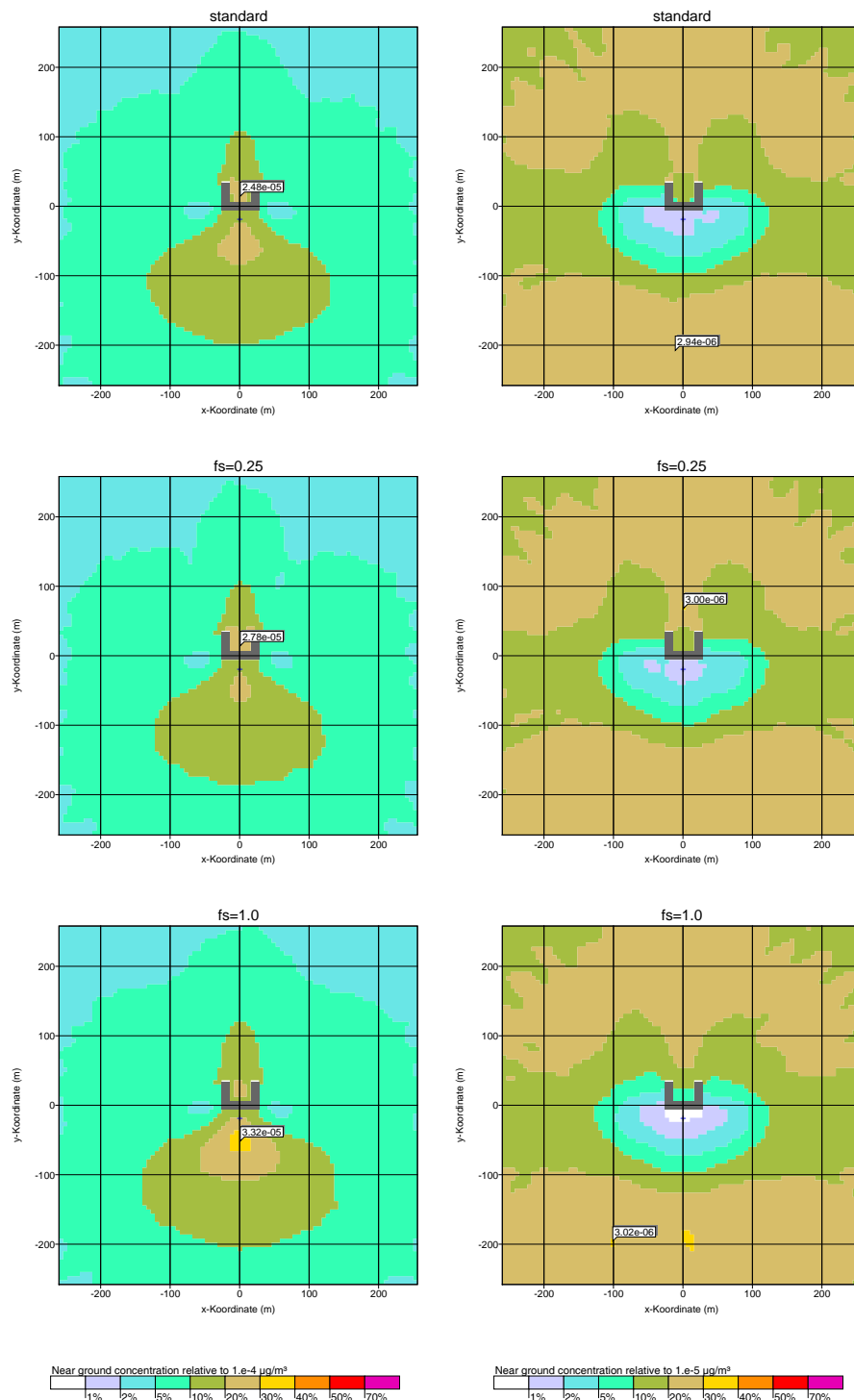


FIGURE 62: Parameter variations, parameter f_s . Concentration distribution near ground for an isotropic wind rose and a source height of 1.2 times (left column) and 1.7 times (right column) the building height. The graphs at the top of each column contain the results of a calculation using the default parameter values. Shown as well in every graph is the position and value of the maximum concentration.

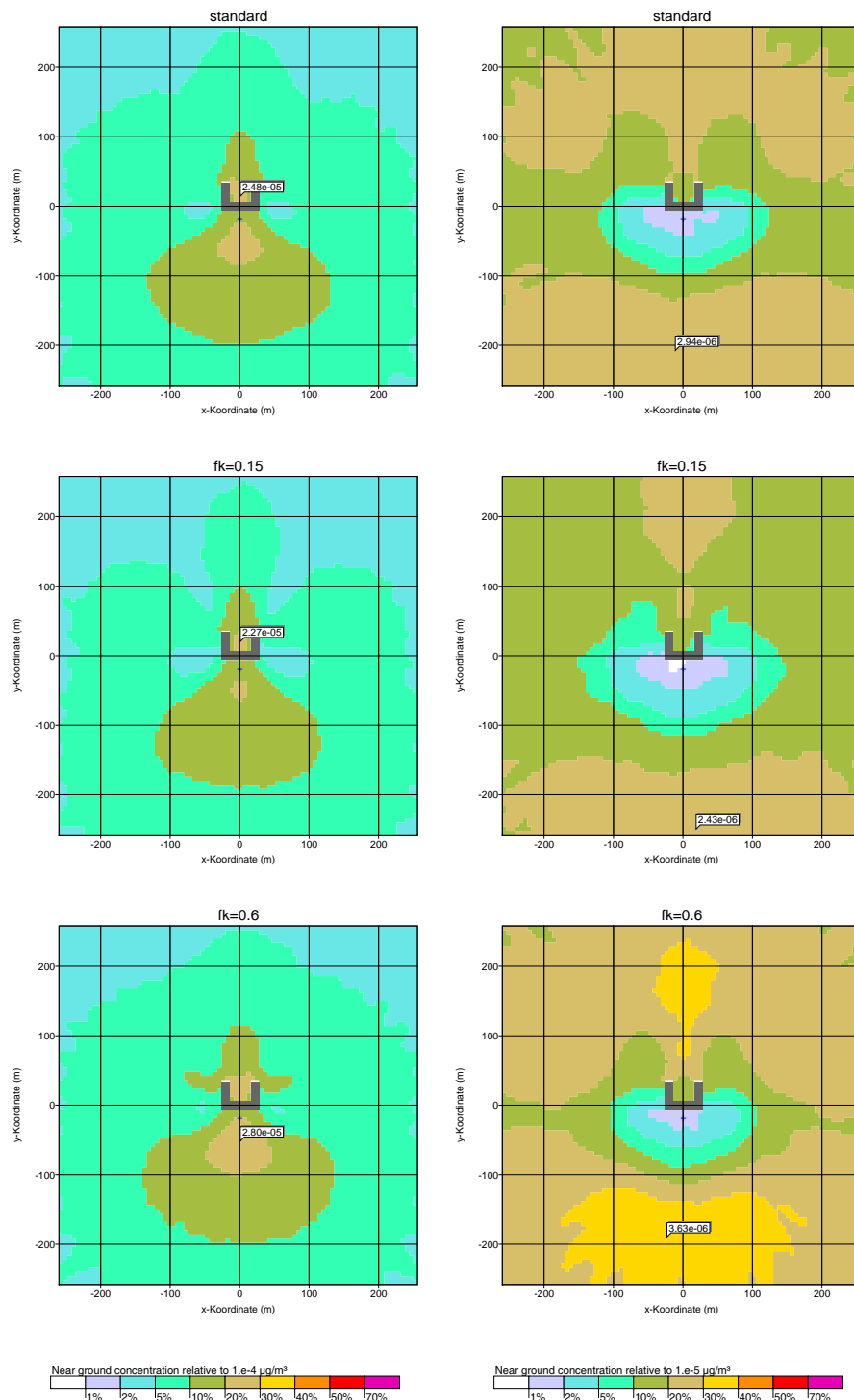


FIGURE 63: Parameter variations, parameter f_k . Concentration distribution near ground for an isotropic wind rose and a source height of 1.2 times (left column) and 1.7 times (right column) the building height. The graphs at the top of each column contain the results of a calculation using the default parameter values. Shown as well in every graph is the position and value of the maximum concentration.
